Lawrence Berkeley National Laboratory
Recent Work

Title
Superconducting and Normal-State Properties of Novel Materials

Permalink
https://escholarship.org/uc/item/8c81b01w

Author
Crespi, V.H.

Publication Date
1994-09-01
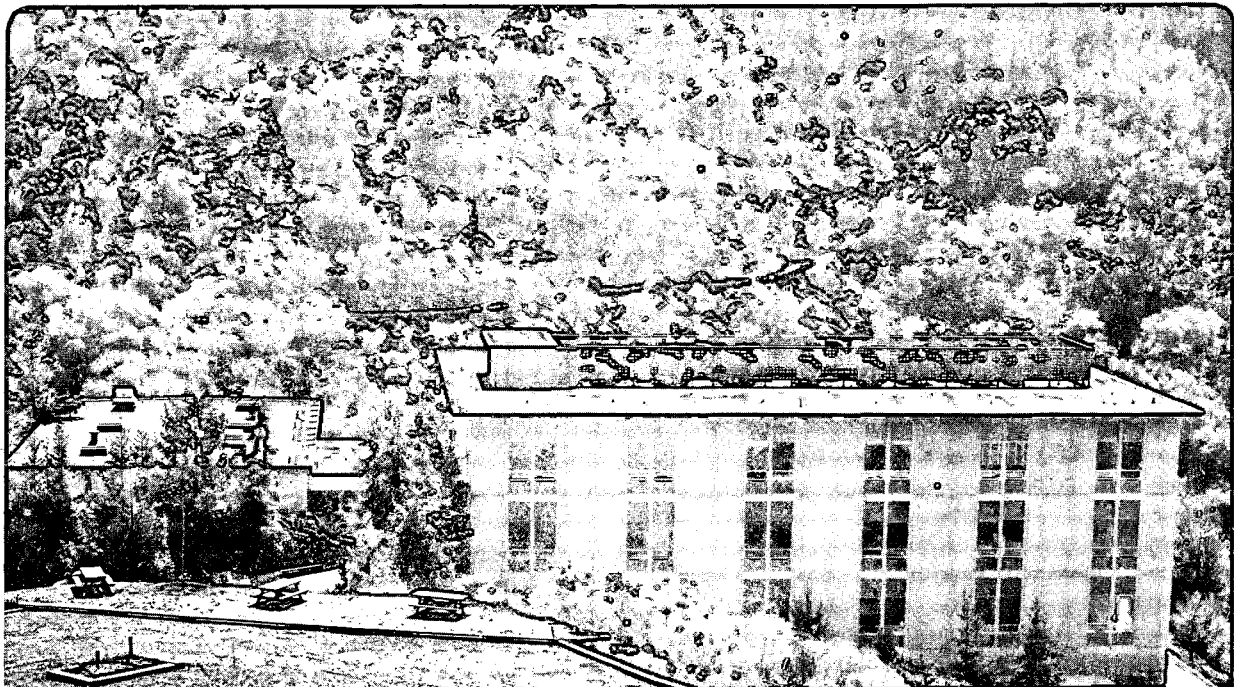
Lawrence Berkeley Laboratory
UNIVERSITY OF CALIFORNIA

Materials Sciences Division

Superconducting and Normal-State Properties of Novel Materials

V.H. Crespi
(Ph.D. Thesis)

September 1994

DISCLAIMER

Superconducting and Normal-State
Properties of Novel Materials

Vincent Henry Crespi

Department of Physics
University of California, Berkeley

and

Materials Sciences Division
Lawrence Berkeley Laboratory
University of California
Berkeley, California 94720

September 1994

Superconducting and Normal-State Properties of Novel Materials

Copyright © 1994

by

Vincent Henry Crespi

recycled paper

0.1 Acknowledgements

First and foremost, I would like to thank my advisor Marvin L. Cohen for his guidance, advice and friendship, qualities which flow from a caring nature, a deep knowledge of physics and years of accumulated wisdom.

The theoretical discussion of doped fullerenes stems from a close collaboration with Professor A. Zettl's experimental group. Any special merit to the theoretical results on the fullerenes derives primarily from the excellent experimental work of this talented group.

David Penn helped me get my start by collaborating with me and Marvin on my first paper. We later collaborated on the work of chapter 6. I would like to thank several researchers in the field for providing results prior to publication and generally being helpful people. Dr. Christian Elsässer provided the results of his frozen phonon calculation on $PdH(D)(T)$. Professor Pui K. Lam was also helpful in this area. Professor Steven C. Erwin provided me with theoretical results on alkali-doped C_{60}. Dr. Henry Krakauer sent me the detailed results of a calculation for phonon distortions in $La_{2-x}Sr_xCuO_4$. Dr. Igor Mazin and I had a useful discussion on resistivity calculations in alkali-doped C_{60}. Kosmas Prassides kindly provided data on the thermal expansion of K_3C_{60}. J. H. Nickel provided information pertaining to the site-selective isotope experiments. Troy W. Barbee III and I had several discussions relating to the original work on anharmonic phonons. Oleg Zakharov (an ever-helpful colleague and system manager) kindly spend a couple hours with me the night before I filed figuring out how to print this thesis at a beautiful 600 dots per inch. Finally, the Zettl group has provided a continuous source of interesting and illuminating discussions and collaborations with many people, including (but not limited to) Brian Burk, Bill Vareka, Kasra Khazeni, Nasreen Chopra, Li Lu, Xiao-Dong Xiang, Jing-Guo Hou, Gabriel Briceño, Kelly Cherrey, Jim Hone and Michael Fuhrer. I could always count on an entertaining and stimulating time if I strolled down

iii

to the Zettl lab.

The work of physicists would not be possible without the help of a capable support staff. Anne Takezawa, Mercy Wong, Abram Hardin, Barbara Gordon, Bertha Zambrano, Rita Jones and Sari Yamaguchi (among unnamed others) have always willing and able to smooth the bumps in the path of a graduate student.

Finally, I reserve a special thanks for my family, who have provided invaluable support through the years, the details of which are too numerous to mention.

0.2 Acknowledgements of Support

0.3 Dedication

The correct parts of this thesis are dedicated to all those who have helped me both in and apart from research. The incorrect parts are dedicated to the Herculean efforts of William Shanks, who over the period 1858–1873 calculated by hand the first 707 digits of π, a record for the time. Unfortunately, he made a mistake on the 528th digit, so that the rest of them were wrong. (The error was discovered by the programmers of Eniac, the first digital computer, which performed the calculation in 70 hours.) Any portion of this work which maintains value after the rest has fallen to the inevitable advancement of research is herein dedicated to the memory of Merrill Cohen.

Contents

CONTENTS

Abstract

SUPERCONDUCTING AND NORMAL-STATE PROPERTIES OF NOVEL MATERIALS

MATERIALS

Copper-oxide and Fullerene Superconductors

by

Vincent Henry Crespi

Doctor of Philosophy in Physics

University of California at Berkeley

Professor Marvin L. Cohen, Chair

Interest in solid state physics naturally gravitates towards novel systems which challenge our current level of understanding such as the copper oxide superconductors, or those which provide new venues for application and refinement of existing techniques such as the alkali-doped fullerenes. The present work tackles the challenge of high temperature superconductivity by extension of the BCS theory for ordinary superconductors, in particular, the incorporation of anharmonicity in the phonon dynamics and anisotropy in the electron-phonon coupling. These refinements can account for many of the anomalous properties of the cuprates. Phonon anharmonicity is consistent with a small isotope effect at optimal doping and a larger isotope effect in suboptimal systems. Anisotropy in the interaction, a plausible consequence of certain anharmonic models, can circumvent objections to electron-phonon coupling based on transport measurements. In addition, such anisotropy is consistent with gap anisotropy and the strong temperature dependence of the Hall coefficient. In contrast to the cuprates, the doped fullerenes appear to be understandable within the standard model of single electron band theory and the BCS theory.

The microscopic parameters derivable from transport and critical field measurements yield a self-consistent picture of a disordered type-II BCS superconductor. Isotope effect experiments imply that superconductivity is mediated by carbon phonons as opposed to alkali atom vibrations. The novel properties of the fullerenes are generally traceable to their microscopic heterogeneity, being a collection of tightly bound but weakly overlapping molecules. For example, the separation of electronic regimes into weak intermolecular overlap and strong carbon-carbon on-ball bonds yields a superconductor with both a large density of states and a high phonon frequency, properties consistent with a relatively high T_c. In addition, the disordered nature of the intermolecular overlap produces a large residual resistivity and an interesting universal dependence to the Hall coefficient. This disorder is also consistent with the anomalously large carbon isotope effect for heterogeneous isotopic substitution.

Chapter 1

Anharmonic Phonons in Superconductivity: Overview

1.1 Background

In a normal metal at T=0 the occupied electronic states below the Fermi energy are neighbored by unoccupied states just above. In a macroscopic system the level spacing is so small that an arbitrarily small perturbation can find phase space to scatter an electron from an occupied state to an unoccupied one, yielding finite scattering amplitude and a finite resistivity. The near-continuous nature of the set of electronic states allows an external electric field to displace the Fermi surface and produce a current. Imagine a metallic system with a displaceable Fermi surface which instead has a energy gap between occupied and unoccupied states. At first sight this may appear ridiculous- we are already familiar with systems with a gap, they are semiconductors or insulators, not metals. Their gap arises from the crystal potential splitting the electronic bands at the Brillioun zone edge so that a filled lower band resides at a finite energy below the unoccupied bands. Since the excited electronic states of an insulator are far removed from the occupied electronic states, the energy denominators in the perturbation expansion for an external field suppress the effects of the applied field. A applied electric field which is small on the atomic scale (as all experimentally accessible macroscopic fields are) cannot displace the "Fermi surface" and insulating behavior results. How can a gap between occupied and unoccupied states form in a system with metallic behavior? The source of the gap must reside elsewhere than the crystal potential.

The Hamiltonian matrix of the noninteracting Fermi gas is diagonal, a sum of single particle energies. The interactions between electrons and phonons gives rise to an effective

interaction between electrons which is mediated by phonons. This effective interaction is attractive for electrons close enough in energy; in this regime it can dominate the Coulomb repulsion to yield a net attractive interaction. In general, Fermi-Dirac statistics guarantee that the contributions to the total many-body Hamiltonian matrix from this attractive interaction will be composed of various matrix elements of different signs which on the whole compose a fairly uninteresting contribution to the energy. However, a particular ordered state of the electrons can yield a Hamiltonian matrix in which the complex assortment of electron-phonon matrix elements contribute with the same sign, an ordered state which has a substantially lower energy than the normal ground state. At sufficiently low temperatures this alternative ordered state is thermodynamically favored, and the system enters this novel ground state. The crucial property of this state is that its energy advantage over the normal ground state is due to a macroscopic ordering of the wavefunction. The perturbation of any one electron has repercussions for the entire ordered state; the perturbation of any single electron therefore requires a finite energy. The system has acquired an energy gap while maintaining the fundaments of the metallic state. The system is a superconductor.

What in particular is this ordered state? At first sight, there would seem to be many schemata about which the electronic state could order. Nature chooses a simple form; the electronic states are occupied in correlated pairs, yielding a state in which the off-diagonal matrix elements connecting different many-body states enter the Hamiltonian with the same sign. Turning to the detailed physics, Bardeen, Cooper and Schrieffer[1] proposed that one could examine a reduced Hamiltonian for the electronic system with electron-phonon interactions, a Hamiltonian which only embodied interactions between the mates of the correlated pairs of electrons,

$$H_{reduced} = \sum_{ks} \epsilon_k n_{ks} + \sum_{kk'} V_{kk'} b_{k'}^{\dagger} b_k, \qquad (1.1)$$

where ϵ_k is the single particle energy, n_{ks} is the occupation number for electrons of wavevec-

tor k and spin s, $V_{kk'}$ is the (attractive) interaction between members of a pair, and $b_k^\dagger = c_{k\uparrow}^\dagger c_{k'\downarrow}^\dagger$ creates a pair of electrons in the single particle states $k\uparrow$ and $-k\downarrow$. Taking this reduced Hamiltonian, they proposed an ansatz for a variational ordered wavefunction,

$$|\Psi\rangle = \prod_k \frac{1 + g_k b_k^\dagger}{\sqrt{1 + |g_k|^2}} |0\rangle \qquad (1.2)$$

with the $\{g_k\}$ a set of variational parameters. Minimizing the ground state energy while constraining the number of particles to be a constant yields the set $\{g_k\}$ expressed in terms of the single particle energies ϵ_k and a new entity, Δ_k. Skipping the detailed form for $\{g_k\}$, we instead turn to the T=0 integral equation for Δ_k,

$$\Delta_k = -\sum_{k'} V_{kk'} \frac{\Delta_{k'}}{2E_{k'}} \qquad (1.3)$$

where $E_k = \sqrt{\epsilon_k^2 + \Delta_k^2}$ will turn out to the the quasiparticle excitation energy. Note that the quasiparticle excitation energy does not go to zero at the Fermi energy, but instead limits to the value Δ_k, the *energy gap*. Taking a very simple form for the electron-phonon interaction

$$V_{kk'} = \begin{cases} -V & |\epsilon_k|, |\epsilon_{k'}| < \omega_c \\ 0 & \text{otherwise} \end{cases} \qquad (1.4)$$

for some characteristic phonon frequency ω_c yields a constant Δ_k for $|\epsilon_k| < \omega_c$ and $\Delta_k = 0$ outside this range. Within ω_c of the Fermi energy the energy spectrum of the electron quasiparticles is qualitatively different from the free Fermi gas.

Finite temperature is easily handled by the introduction of Fermi factors which lead to the generalized gap equation

$$\Delta_k = -\sum_k V_{kk'} \frac{\Delta_{k'}}{2E_{k'}} \tanh \frac{E_{k'}}{2k_B T}. \qquad (1.5)$$

At sufficiently low temperature this equation has a solution for finite Δ_k, a ground state with a finite energy gap. Once again using approximation 1.4 for the pairing interaction $V_{kk'}$, converting the sum to an integral over energy and solving for the temperature T_c at

which $\Delta \rightarrow 0$ yields

$$k_b T_c = 1.14 \omega_c e^{-\frac{1}{N(0)V}} \tag{1.6}$$

where N(0) is the density of states at the Fermi level. The characteristic frequency ω_c is set by the energy scale of the phonon distortions which mediate the coupling between electrons. The product N(0)V is generally written as λ=N(0)V. Below T_c the material is a superconductor with a finite energy gap. Above T_c the system is a normal metal.

This BCS model T_c formula is accurate only for extremely small values of the coupling constant. For realistic systems one must take into account the finite Coulomb repulsion and the renormalization of the electron-phonon interaction by its own influence upon the individual electronic states that it couples. In its simplest form, such a treatment yields a transition temperature,

$$T_c = 1.14 \omega_c e^{-\frac{1}{\frac{\lambda}{1+\lambda} - \mu^*}} \tag{1.7}$$

where $\mu^* = \frac{\mu}{1+\mu \ln \frac{E_f}{\omega_c}}$ is the Coulomb repulsion renormalized to take into account the large difference in energy scales between electronic and vibrational dynamics.

McMillan carried this procedure a step further by taking a physically motivated form of the T_c equation which incorporated finite Coulomb repulsion and interaction renormalization with a small set of adjustable parameters that were fit to solutions for the full electron-phonon coupling spectrum of Nb[2]. The resulting formula, which is valid over the fitted range of $\lambda \sim 0.0 \rightarrow \sim 1.5$, is

$$T_c = \frac{\omega_{log}}{1.2} \exp \frac{-1.04(1+\lambda)}{\lambda - \mu^*(1+0.62\lambda)} \tag{1.8}$$

where the original McMillan prefactor has been replaced by the more general logarithmic prefactor of Allen and Dynes[3],

$$\omega_{log} = \exp \frac{2}{\lambda} \int_o^\infty d\omega \alpha^2 F(\omega) \frac{\ln \omega}{\omega}. \tag{1.9}$$

In all of the T_c expressions the prefactor is a measure of the characteristic phonon frequency relevant to the electron-phonon coupling and the more complicated exponential

embodies the relative strengths and renormalizations of the electron-phonon and Coulomb interactions.

A more careful treatment in the case of strong coupling yields the Eliashberg equations[4, 5], which may be solved numerically to obtain superconducting properties at arbitrary coupling constant λ. The realm of validity of the Eliashberg equations when applied to standard superconductors is set not so much by inherent inaccuracies in the treatment of the superconducting state but by the the prominence of alternative instabilities at large coupling, in particular static lattice instabilities. The Eliashberg equations provide an accurate theoretical framework applied with great success to many cases of lower-temperature superconductivity.

The standard harmonic approximation of phonon dynamics yields phonon frequencies proportional to the inverse square root of the oscillator mass, $\omega \propto M^{\frac{1}{2}}$. In contrast, the electron-phonon coupling λ is mass-independent. Ignoring Coulomb repulsion for the moment, we obtain that the superconducting transition temperature, which is proportional to the relevant (i.e. phononic) energy scale, is proportional to the inverse oscillator mass, yielding an isotope effect exponent $\alpha \equiv -\frac{M}{T_c}\frac{dT_c}{dM} = \frac{1}{2}$. In fact, the measurement of $\alpha \approx \frac{1}{2}$ in Pb provided critical guidance in the development of the BCS theory of superconductivity.

The electron-phonon coupling can be written quite simply as $\lambda = \frac{N(0)\langle I^2\rangle}{M\langle\omega^2\rangle}$ where $\langle I^2\rangle$ is an averaged matrix element over electronic states and $\langle\omega^2\rangle$ is an average phonon frequency[2]. The numerator can be interpreted as an electronic spring constant and the denominator is easily seen to be a phonon spring constant. How could this expression be of guidance for increasing the transition temperature? The superconducting T_c is proportional to the average phonon frequency and is also a monotonically increasing function of λ. To increase T_c, we could increase the numerator in λ, increasing the sensitivity of the electronic states to the phonon displacements. We could also decrease the phonon spring constant, decreasing the denominator in the expression for λ. A decreased phonon spring constant will also decrease the average phonon frequency, but on the whole such

a modification yields a net increase in T_c. Finally, we could decrease the oscillator mass and thereby increasing the average phonon frequency while λ remains constant.

Each of these proposed modifications has ramifications for the harmonic approximation of phonon dynamics. A large electronic spring constant means that a given phonon displacement causes large changes in the electronic structure. These changes in turn influence the energy versus displacement relation of the phonon distortion, possibly producing a novel form for the vibrational potential. A decrease in oscillator mass or a decrease in phonon spring constant both imply an increase in oscillation amplitude with a concomitant increased influence of anharmonic terms. Each of the strategies for increasing the superconducting transition temperature carries with it the possibility of increased phonon anharmonicity, suggesting that phonon anharmonicity should be taken into account in superconductors with unusually high transition temperatures.

Anharmonicity affects superconductivity in three ways: a shift in the phonon frequencies, the introduction of Debye-Waller factors in the ionic potential, and multi-phonon processes. These processes are all second order in the ratio of ionic displacement to lattice constant[6]. We concentrate on the modification of phonon frequencies and multiphonon processes. For several interesting forms of anharmonicity the modification of phonon frequencies is quite dramatic; for an equally wide class of anharmonic potentials the atomic displacement are large enough to necessitate consideration of second order multiphonon processes. In contrast, the modification of Debye-Waller factors seems less likely as a source of qualitatively new behavior.

We assume the validity of the standard harmonic treatment for the transition temperature T_c, whether the full Eliashberg equations or a simplified T_c equation in term of λ, the Coulomb repulsion μ^*, and an average phonon frequency. We emphasize that there is no rigorous justification for extending the scope of the harmonic T_c equations. A self-consistent treatment of phonon anharmonicity yields expressions which are formally identical to the Eliashberg equations with a fully anharmonic expression replacing the

spectral density of the one-phonon Green function[6]. Unfortunately, the equations are computationally intractable. In effect, we use a simple form for this spectral density within an Einstein model in which phonon-phonon interactions can be neglected. At least for harmonic superconductivity calculations the assumption of an Einstein spectrum will not introduce qualitative errors since an Einstein model produces values of T_c reasonably close to those given by more realistic phonon spectra[7]. Dispersion of an anharmonic mode could conceivably change the results qualitatively, if the anharmonic terms produce novel low-lying eigenstates. Preliminary classical models of various forms of anharmonic lattices yield relatively straightforward dynamics without suggestions of underlying novel quantum behavior. Unfortunately, the quantum mechanical calculation of an analog to a dispersion relation for a strongly anharmonic phonon is problematic. In addition, the strong coupling between anharmonic phonons of different $\vec{q}$ presents a difficult exercise in frequency renormalization. The treatment of Einstein modes, although decidedly less rigorous than a full dispersive calculation, has the virtue of computational simplicity. With these caveats in mind, we explore the effects of anharmonicity.

The electron-phonon coupling at zero temperature can be generalized to the anharmonic case by including matrix elements over all of the phonon excited states[8]. Since certain anharmonic modes involve large ionic excursions, the quadratic term in the expansion of the electron-ion potential is included. The zero temperature form for the electron-phonon coupling should be valid for transition temperatures sufficiently below the relevant phonon frequency, as will be the case for $\lambda < 2$. We begin with an expression for the electron-phonon coupling constant λ involving a sum over all phonon excited states labelled by the index n and electronic states $|k'\rangle$ and $|k\rangle$,

$$\lambda = N(0) \sum_{kk'}^{(FS)} \sum_{n=1}^{\infty} \frac{|\langle n|\langle k'| \left((\nabla V \cdot \delta \mathbf{R})_{R_0} + \nabla_i \nabla_j V \delta \mathbf{R}_i \delta \mathbf{R}_j \right) |k\rangle|0\rangle|^2}{E_n - E_0}, \qquad (1.10)$$

where N(0) is the density of states at the Fermi level, V(r) is the electron-ion potential, and $\delta \mathbf{R}$ is the ionic displacement from the equilibrium position $\mathbf{R}_0$. The sum over k and

(a)   (b)
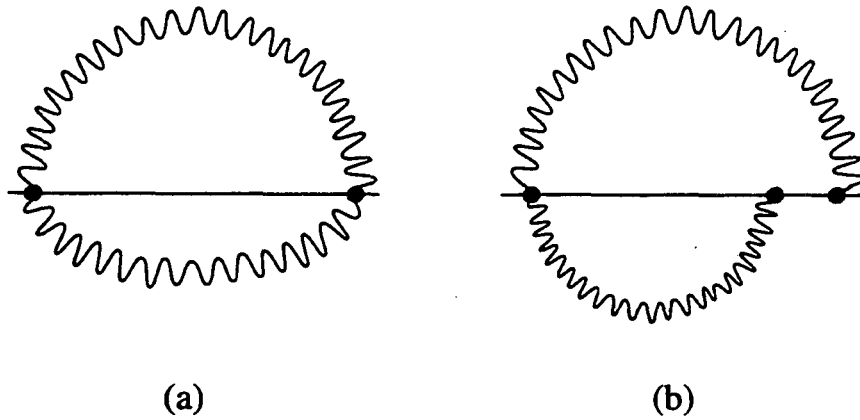
Figure 1.1: Second order contributions to the electron-phonon coupling

k' is performed over the Fermi surface. The cross terms with $i \neq j$ in the second order term are usually small for potentials suitably oriented with respect to the coordinate axes. Assuming, for example, a phonon eigenmode polarized in the x direction, we obtain

$$\lambda = \sum_{n=1}^{\infty} \left[\langle I^2 \rangle \frac{|\langle n|x|0 \rangle|^2}{E_n - E_0} + \langle J^2 \rangle \frac{|\langle n|x^2|0 \rangle|^2}{E_n - E_0} \right]. \qquad (1.11)$$

The electronic degrees of freedom have been factorized out and lumped into prefactors $\langle I^2 \rangle$ and $\langle J^2 \rangle$, analogous but not identical to the prefactor in the case of pure linear coupling[2]. The remaining expression involves a summation over only matrix elements between phonon states.

We have included only one diagram of second order in the expression for lambda (or equivalently, the expression for the electronic self-energy). In particular, we have included contributions of the form shown in Fig. 1.1(a), but ignored diagrams of the form shown in Fig. 1.1(b). Diagram (a) has one intermediate electronic state, whereas diagram (b) has two. The dominant contributions to the coupling arise from regions of integration where the intermediate electronic states are near the Fermi surface. In diagram (a), this condition puts one constraint on $\vec{Q}_1 + \vec{Q}_2$ (namely, $\vec{Q}_1 + \vec{Q}_2$ must bridge the Fermi surface). In diagram (b), this condition puts constraints on $\vec{Q}_1$ and $\vec{Q}_2$ individually. Diagram (a) produces contributions to the coupling over a significantly larger portion of the phonon

phase space. For this reason, contributions of the form shown in Fig. 1.1a are assumed to dominate the second-order electron-phonon coupling.

At this point there are two routes to obtaining expressions for the superconducting transition temperature within an anharmonic model. The various contributions in the summation for λ can either be lumped into a total λ at an average phonon frequency, values which are then used in a standard T_c equation, or the individual contributions can be incorporated into the electron-phonon coupling function $\alpha^2 F(\omega)$, which is used as input to the Eliashberg equations. The first approach has the virtue of computational simplicity, affording simple analytic formulae in certain cases, whereas the second approach avoids collapsing the phonon frequency spectrum to a single moment and in addition maintains validity over a wider range of coupling strengths. Both techniques will be used as appropriate.

Keeping in mind the first approach, an expression similar to that for λ can be written for the average squared phonon frequency,

$$\langle \omega^2 \rangle = \frac{N(0)}{\lambda} \langle I^2 \rangle \sum_{n=1}^{\infty} |\langle n|\delta R|0\rangle|^2 (E_n - E_0). \tag{1.12}$$

Where for the present we have considered only the linear term. Inclusion of higher-order terms introduces the complication of calculating the relative weights of the electronic prefactors of the higher-order terms. In addition, inclusion of these terms precludes the use of powerful sum rule relations. By concentrating on the linear term we obtain simple and useful analytic results that provide guidance in more complex situations.

The summation in 1.12 has the form of a sum rule with value $\hbar^2/2M$, where M is the ionic mass. Using this information,

$$\langle \omega^2 \rangle = \left[\frac{N(0)\hbar^2 \langle I^2 \rangle}{2} \right] \frac{1}{M\lambda} \tag{1.13}$$

The anharmonic λ and $\langle \omega^2 \rangle$ are related in the same manner as in the harmonic case. We

define separate isotopic exponents for λ and $\sqrt{\langle \omega^2 \rangle}$ in the form

$$\lambda_M = \frac{M}{\lambda} \frac{d\lambda}{dM}, \tag{1.14}$$

$$\omega_M = \frac{M}{\sqrt{\langle \omega^2 \rangle}} \frac{d\sqrt{\langle \omega^2 \rangle}}{dM}, \tag{1.15}$$

where Eqn. 1.13 implies

$$\omega_M = -\frac{\lambda_M + 1}{2}. \tag{1.16}$$

Assuming that $\langle I^2 \rangle$ is independent of the ionic mass, the mass dependences of λ and $\langle \omega^2 \rangle$ can be calculated from the mass dependence of the dipole matrix elements and the oscillator levels. Note that the electronic prefactor could obtain a mass dependence if the electronic structure is sensitive to fine details of structural distortions. For a pure harmonic potential, $\omega_M = -\frac{1}{2}$, so that Eqn. 1.13 yields $\lambda_M = 0$, as expected. Since the electronic prefactor in the expression for λ is generally unknown or difficult to calculate, we do not calculate the absolute value of $\frac{d\lambda}{dM}$. Instead, we calculate $\frac{M}{\lambda}\frac{d\lambda}{dM}$, a measure of the relative sensitivity of λ to variations in the oscillator mass.

Having elucidated the mass dependence of λ and $\langle \omega^2 \rangle$, we can determine α from the Kresin-Barbee-Cohen T_c equation[9, 10],

$$T_c = 0.26 \frac{\sqrt{\langle \omega^2 \rangle}}{\sqrt{e^{\frac{2}{\lambda}} - 1}}, \tag{1.17}$$

where we have assumed that the Coulomb repulsion parameter $\mu^* = 0$. The Kresin-Barbee-Cohen equation provides a convenient analytic expression for the transition temperature which is valid at both weak and strong coupling. For moderately large λ, the $\mu^* = 0$ approximation is a reasonable first approximation of the Eliashberg results. A simple calculation yields

$$\alpha = \frac{1}{2} - \lambda_M \left[\frac{e^{\frac{2}{\lambda}}}{(e^{\frac{2}{\lambda}} - 1)\lambda} - \frac{1}{2} \right]. \tag{1.18}$$

The term multiplying λ_M is positive for all values of λ, so that the direction of deviation of α from $\frac{1}{2}$ will be determined by the sign of λ_M. In the strong coupling limit, we obtain

$$\alpha = \frac{1}{2} - \frac{\lambda_M}{2\lambda}. \tag{1.19}$$

The extreme strong-coupling limit of α is one half, regardless of anharmonicity. To study the influence of finite μ^* upon this limiting form we have solved the Eliashberg equations for μ^* from 0.05 to 0.25, obtaining a strong coupling limit of α that varies from 0.5 to 0.4.

In the weak coupling case the two square well approximation with a finite Coulomb repulsion yields an analytic form for finite μ^*,

$$\alpha = \frac{1}{2}\left(1 - \left(\frac{\mu^*}{\lambda^* - \mu^*}\right)^2\right)(1 + \lambda_M) - \frac{\lambda_M}{\lambda}\left(\frac{\lambda^*}{\lambda^* - \mu^*}\right)^2. \tag{1.20}$$

For positive λ_M, the introduction of μ^* will decrease α, as in the harmonic case. However, for negative λ_M the effect of μ^* depends on the value of λ_M. For sufficiently large negative λ_M, a positive μ^* can actually increase α. Calculations using the Eliashberg equations extend this result to the strong coupling regime. These Eqns. 1.18 and 1.20 can be used with the corresponding T_c equations to obtain a relation between T_c and α for a given anharmonic potential.

In contrast to the analytic approach presented above, the various energy level differences (E_n-E_0) and their contributions to λ can also be used to create an expression for the electron-phonon coupling function $\alpha^2 F$,

$$\alpha^2 F(\omega) = \sum_{n=1}^{\infty} \frac{1}{2}\lambda_n \omega_n \delta(\omega - \omega_n). \tag{1.21}$$

Once again taking the example of a phonon mode polarized in the x direction,

$$\lambda_n = \left[\langle I^2 \rangle \frac{|\langle n|x|0\rangle|^2}{E_n - E_0} + \langle J^2 \rangle \frac{|\langle n|x^2|0\rangle|^2}{E_n - E_0}\right] \tag{1.22}$$

with

$$\omega_n = E_n - E_0. \tag{1.23}$$

The three-dimensional isotropic Eliashberg equations for T_c are then solved within a matrix formalism[5].

The problem remains of calculating the various energy levels of the anharmonic potential. For a one-dimensional interionic potential, the numerical solution of the Schrödinger

equation is straightforward. The two-dimensional and three-dimensional Schrödinger equations are solved by expansion with a basis of eigenfunctions of the harmonic oscillator. For each energy level, we calculate the mass dependences of ω_n and λ_n and incorporate this information either into a T_c equation or the Eliashberg equations to obtain the relation between T_c and α.

1.2 Analytic Results

The Kresin-Barbee-Cohen equation under linear electron-phonon coupling provides simple analytic results for particular zoo of phonon potentials. For a pure quartic potential a simple scaling argument applied to the Schrodinger equation yields information about $\sqrt{\langle\omega^2\rangle}$. To wit, a shift in the mass can be counteracted by changes in length scale and energy scale. The energy rescaling implies that

$$\sqrt{\langle\omega^2\rangle} \propto M^{-\frac{2}{3}}, \tag{1.24}$$

so that

$$\lambda_M = \frac{1}{3}. \tag{1.25}$$

Since $\lambda_M > 0$, α is depressed below 0.5. Such an argument can be applied to any potential with only one length scale (e.g. pure sixth-order, etc); with potentials of the form $V(x)=x^{2n}$ yielding $\omega_M = -\frac{n}{n+1}$ and $\lambda_M = \frac{n-1}{n+1}$.

In the extreme anharmonic limit of a square well potential, elementary quantum mechanics yields

$$\sqrt{\langle\omega^2\rangle} \propto M^{-1}, \tag{1.26}$$

so that

$$\lambda_M = 1. \tag{1.27}$$

The stronger anharmonicity produces a greater deviation from the harmonic case.

We next obtain analytic results for a double well potential, a potential approximated as a pair of negative delta function potentials at $\pm a$. For simplicity, we initially include only linear electron-phonon coupling. A potential of the form

$$V(x) = -\frac{V_0 \hbar^2}{2Ma} [\delta(x+a) + \delta(x-a)] \qquad (1.28)$$

yields equations for the ground state and first excited state in which the energy level and oscillator mass always appear as a product, implying that $\omega_M = -1$. The sum rule relation then yields $\lambda_M = 1$, identical to the case of a square well. The double delta function potential has a single length scale, the separation between the wells, which is independent of the ionic mass, so that both the dipole and quadrupole matrix elements in Eqn. 1.22 are mass independent. For this reason, the inclusion of quadratic coupling will not change the mass dependence of λ or ω. A similar relation applies to the square well potential. For both potentials α is depressed below 0.5 for weak to moderate coupling and $\alpha = 0.5$ in the extreme strong coupling limit.

Potentials of the form $V(x)=x^{2n}$ can also be examined analytically for quadratic coupling, using the same scaling arguments. For linear coupling, a sum rule relation provided the mass dependence of λ. For quadratic coupling, we approximate the matrix element of x^2 with the square of the classical turning point. Numerical solutions of Schrödinger's equation support this approximation. This technique yields $\lambda_M = \frac{n-2}{n+1}$ and $\omega_M = \frac{n}{n+1}$. The strong coupling limit for α can be obtained from the asymptotic strong coupling T_c equation[3]

$$T_c = 0.18\sqrt{\lambda \langle \omega^2 \rangle}. \qquad (1.29)$$

For second-order electron-phonon coupling, the harmonic and pure quartic potentials limit to $\alpha = \frac{3}{4}$ and $\alpha = \frac{2}{3}$ respectively, values significantly different from the generic first-order coupling limit of $\frac{1}{2}$. For smaller values of the coupling, the deviation of the isotope effect exponent from 0.5 is generally in the same direction as that obtained in the strong coupling limit, with a larger deviation for weaker coupling.

We now briefly consider the limit of arbitrarily deep double wells (beyond the double delta function approximation introduced earlier). In this situation, one would expect the system to decouple into two uncoupled potential wells, with the particle occupying one well or the other. The ground state and first excited state will become degenerate ($E_0 \approx E_1$, as will all subsequent pairs of excited states. At first sight, Eqn. 1.10 seems to imply that λ will diverge, since the energy denominator goes to zero. However, for such low first excitation energies, one must consider the finite temperature generalization of Eqn. 1.10[11]

$$\lambda = N(0) \sum_{kk'}^{(FS)} \sum_{n \succ n'}^{\infty} \sum_{n'}^{\infty} \frac{|\langle n|\langle k'| \left((\nabla V \cdot \delta \mathbf{R})_{R_0} + \nabla_i \nabla_j V \delta \mathbf{R}_i \delta \mathbf{R}_j \right) |k\rangle |n'\rangle|^2}{E_n - E_{n'}} (f_{n'} - f_n),$$

(1.30)

where f_n is the thermal weighing factor $\frac{e^{-\beta E_n}}{\sum_i e^{-\beta E_i}}$. For $T \gg (E_1 - E_0)$, the difference between thermal factors for the ground state and first excites state goes to zero faster than the energy level difference, so that the contribution to λ from the nearly degenerate pair of lowest levels actually goes to zero in the limit of an infinitely deep double well. The sum over the other transitions in Eqn. 1.30 yields the same result as that calculated for contributions from two decoupled potentials, with no reference to double well character.

1.3   Small anharmonic perturbations

The effect of small quartic anharmonicities can be studied within perturbation theory. Take a potential of the form

$$V(x) = Ax^2 + Bx^4$$

(1.31)

with $A > 0$ and the quartic term in some sense small. The perturbation will shift the average phonon frequency to first order in the relevant expansion parameter, namely the ratio of the energies contained in the quartic and quadratic parts of the oscillation,

$$\sqrt{\langle \omega^2 \rangle} = \sqrt{\frac{2A}{M}} \left(1 + K \frac{B}{A^{\frac{3}{2}} M^{\frac{1}{2}}} \right).$$

(1.32)

The order-unity prefactor K is initially left indeterminate. Eqn. 1.13 then determines the mass dependence of λ,

$$\lambda_M = K \frac{B}{A^{\frac{3}{2}} M^{\frac{1}{2}}}. \tag{1.33}$$

The prefactor K can be approximated by a perturbation calculation using the first term in the sum for $\langle \omega^2 \rangle$, which yields K=1.06. Numerical solutions of Schrodinger's equation for weakly anharmonic wells produce K=1.05±0.01, confirming the perturbative approach. These numerical studies also allow a rough evaluation of the coefficient of the next term in the perturbation expansion, producing

$$\lambda_M = 1.05 \frac{B}{A^{\frac{3}{2}} M^{\frac{1}{2}}} - 5 \frac{B^2}{A^3 M}. \tag{1.34}$$

We obtain a shift in α as expressed by Eqn. 1.18. A positive quartic part will decrease the isotope effect, with the reduction most pronounced for light ions. A negative quartic part, on the other hand, will produce $\lambda_M < 0$ and thereby increase α above $\frac{1}{2}$.

The influence of various forms of anharmonicity can be conveniently summarized in terms of the level spacing of the eigenstates in the local vibrational potential. Those potentials which yield excited state level spacings greater than the ground state to first excited state spacing will yield $\lambda_M < 0$ and thereby depress α below 0.5. Examples of such potentials are a square well and a harmonic potential hardened by a positive quartic part. In contrast, potentials in which the higher states are closer together than the first two states will yield $\lambda_M > 0.0$ and $\alpha > 0.5$. This unusual state of affairs comes about when a harmonic potential is softened by a small negative quartic part.

Before considering specific numerical results it is useful to briefly survey the qualitative behavior of multiple-well potentials. Starting with the perfectly harmonic potential, we have an exactly solvable quantum mechanics problem with equally spaced energy levels. If the oscillator mass is increased, the wavefunction contracts and the oscillator mass is less influenced by the steep walls of the potential. The eigenstates decrease in energy proportional to the inverse square root of the mass ($\omega_M = -0.5$). Now consider distorting

the potential by introducing very weak local minima some distance from the central well. In this situation the outer portions of the potential are weaker. When the oscillator mass is increased, these outer portions again have less influence on the dynamics of the oscillator mass. However, since these regions are weaker to begin with, the total mass dependence of the energy levels is weaker $(0 > \omega_M > -0.5)$. This argument is perturbative in nature. As the outer wells strengthen they begin to dominate the situation and the perturbative picture breaks down. Eventually the dynamics will be dominated by the near-degeneracy of the levels in the two outer wells. In this situation, increasing the oscillator mass will drop the wavefunction farther into the two outer wells and bring the system ever closer to a true degeneracy. In consequence, the level spacing becomes very sensitive to the mass $(\omega_M < -0.5)$. As explained previously, finite temperature effects eventually wash out the near-degenerate level spacings and the system returns to near-harmonic behavior in each of the two now-independent outer wells. Such is the life of an anharmonic multiple-well potential.

1.4   Illustrative Numerical Results

Local density approximation total energy results for a buckling vibration of the chain oxygens[12] in $YBa_2Cu_3O_7$ yield a vibrational potential which provides an illustrative numerical example of a strongly anharmonic potential. The calculations yield a double well potential with roughly 0.7 Å between the two wells, each of depth $\sim$150 K below the central maximum. Motivated by this results, we examine a series of anharmonic potentials of the form

$$V(x) = Ax^2 + Bx^4 \qquad (1.35)$$

with distances between the wells of 0.5, 0.7, and 1.0 Å and well depths of 60, 150, and 300K. The summations over excited oscillator states were carried over six levels, with the dominant contribution in all cases coming from the first term. The oscillator mass is the

mass of an oxygen atom.

In addition to λ_M and ω_M, the numerical calculations also provide $\langle \omega^2 \rangle$ and the ionic part of λ (without the electronic prefactor). In accordance with the results of Hardy and Flocken[11] the ionic part of λ increases substantially from the shallow, narrow wells to the deep, wide potentials. However, this variation is primarily caused by a decrease in phonon frequencies; possible variations in the electronic prefactor for different potentials rule out a direct comparison between the λ calculations for different potentials. We circumvent this difficulty by exploiting the relationship between λ and α given by Eqn. 1.18. For the value α equal to 0.02, the accepted value for $YBa_2Cu_3O_7$, we obtain an estimate for λ, should this chain buckling mode dominate the superconductivity. (Note that this is an unlikely scenario- other modes would be likely to contribute strongly. The present example is primarily for illustrative purposes.) The transition temperature T_c is calculated from Eqn. 1.17.

Imposing the $\alpha = 0.02$ condition produces moderately strong coupling λ's. The largest λ's occur for wide, deep wells in which λ is most sensitive to M. This trend is elucidated by Eqn. 1.19, which shows λ to be proportional to λ_M in the strong coupling limit under the condition $\alpha = 0$. As noted above, the wide, deep wells also have the largest ionic contributions to the electron-phonon coupling, as computed directly from the numerical solutions of Schrodinger's equation without imposing the $\alpha = 0.02$ condition.

For the particular potentials under analysis the large separation between wells leads to a very small average phonon frequency. Increasing the depth of the wells does not substantially increase the average frequency, since the limit of infinitely deep double wells yields a degeneracy between the ground state and the first excited state. This small average phonon frequency limits the critical temperature to roughly 15 K. For some potentials, the transition temperature is only 2 or 3 K. If λ is increased by hand to produce T_c on the order of 90K, then α will approach the strong-coupling limit of one half, at variance with experimental results. A one dimensional incarnation of the chain oxygen vibrational

potential, although of strongly anharmonic form, is too wide to yield simultaneous high T_c and small α. Note that a closely related calculation by Dreschler and Plakida[13] produces similar results for the variation of α with λ.

In a two dimensional double well, the angular momentum term will break the near degeneracy of the lowest levels, increasing the average frequency. Such a situation would increase T_c above the values quoted above. Since the O(1) atoms lie in chains, we will examine two dimensional anharmonic buckling motion out of the chain. A neutron powder diffraction study has measured large thermal ellipsoids for the O(1) atoms. The ellipsoids are pancake-shaped and oriented perpendicular to the Cu-O bonds[14], providing some support for the hypothesis of a two-dimensional anharmonicity. Unfortunately, the experimental situation is unclear; other diffraction studies have yielded a cigar-shaped thermal ellipsoid[15, 16]12 13, a result inconsistent with a soft two-dimensional double well. The standard description of phonons would necessitate a separation of the two-dimensional mode into two coupled one-dimensional modes. The Einstein scheme avoids the problem of analyzing such strongly coupled modes. Analysis of such two dimensional mode yields roughly a factor of 3 increase in the phonon frequency (and transition temperature), implying that a narrow form of the chain buckling mode could make a significant contribution on the order of 10-30 K to the high T_c

Chapter 2

Anharmonicity and Superconductivity in PdH

The PdH(D) materials provide a relatively simple system in which to study unusual isotope effects. The transition temperature of PdH is roughly 9 K. The substitution of deuterium for hydrogen increases the transition temperature to 11.5 K[17][18]. A compilation of superconducting tunneling, neutron scattering, electrical resistivity, Raman scattering, thermal expansion, elastic moduli, and point-contact spectroscopy data yields an anharmonicity of 12%±5% in the hydrogen(deuterium)-palladium potential (i.e. $\frac{M_H\omega_H^2}{M_D\omega_D^2} = 1.12 \pm 0.05$)[19]. We examine this system within a simple model of anharmonic phonons in superconductivity, assuming an Einstein phonon spectrum with linear electron-phonon coupling at T=0 and using the isotropic Eliashberg equations.

Pseudopotential frozen phonon studies of the q=0 optical phonon in PdH yield a strongly anharmonic potential[20]. Total energy calculations for displacements of the hydrogen sublattice in the (001), (110) and (111) directions can be fit to a symmetry-preserving polynomial of the form

$$V(x,y,z) = c_2(x^2 + y^2 + z^2) + c_4(x^4 + y^4 + z^4) + c_{22}(x^2y^2 + y^2z^2 + x^2z^2), \qquad (2.1)$$

yielding the values $c_2 = 2.800\frac{mRyd}{au}$, $c_4 = 14.88\frac{mRyd}{au}$ and $c_{22} = -9.77\frac{mRyd}{au}$[20]. We have solved for the lowest excited states in a local potential of this form by expansion of the Hamiltonian in the eigenstates of a three-dimensional harmonic oscillator. Diagonalization of the resultant 512x512 matrix produces eigenvalues in excellent agreement with those derived by fourier expansion of the potential[20]. The energy difference between the ground state and the first excited state is calculated to be 62 meV for PdH, 42 meV for PdD and 32 meV for PdT, as compared to experimental values of 60 meV and 40 meV for PdH and

PdD. The mass dependence of the linear electron-phonon coupling constant λ is calculated in accord with Eqn. 1.10[21][22], yielding the following ratios,

$$\frac{\lambda_{PdD}}{\lambda_{PdH}} = 1.19 \tag{2.2}$$

and

$$\frac{\lambda_{PdT}}{\lambda_{PdH}} = 1.27. \tag{2.3}$$

The value of λ is a free parameter which must be fitted to experimental data for the transition temperature of one of the isotopes. Assuming a Coulomb repulsion parameter $\mu^* = 0.11$, we fit the magnitude of the electron-phonon coupling to the 9.0 K transition temperature of PdH, yielding $\lambda_{PdH} = 0.52$. This model then predicts $\lambda = 0.62$ and $T_c=11.4$ for PdD, in reasonable agreement with the experimental results. The model predicts $\lambda = 0.67$ and $T_c=11.4$ for PdT. The effect of the anharmonicity is much reduced for PdT for several reasons. The mass dependence of λ for this interatomic potential is slightly weaker for the larger mass of the tritium atom. In addition, the effect of anharmonicity on the isotope effect is in general reduced the stronger the electron-phonon coupling, which is largest in the PdT system. Finally, the fractional increase in mass from PdD to PdT is 50%, as opposed to 100% for the change from PdH to PdD.

In treating only the q=0 optical phonon we have ignored the effects of both the acoustic modes and dispersion in the optical modes. A significant contribution to the electron-phonon coupling from the acoustic modes, which are assumed to be less anharmonic, would decrease the calculated negative isotope effect. Previous theoretical treatments of the electron-phonon interaction in PdH[19] assert that the bulk of the coupling results from the optical modes. The effect of optical mode dispersion is more difficult to analyze. Neutron scattering measurement on $PdD_{0.63}$ yield significant dispersion for this mode[23]. In general, the frequencies at finite q are from 0 to 50% larger then the q=0 mode. These higher frequencies imply that the electron-phonon coupling should be somewhat smaller then that calculated from just the q=0 mode. If the anharmonicity is roughly constant

as a function of wavevector, this smaller value of λ will produce a larger negative isotope effect, counteracting the effect of finite coupling from harmonic acoustic modes.

One can make use of additional experimental data on the inverse isotope effect in PdH, namely the pressure and concentration dependence of T_c. The transition temperatures of PdH_x, PdD_x and PdT_x are plotted in Fig. 2.1[24]. Note that other experiments[17][18] have yielded different values of both T_c and α at the highest hydrogen concentrations, suggesting possible differences in sample quality. The theoretical results are fit to the data for PdH_x, completely determining the theoretical transition temperatures for PdD_x and PdT_x. We have assumed that the anharmonicity is constant over this doping range, as suggested by a comparison of frozen phonon calculations for PdH and PdH_4[25]. Since numerical solution of the Eliashberg equations is inefficient at small values of λ, the McMillan equation[2] with a modified phonon frequency prefactor[26] of Eqn. 1.9 is used to calculate T_c,

$$T_c = \frac{\langle \omega_{log} \rangle}{1.20} \exp\left[-\frac{1.04(1 + \lambda)}{\lambda - \mu^*(1 + 0.62\lambda)} \right]. \tag{2.4}$$

The agreement is good for PdD. On the other hand, the results for PdT are significantly below the experimental values. A possible source of error in the treatment of PdT is the Born-Oppenheimer approximation, which has been implicitly used in the frozen phonon calculation to separate the dynamics of the hydrogen and palladium atoms. This approximation should be least accurate for the heaviest isotope. Other possible explanations could invoke phonon dispersion or variations in μ^* between materials. Unfortunately, the experimental results for T_c in PdT are sparse. A more complete evaluation of the theory awaits additional experimental data. Numerical solution of the Eliashberg equations produces similar results, with a slightly larger slope for the T_c vs. x curve for PdD_x.

The transition temperature for PdH and PdD decreases with pressure at a rate of roughly 0.05k/kbar up to pressures of 40 kbar[27]. Unfortunately, we know of no frozen phonon calculations in this pressure range. However, the results for PdH_4 with unre-
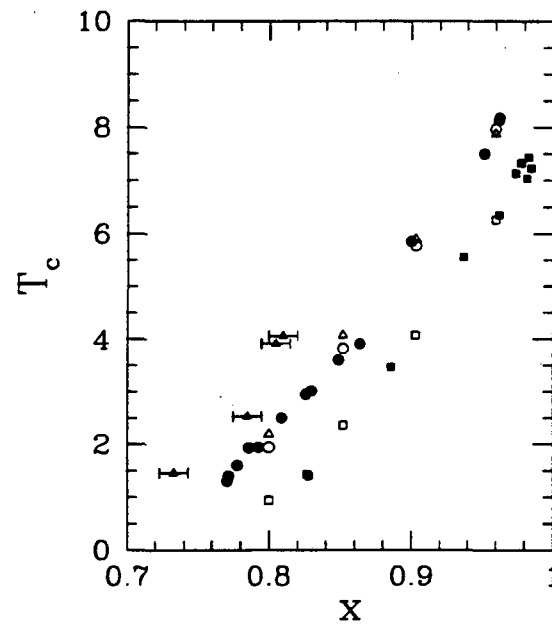
Figure 2.1: Theoretical calculation of T_c versus hydrogen isotope concentration in PdH_x ($\square$), PdD_x ($\bigcirc$) and PdT_x ($\triangle$). Corresponding filled polygons are experimental results.

laxed lattice constant provide an estimate of the interatomic potential for a 3.2% lattice contraction[20]. This contraction corresponds to a pressure of roughly 180 kbar, outside the range of experimental results. However, the theoretical potential at 180 kbar has almost identical anharmonicity to that at ambient pressures, with only a shift in phonon frequency from 62 meV (40 meV) to 83 mev (54 meV) for PdH (PdD). If we scale the phonon frequency linearly with pressure, we obtain a frequency of 66.6 meV (43.1 meV) for PdH (PdD) at 45 kbar, at which pressure the experimental value of T_c is 6.3 K (8.7 K). Fitting to a value of $\lambda_{PdH} = 0.47$, we obtain a theoretical transition temperature of 6.2 K (8.7 K) for PdH (PdD).

In summary, a model of anharmonicity that takes into account the novel mass dependences of both the phonon frequencies and the electron-phonon coupling can account for differences in T_c between PdH_x and PdD_x at both ambient and finite applied pressure. Theoretical results are at variance with preliminary data for T_c in PdT_x.

Chapter 3

Anharmonic Phonons and Dopant Effects in HTS

The proper theoretical description of high temperature superconductivity[28] in the copper-oxide based superconductors remains a mystery. Proposed (sometimes nonexclusive) models include large bipolarons, exchange of antiferromagnetic spin fluctuations, marginal Fermi liquid (a somewhat generic term)[29], spin-charge separation in a Luttinger liquid[30], and various numerical explorations of the Hubbard model around half filling. Most of these mechanisms require a novel non-Fermi liquid electronic ground state in which electron correlation plays a critical role. One could be easily put off by this wealth of models- in pragmatic terms, what chance is there that any given novel mechanism is relevant, given the breadth of mechanisms proposed? A different strategy presents itself. We have one very successful theory of lower-temperature superconductivity, the BCS theory with electron-phonon coupling. Perhaps it is most reasonable to approach the puzzle of high temperature superconductivity from known territory, extending the BCS theory into a regime of novel phonon dynamics and unusual Fermi liquid anisotropy. A more exotic mechanism may very well be correct. However, the choice of *which* exotic mechanism is problematic! The most likely single mechanism remains an extension of the BCS theory.

Numerous experimental and theoretical results bear on the importance of the electron-phonon interaction in the high-temperature superconductors. Theoretical calculations indicate that the roughly 30 K transition temperature of the non-cuprate superconductor $Ba_{1-x}K_xBiO_3$ can be explained with standard electron-phonon coupling[31, 32]. Tunnelling measurements on $Ba_{1-x}K_xBiO_3$ and $Nd_{2-x}Ce_xCuO_4$ support a phonon-mediated mechanism[33]. Tunnelling results for $YBa_2Cu_3O_7$ can be also interpreted as suggesting strong electron-phonon coupling[34]. Indications of phonon softening at the supercon-

ducting transition suggest significant coupling between the electrons and certain phonon modes[35][36]. Several anomalous properties of the high temperature superconductors can be explained within an electron-phonon framework. For example, the lack of a coherence peak in the nuclear spin relaxation time can be ascribed to strong coupling effects[37]. Proponents of novel mechanisms often assert that the temperature-dependent resistivity is too linear to be electron-phonon in origin. However, standard electron-phonon mediated resistivity is quite linear above some fraction of the Debye temperature. In addition, converting the resistivity data from constant pressure to constant volume introduces nonlinearity[38], rendering invalidate the argument that the resistivity in the high-T_c materials is "too linear" to be phonons. The lack of saturation in high-temperature resistivity data appears to be inconsistent with a system having strong electron-phonon coupling[195]. However, explanations exist incorporating anisotropic electron-phonon coupling[40] or variations in the Fermi velocity across the Fermi surface[41].

The primary difficulty with an electron-phonon mediated mechanism for superconductivity is the small isotope effect of the highest T_c materials. For example, $YBa_2Cu_3O_7$ has $\alpha \approx 0.02$ and $T_c \approx 90$ K[42]. Anharmonicity provides a means to circumvent this objection in that anharmonic effects can yield decreased isotope effects, particularly for the most strongly anharmonic potentials which would likely be associated with the highest T_c's. Impurity doping of the optimized (highest-T_c) materials generally yields increased α while depressing T_c. In particular $La_{2-x}Sr_xCuO_4$ shows large variations in the isotope effect exponent with Sr doping[43]. Clearly it is difficult to explain the large isotope effect at certain Sr concentrations if phonons do not contribute to the pairing. Other varieties of doping, such as Pr for Y[44] or Fe for Cu[45], also produce high-T_c materials with isotope effect exponents on the order of one half.

More direct evidence exists of unusual phonon dynamics in these materials. Measurements of pair distribution functions from neutron scattering imply local structural distortions of the Cu-O planes in $La_{2-x}Sr_xCuO_4$, $Tl_2Ba_2CaCu_2O_8$ and $Nd_{2-x}Ce_xCuO_4$

corresponding to buckling motions of oxygen atoms perpendicular to the Cu-O bond,[46] with indications that the distortions are dynamic[47]. X-ray absorption fine structure (EXAFS) experiments can be explained with a double well potential of width 0.13 Å for c-axis motions of the apical oxygens in $YBa_2Cu_3O_7$ [48], with other plausible interpretations in terms of local structural distortions[49]. Infrared measurements indicate that the mode in question has at Q=0 a frequency well above that derived from a local-mode solution to the proposed double well potential. However, the infrared measurements probe Q=0, whereas the EXAFS experiment probes the local lattice dynamics. Ion channelling experiments also indicate strong anharmonicity for vibrations involving the apical oxygens and the copper atoms[50]. The proximity of superconductivity to structural phase transitions, especially in the $La_{2-x}M_xCuO_4$ systems, suggests the relevance of soft modes associated with these transitions. On the theoretical front, frozen phonon calculations yield multiple-well potentials for octahedral tilt motions in $La_{2-x}M_xCuO_2$[51] and for buckling motions in the oxygen chains of $YBa_2Cu_3O_7$[12]. X-ray scattering data suggests such a buckling distortion in the chains[52]. In addition, frozen phonon calculations yield a strongly anharmonic, but not multiple-well, potential for the zone-center oxygen E_u mode in $La_{2-x}Sr_xCuO_2$[56].

The evidence for unusual electron-phonon dynamics is substantial, leading to the question of which particular modes are plausible candidates for strong electron-phonon coupling and anharmonic dynamics. Many of the modes discussed above do not represent generic modes of the high-T_c oxides. The octahedral tilt is unique to materials with a single Cu-O plane. The chain buckling is unique to $YBa_2Cu_3O_7$. There are several reasons why the apical oxygen vibrations are unlikely to be the sole contributor to an anharmonic mechanism. They are present as at most low concentrations of defects[53] in several high-T_c materials, such as the "parent compound" electron-doped superconductor $Sr_{1-x}Nd_xCuO_2$ with T_c=40 K[54]. A model based entirely on these modes may have difficulty accounting for the increase in T_c with increasing number of Cu-O planes in the thallium and bismuth

compounds, since the number of apical oxygens remains fixed as Cu-O planes are added. In addition, T_c seems to be highest in materials where the apical have the least influence, the single layer compounds with large apical oxygen to planar copper distances and the multiple layer compounds with a decreased proportion of apical oxygens to copper-oxide planes. Finally, within our formalism, the potential suggested by the EXAFS experiments can be shown to produce T_c of roughly 30 or 40 K for $\alpha \approx 0.0$, suggesting at most a supporting role for the apical oxygen modes. Although the apical oxygens could conceivably play a major role, the most generic modes of possible multiple-well character would involve oxygen atoms in the Cu-O sheets, either buckling perpendicular to the sheets (similar to the in-plane behavior of the octahedral tilt mode), buckling parallel to the sheets (modes which are experimentally inaccessible due to screening), or vibrations along the bond (which could have double-well character at high Q due to Peierls-like distortions.)

3.1 Optimally doped compounds

We first examine the optimally doped compounds to evaluate whether reasonable phonon anharmonicity can account for high T_c and small α. Single plane Cu-O materials such as $La_{2-x}Ba_xCuO_4$ possess planar oxygen buckling motions some of which can be described as semi-rigid tilt modes of the Cu-O octahedra, a fairly low-frequency motion. The multiple-plane compounds such as $YBa_2Cu_3O_7$ and $Bi_2Ba_2CaCu_2O_8$ do not possess such a tilt mode. The relevant oxygen bucklings should have a higher frequency, since the Cu-O skeleton must be nonrigidly distorted. These bucklings could be associated with narrow multiple well potentials, as could vibrations along the Cu-O bond. In addition, the multiple-plane compounds are likely to possess increased two dimensionality, which could be related to the relative prominence of anomalous phonon or electron dynamics (such as Peierls distortions). The possibilities of higher phonon frequency and increased coupling and anharmonicity due to two dimensionality are consistent with the higher T_c's

and generally lower α's in the multiple layer compounds.

If the hypothetical multiple-well potentials corresponded to Raman active or c-axis polarized IR active modes, then one would expect an anomalously strong isotope effect in the frequencies of these modes under $^{16}O \rightarrow ^{18}O$ substitution. The few isotopic IR and Raman studies to date do not show anharmonic behavior, implying that a plausible anharmonic potential must either correspond to high-Q mode or an in-plane displacement which is not experimentally accessible due to screening.

Several forms of multiple-well potential can produce a near-vanishing α for T_c on the order of 90K. A quadrupolar potential of the form

$$V(r,\theta) = ar^2 + cr^6 + br^4 \cos 2\theta. \tag{3.1}$$

with a distance of 0.14 Å between the origin and the outer minima can produce $\alpha = 0.0$ with T_c of 100K and $\lambda = 1.3$. A one-dimensional double well of the form

$$V(x) = ax^2 + bx^4 \tag{3.2}$$

with a distance of 0.12 Å between outer minima of depth 900 K produces a T_c of ~100K with $\lambda = 2$ and $\alpha \sim 0$. A two-dimensional triple well potential of the form

$$V(r) = ar^2 + br^4 + cr^6 \tag{3.3}$$

can produce a T_c of roughly 80K with $\lambda = 2.0$ and $\alpha = 0.09$ for a distance of 0.10 Å between the outer minima. These examples assume linear electron-phonon coupling. A quadratically coupled double-well potential with a distance of 0.25 Å between the minima can also account for high T_c and small α with similar parameter values.

A related quadrupolar form with distance of ~ 0.09Å between the wells and a well depth of 2000 K with $\lambda = 1.4$ yields a transition temperature of 110K and an isotope effect exponent of $\alpha = 0.04$. Quartic and sixth order potentials also depress the isotope effect exponent. For example, a purely sixth order linearly coupled one-dimensional potential of

the form V(x)=3.0×10^8 x^6 meV for x measured in Å produces T$_c$ of 93 K for α=0.01. For each of these potentials the ionic mass has been set equal to the mass of an oxygen atom. The Coulomb pseudopotential μ^* has been fixed at 0.1; the results are relatively insensitive to this parameter. Large values of T$_c$ and near-zero isotope effects are consistent with electron-phonon coupling within this model of anharmonic phonons.

These narrow, high frequency potentials do not generally have large values for the ionic part of λ, since the dipole matrix elements are not very large. Within this model, a large electron-phonon coupling for these potentials would have its origin in the electronic prefactor. Possible sources of a large electron-phonon coupling are local field effects[55], ionic properties,[56] or Peierls-type distortions[57].

3.2 Application to La$_{2-x}$Sr$_x$CuO$_4$

We will examine the possible effects of anharmonicity on the superconducting isotope effects in high temperature superconductivity, in particular La$_{2-x}$M$_x$CuO$_4$ and doped YBa$_2$Cu$_3$O$_7$. Measurements of the isotope effect exponent α in La$_{2-x}$Sr$_x$CuO$_4$[43, 58] have yielded $\alpha > 0.5$ for x in the range 0.10 to 0.13 and $\alpha \approx 0.1$ for larger values of x. T$_c$ for M=Ba, Sr is depressed for x≈0.125, with a much larger depression for Ba than for Sr. A model based on a Van Hove singularity in the electronic density of states near the Fermi level has been proposed to account for this unusual behavior[59] In contrast, Crawford et al.[58] have speculated that an incipient phase transition from the orthorhombic to the low temperature tetragonal structure could produce these anomalous values of α.

More recent evidence suggests that the peak in T$_c$ and the unusual behavior of α is closely associated with the electronic doping level of x=0.125. Th^{1+} doping in La$_{2-x-y}$Ba$_x$Th$_y$CuO$_4$, which shifts the $\frac{1}{8}$ doping level to larger Sr concentrations, shifts both the incipient phase transition and the suppression of T$_c$ to x-y=0.125[60]. High resolution synchotron x-ray diffraction of La$_{2-x}$Ba$_x$CuO$_4$suggests that the transition at

x=0.125 is distinct from the LTO-LTT transition. Pair distribution function data indicates that the LTO phase is simply an incoherent superposition of differently oriented LTT phases on a $\sim$10Å length scale, yielding a crystallographically orthorhombic phase which is locally tetragonal[61, 62]. Finally, Nd doping, which stabilizes the LTT phase, yields a material in which the superconductivity is uncorrelated with the LTT instability[63]. A $\sqrt{2} \times \sqrt{2}$ superlattice instability could be modulated by a wavevector which could span the Fermi surface for x$\approx$0.125, yielding an electronically-driven change in lattice dynamics. Finally, copper isotope effect experiments on the same system[64] yield nearly identical variation in isotope effect with doping, a surprising result that argues against a structural phase transition and by default towards an electronic mechanism for the instability. These results taken as a whole suggest anomalous electronically driven lattice dynamics near x=0.125, not necessarily a true lattice instability, but more generally a qualitative change in the vibrational potential, a substantial change in phonon anharmonicity. We will model of the effects of anharmonicity on the isotope effect to flesh out this speculation.

Preliminary numerical study of one-dimensional modes indicates that a triple well potential with weak outer minima can produce $\alpha > 0.5$, while a triple well with stronger outer minima can produce $\alpha < 0.5$, in analogy with the results obtained from quartic perturbations of a harmonic potential. These results suggest a simple explanation for the variation in α with Sr concentration. Frozen phonon calculations[51] suggest that a multiple-well interionic potential is associated with the orthorhombic/high temperature tetragonal transition. We will assume a similar form of potential for the low temperature anomaly. As the Sr concentration is increased, the system approaches the regime of anomalous behavior. We posit a multiple-well potential in which the outer wells deepen as the anomaly is approached, evolving from a softened quadratic potential to a true multiple-well potential. Note that the model to this point generalizes to any form of boson-exchange superconductivity with evolving anharmonic dynamics. This model can reproduce the experimentally observed variations in both T_c and α.

We begin the expression for the electron-phonon coupling λ at zero temperature,

$$\lambda = N(0) \sum_{kk'}^{(FS)} \sum_{n=1}^{\infty} \frac{|\langle n|M_{kk'}|0\rangle|^2}{E_n - E_0}, \tag{3.4}$$

which describes coupling between the lattice ground state $|0\rangle$ and all excited states $|n\rangle$ with energy E_n[8]. Taking linear coupling, we obtain

$$M_{kk'} = \langle k'| \left(\nabla V \cdot \delta\mathbf{R}\right)_{R_0} |k\rangle, \tag{3.5}$$

where V(r) is the electron-ion potential, $|k\rangle$ and $|k'\rangle$ are electronic states, and $\delta\mathbf{R}$ is the ionic displacement from the equilibrium position R_0. Assuming a two-dimensional phonon mode with displacements in the x and y directions, we can recast Eqn. 3.5 in the form

$$M_{kk'} = \langle k'| \frac{dV}{dx}x + \frac{dV}{dy}y |k\rangle. \tag{3.6}$$

Following McMillan[2], we factorize Eq (1) to obtain a computationally convenient form,

$$\lambda = \sum_{n=1}^{\infty} \left[\langle I_x^2 \rangle \frac{|\langle n|x|0\rangle|^2}{E_n - E_0} + \langle I_x I_y \rangle \frac{|\langle n|x|0\rangle||\langle n|y|0\rangle|}{E_n - E_0} + \langle I_y^2 \rangle \frac{|\langle n|y|0\rangle|^2}{E_n - E_0} \right] \tag{3.7}$$

where the prefactors $\langle I_x^2 \rangle$, $\langle I_x I_y \rangle$, and $\langle I_y^2 \rangle$ contain the electronic contributions and the summation involves matrix elements between phonon states. Numerical results indicate that the cross term $\langle I_x I_y \rangle$ is negligible for physically plausible potentials suitably oriented with respect to the coordinate axes. For simplicity, the other prefactors, $\langle I_x^2 \rangle$ and $\langle I_y^2 \rangle$, will be assumed to be equal. The case of unequal prefactors can be easily treated, but the interesting physics is contained in the simpler situation. In any case, the prefactors should be equal for any potential symmetric in x and y.

In this instance, the various energy level differences (E_n-E_0) and their contributions to λ are used to create an expression for $\alpha^2 F$,

$$\alpha^2 F(\omega) = \sum_{n=1}^{\infty} \lambda_n \omega_n \delta(\omega - \omega_n), \tag{3.8}$$

where

$$\lambda_n = \langle I_x^2 \rangle \left[\frac{|\langle n|x|0\rangle|^2}{E_n - E_0} + \frac{|\langle n|y|0\rangle|^2}{E_n - E_0} \right] \tag{3.9}$$
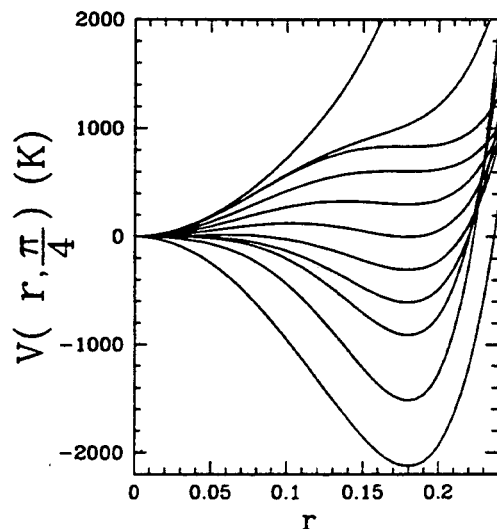
Figure 3.1: The r-dependence of the various quadrupolar potentials studied, plotted for $\theta = \frac{\pi}{4}$. Sr concentration increases with increasing depth.

and

$$\omega_n = E_n - E_0. \tag{3.10}$$

This strategy avoids the inherent inaccuracies in reducing the phonon frequency distribution to a single moment such as $\langle \omega^2 \rangle$ or $\langle \omega_{log} \rangle$. In any case, the potentials examined will be dominated by the transition between the ground state and the first excited state, so that this energy difference will closely approximate the average phonon frequency.

The two-dimensional Schrödinger equation is solved by expansion with a basis of solutions to the harmonic oscillator. For each energy level, we calculate the mass dependence of ω_n and λ_n and solve the Eliashberg equations numerically to obtain T_c and α.

We start with an in depth analysis of potentials of the form

$$V(r, \theta) = ar^2 + cr^6 + br^4 \cos 2\theta. \tag{3.11}$$

When b<0, the last term produces triple wells for $\theta = \frac{\pi}{4}, \frac{3\pi}{4}$. In the case a<0, the first term is also multiplied by the cosine factor to produce double wells at these angles. The potential

examined should not be considered a quantitative prediction, but rather a representative example. Related multiple-well potentials to be discussed will yield similar results. To ensure convergence, we used from 22 to 28 basis functions in the x and y directions. We consider a series of potentials with the outer wells increasing in strength. A plot of the r-dependence of these potentials for $\theta = \frac{\pi}{4}$ is given in Fig. 3.1. The outer minima are located at ± 0.18 Å, in accord with the frozen-phonon calculations[51]. The difficulty of defining normal modes in a strongly anharmonic system clouds the choice of effective oscillator mass. We initially assume an oscillator mass equal to the mass of an oxygen atom before turning to other possibilities. The relevance of the linear term in the electron-phonon coupling for the phonon mode governing the orthorhombic to low temperature tetragonal transition has been questioned within the context of a tight-binding model[65, 66]. Should the electronic anomaly have similar symmetry, the linear term in the coupling would be suppressed. However, the tight binding model ignores long range non-rigid ion contributions, which are important in the cuprate materials[67]. In addition, the strong anharmonicity of the system complicates any considerations based on the symmetry of a harmonically-defined normal mode. Finally, the symmetry argument only applies at a particular value of phonon wavevector; phonons of slightly different wavevector will not be constrained to zero linear coupling. We begin with the assumption that the linear term dominates the interaction, relaxing this assumption in later examples. After this in depth discussion, various related potentials will be examined to indicate the generic nature of the behavior observed for evolving multiple well potentials.

To calculate T_c and α, we need a value for λ to set the scale for $\alpha^2 F$. The formalism provides only the ionic part of λ, without the electronic prefactor. This ionic part of λ increases with decreasing boson frequency, which corresponds to increasing Sr concentration. However, one cannot assume that the electronic prefactor will remain constant as the Sr concentration changes. For each potential, λ is adjusted to fit T_c. We also take $\mu^* = 0.10$ for each potential. The theoretical results are not particularly sensitive to the
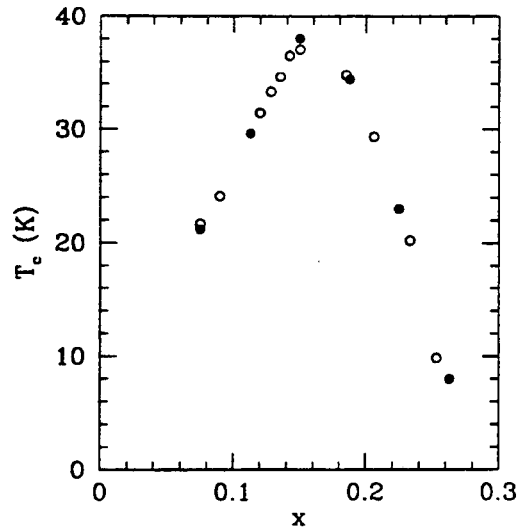
Figure 3.2: T_c versus Sr concentration x in $La_{2-x}Sr_xCuO_4$ for the interionic potentials shown in Fig. 3.1 The depth of the potentials increases with increasing Sr concentration. Solid circles are the data of Crawford et al.[58] Open circles are the theoretical results.

value of μ^*. Note that the coefficients a, b and c of Eqn. 3.11 were not adjusted in order to better match the data, but merely chosen to produce a smooth evolution in the shape of the potential. The results for T_c, α and λ are plotted in Figs. 3.2 through 3.4, along with the data of Crawford et al.[58].

The horizontal scale of the theoretical results is arbitrary, since we do not have a quantitative relation between Sr concentration and the particular potentials chosen. The ordering of the potentials is fixed, but the horizontal scale is chosen to match the experimental data.

The proposed variation in potentials can produce an isotope parameter that starts near 0.5, increases, and then falls to a constant value below 0.5, with T_c peaking just after α has dropped. For each potential we have one free parameter, λ, with which to fit both T_c and α. This fit produces λ's which increase with increasing Sr concentration, as does the
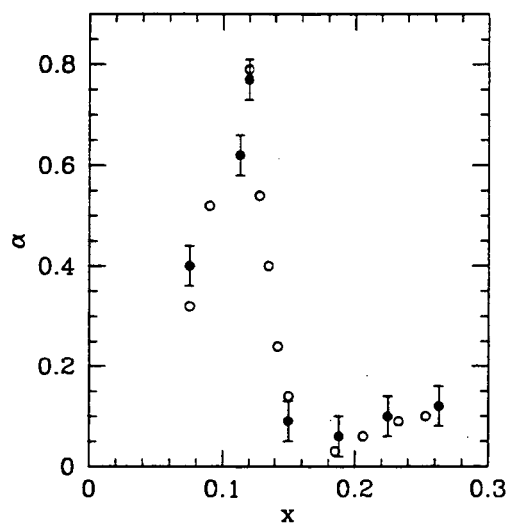
Figure 3.3: The isotope exponent α versus x in $La_{2-x}Sr_xCuO_4$ for the interionic potentials shown in Fig. 3.1. Solid circles are the data of Crawford et al.[58] Open circles are the theoretical results.
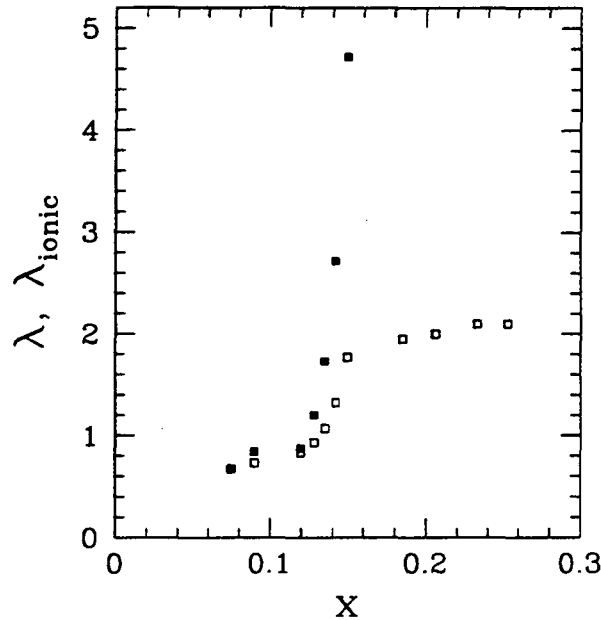
Figure 3.4: Electron-phonon coupling λ versus x in $La_{2-x}Sr_xCuO_4$ for the quadrupolar potentials shown in Fig. 3.1. Open squares are the λ used to determine T_c and α. Solid squares are the ionic part of λ, scaled so that the first point coincides with the value of λ used in the calculations of T_c and α. The value of λ_{ionic} continues to increase for higher Sr concentrations, with values of 6.4, 7.9, 12.1, and 36.6 for the higher Sr concentrations considered.

calculated ionic part of lambda alone, as shown in Fig. 3.4. The ionic contribution has been scaled so that the first points of either curve coincide.

It is not surprising that the ionic part of λ increases much more quickly than the total λ since the variations in the electronic contributions to λ have not been taken into account. In fact, a comparison of the fitted values of λ with the ionic contributions to λ provides a measure of the variation in the electronic prefactor $\langle I_x^2 \rangle$. The electronic prefactor begins to fall steeply at the same point that α decreases, possibly indicating a drop in the density of states at the Fermi level, or a significant change in the character of

the electronic wavefunctions, or possibly a deviation from a nesting condition operative near the optimal T_c.

The quadratic part of the potentials with $\alpha > 0.5$ is sufficient to produce a phonon frequency of roughly 500K. The tetragonal to orthorhombic soft phonon mode is experimentally observed at roughly 50 to 100 K[68, 69] a considerably lower frequency. Although one might expect the lower temperature transition to be mediated by a mode of similar frequency, the actual anharmonic potential considered here is not directly related to this phonon distortion, but instead a posited vibrational source of the anomalous electronic dynamics at a doping level of $\frac{1}{8}$. In any case, phonon modes with smaller q than the mode driving the orthorhombic to low temperature tetragonal transition could have higher frequencies, since these modes do not involve rigid motion of Cu-O octahedra. Other buckling motions of the oxygen atoms out of the Cu-O plane could also produce higher frequency multiple well modes. We note that a mode of lower frequency than that considered would produce less pronounced variations in λ than that exhibited in Fig. 3.4.

At low doping, the potential studied is roughly harmonic. As the doping increases, it is assumed that the outer relative minima form and steadily increase in depth until a quadrupolar potential is obtained. A potential ambiguity in this analysis involves the difficulty of defining normal modes in a strongly anharmonic system, a problem with implications for the choice of effective oscillator mass. In the preceding analysis, the oscillator mass has been taken as the mass of an oxygen atom, instead of the reduced mass of the Cu-O octahedra, as would be valid for a harmonic normal mode. Such an assumption is plausible if the octahedra do not act as purely rigid entities.

In deference to the peculiarities of anharmonic lattices, we now discuss the behavior of several non-quadrupolar multiple well potentials with analogous behavior under doping. Similar behavior for a wide class of potentials would lend some support to the physical relevance of this simplified model of anharmonicity. We do not propose that any particular potential is relevant to $La_{2-x}Sr_xCuO_4$; we merely wish to exhibit a general feature of

multiple-well potentials.

We examine one-dimensional double and triple wells. We examine a triple well in the y direction coupled to a harmonic well in the x-direction,

$$V(x,y) = ax^2 + (by^2 + cy^4 + dy^6)\frac{1}{fx^2 + 1} + gy^2\frac{fx^2}{fx^2 + 1}. \qquad (3.12)$$

We have also computed the variations in T_c and α for a two dimensional triple well potential of the form

$$V(r^2) = ar^2 + br^4 + cr^6 \qquad (3.13)$$

with

$$r^2 = x^2 + y^2. \qquad (3.14)$$

Finally, we have examined the behavior of an octapolar potential of similar dimensions.

Since symmetry considerations within a tight binding model suggest that the linear term in the electron-phonon coupling is absent for the orthorhombic tilt mode at the relevant phonon wavevector, these potentials have been examined for both linear and quadratic coupling. Linear terms are included because they will be nonzero for wavevectors near, but not exactly equal to, the relevant phonon $\vec{q}$. In the linear case, the distances between the outer minima of the potentials were taken in the range 0.22 to 0.25 Å. Quadratic coupling encompasses primarily the transition from the ground state of the local oscillator to the second excited state. The dominance of higher energy transitions implies that a quadratically coupled potential will be wider than a linearly coupled potential that yields the same frequency scale for the electron-phonon coupling. For this reason, the interwell widths for quadraticly coupled potentials are in the range 0.4 to 0.5 Å. For each potential the oscillator mass has been taken as the mass of an oxygen atom. A larger oscillator mass would require a narrower potential.

For each of these potentials we obtain α near 0.5 at low doping, with a maximum substantially above 0.5 at intermediate doping (near the maximum T_c), and a relatively constant value around 0.1 for high doping, The transition temperature peaks at ~30K for

intermediate doping. In the linear case, the electron-phonon coupling λ increases from ∼1.0 for low doping, to ∼2.0 for the highest doping. [65]. The variation in λ is much less pronounced for quadratic coupling, with $\lambda \sim 2$ for all doping concentrations. For a more detailed account of the behavior of a particular evolving anharmonic mode, we refer to a previous publication[22]. The similar behavior of a broad class of potentials mitigates somewhat against the concerns stemming from the inadequacies of a harmonic normal mode description.

We now examine in detail a particular pair of quadratically coupled octapolar potentials which are designed to more closely mimic the structural instabilities which arise upon doping. The potentials are displayed in Figs. 3.5 and 3.6, which show the potential energy for tilts of the semi-rigid Cu-O octahedra. The magnitude of the tilt is expressed in terms of the displacement of the apical oxygen. Tilts towards the corners of the plot correspond to distortions to the low temperature tetragonal (LTT) phase, while tilts to the sides correspond to the low temperature orthorhombic (LTO) phase. In this case, the oscillator mass is set to 2.6 times the mass of an oxygen atom, the normal mode mass for the displacement in question and likely the most realistic choice for oscillator mass. The potential of Fig. 3.5 is designed to mimic situation at doping levels of x∼ 0.12 near the incipient transition to the low temperature tetragonal phase. The wells in the LTO directions have a minimum at 150 K, compared to a value of -75 K for the LTT wells. The deeper wells in the LTT directions is consistent with the low-temperature stability of the LTT phase at this doping level. The central well is set at zero energy. In the second potential the outer wells have flattened out, corresponding to the increased stability of the high temperature tetragonal phase at higher doping levels. Assuming purely quadratic electron-phonon coupling, the first potential yields $T_c = 35$ K and $\alpha = 0.8$ for a fitted value of $\lambda = 2.0$. The second potential yields $T_c = 26$ K and $\alpha = 0.07$ for the same value of λ. In both cases the Coulomb repulsion is set at $\mu^* = 0.13$. The results are similar for μ^* in the range 0.05 to 0.30. Without detailed experimental information on the form of the

tilt mode potential, the present calculations must be considered as plausibility arguments. However, the theoretical results are fairly robust to variations in the detailed form of these potentials. The important qualitative features are the comparable magnitudes of the central and outer wells for the first potential and the flatness of the second potential.

This choice for the evolution of the potentials assumes that the low temperature tetragonal phase becomes more favored with increasing strontium concentration. Qualitatively similar results could be obtained from a slightly different series of potentials which are identical to the potentials discussed for strontium concentrations less than x=0.12, but then flatten out for higher concentrations. This series of potentials produce a maximally stable low temperature tetragonal phase around x=0.12.

Before concluding, we again touch on the point that the eigenvectors of harmonic normal modes will not be normal modes of the anharmonic system. These vibrations should in general couple to other modes, although it is possible that certain vibrations could act as effectively independent oscillators, as seen in certain metal hydrides[70, 71]. Consequently, the standard normal mode masses for these vibrations will not necessarily be physically relevant. Noting these difficulties, interpretation of frozen phonon calculations for particular atomic displacements should proceed with caution, especially for complicated atomic distortions, such as the orthorhombic tilt mode. In the particular case of the orthorhombic tilt, the strong dependence of the structural transition temperatures on ionic size[58, 72] implies that the anharmonic potential is strongly doping dependent, even for ions of the same valence. The frozen phonon calculation for La_2CuO_4[51] should be treated as a representative example of the form of potential for this mode, not a definitive conclusion.

Numerous theories for high-T_c can explain an anomalously weak isotope effect. However, few can explain strong variations in α both above and below 0.5. A multiple well anharmonic potential appears to be a likely candidate for a mechanism for such a variation. The reproducible measurement of $\alpha > 0.5$ in $La_{2-x}Sr_xCuO_4$ has put significant
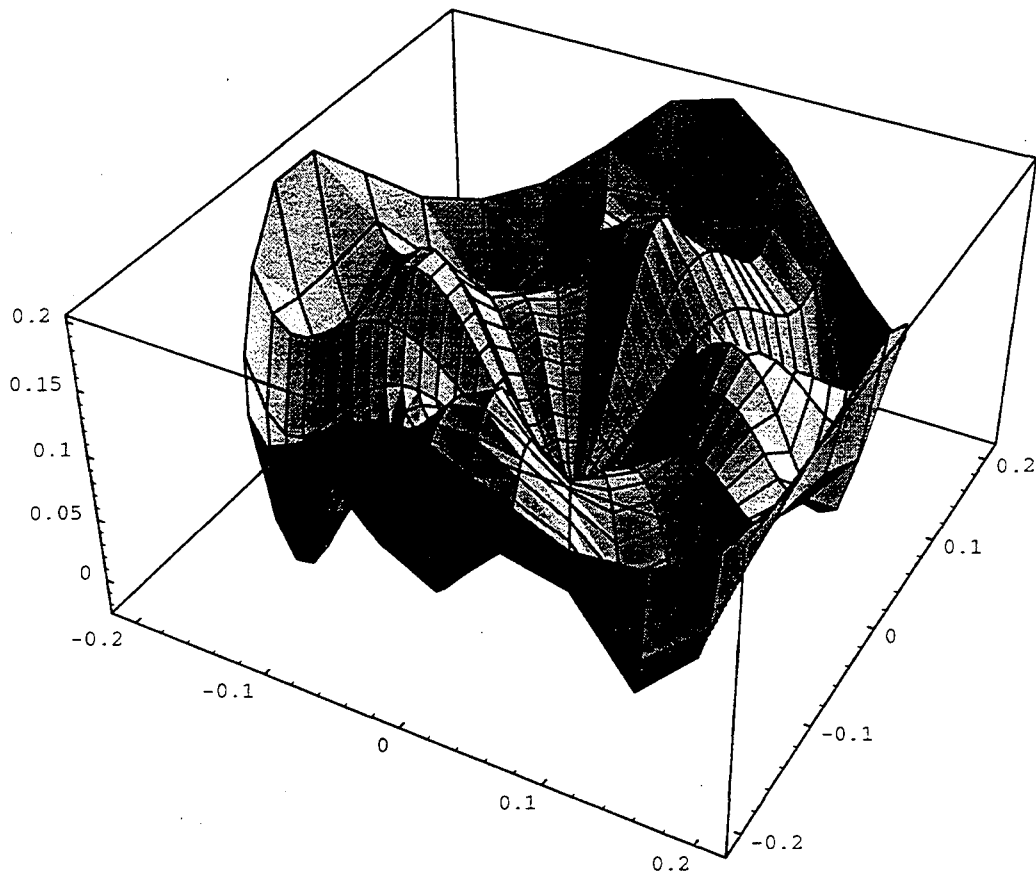
Figure 3.5: Model octapolar potential for octahedral tilts in $La_{1.88}Sr_{0.12}CuO_4$. Units on the horizontal axis are Å. On the vertical axis one unit equals 3000 K.
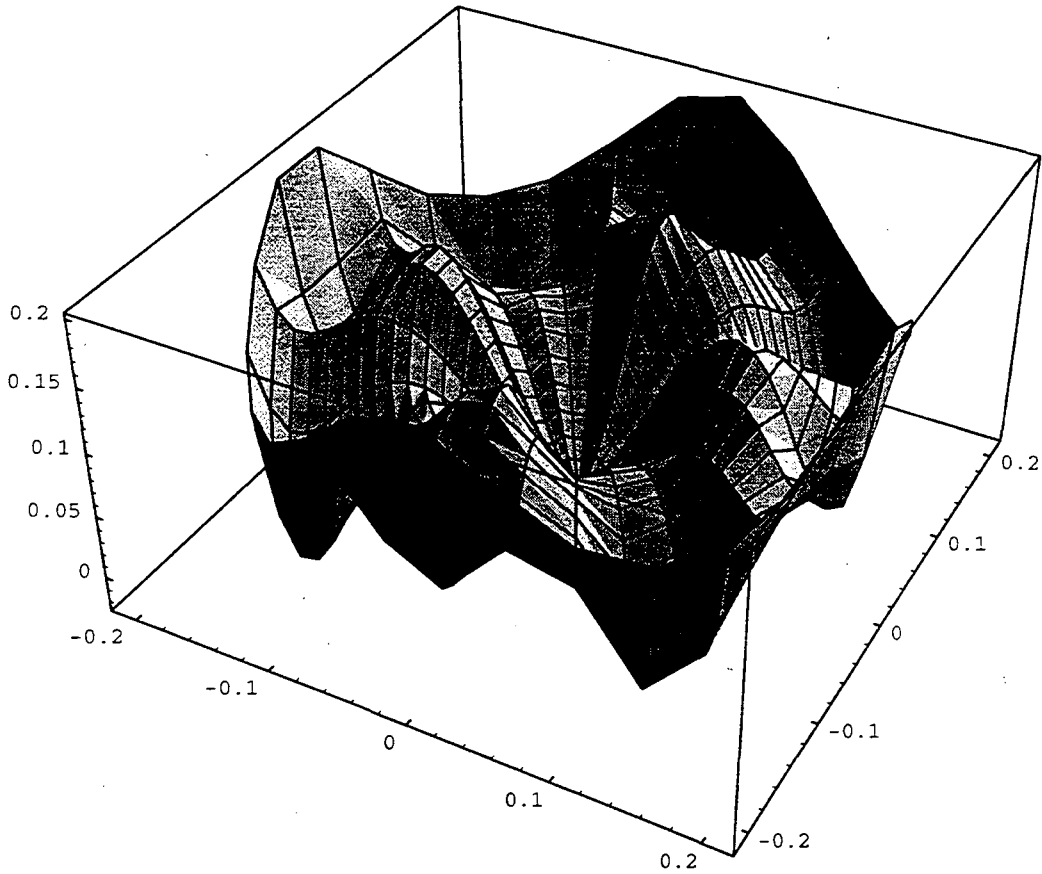
Figure 3.6: Model octapolar potential for octahedral tilts in $La_{2-x}Sr_xCuO_4$ near the LTO→HTT transition. Units on the horizontal axis are Å. For the vertical axis one unit equals 3000 K.

constraints on possible theories of high temperature superconductivity.

3.3 The higher-T_c oxides

The highest T_c oxides generally exhibit small positive oxygen isotope effects. However, when one introduces dopants which decrease T_c, the isotope effect generally increases, often attaining values on the order of the canonical $\alpha = 0.5$. We now consider the suboptimal compounds, discerning whether the physical effects of the dopant atoms are consistent with various models for the isotope effect in these materials. Specifically, the results of the model calculations are compared with the high temperature superconductors $Y_{1-x}Pr_xBa_2Cu_3O_{7-\delta}$ and $YBa_2Cu_{3-x}M_xO_{7-\delta}$ with M=Zn, Ni or Fe.

3.3.1 Interplanar coupling of vibrational modes

We first examine the possible ramifications of interplanar coupling of planar oxygen buckling motions in the multiple-plane compounds to see if the interplanar coupling correlates in a meaningful way with the generally higher T_c of the multiple plane compounds. We will assume a double-well potential for independent oxygen motions perpendicular to the plane with Hooke's law coupling between oxygen atoms in adjacent planes. The Hamiltonian is

$$H = \frac{p_1^2}{2m} + \frac{p_2^2}{2m} + a(q_1^2 + q_2^2) + b(\frac{1}{2}q_1^4 + 3q_1^2q_2^2 + \frac{1}{2}q_2^4) + 2cq_2^2, \qquad (3.15)$$

where we have decomposed the motion into the harmonic normal mode coordinates. The coordinate q_1 describes oxygen atoms moving vertically in unison, while q_2 measures the amplitude of anticorrelated motion. We ignore intraplanar dispersion. As the coupling constant c is increased, the degenerate ground state splits. In the lower frequency mode the atoms move roughly in unison such that the interplanar coupling is less important while the higher frequency mode is dominated by the interplanar spring. Although the average frequency of these two modes increases as the coupling becomes stronger, the

lower frequency mode (with the larger λ due to the inverse dependence of λ on phonon frequency) dominates the superconductivity, such that the net effect on T_c is minor. The higher frequency mode, being dominated by the presumed harmonic interplanar coupling, acquires reduced anharmonicity, suggesting that interplanar coupling is not the source of the higher T_c's in the multiplanar compounds, since reduced anharmonicity is inconsistent with the small isotope effect. Although not a plausible source of T_c enhancement, harmonic interplanar coupling should not cause any significant depression in T_c since it leaves the dominant lower frequency mode nearly unchanged.

3.4   Isotope Effect Under Cu site Substitution

Substitution of Zn, Fe, or Ni for Cu in $YBa_2Cu_3O_7$ and $YBa_2Cu_4O_8$ has a dramatic influence on the isotope effect[45]. Fig. 3.7 reproduces experimental results for T_c versus α for various concentrations of these dopants. The substantial difference between the effects of the different dopants in the two compounds could be ascribed to different substitutional sites for the dopant atoms, however, we do not examine this issue in detail here (chapter 4 has a brief discussion of different substituent sites). Instead, we present a simple generic model of evolving anharmonicity which is consistent with the data. This model provides a mechanism alternative to magnetic pair breaking from the addition of transition metal dopants.

In particular, let us assume that the addition of dopant atoms destroys the delicate structural or electronic situation in the Cu-O planes necessary to produce anharmonic modes. Although one might expect the effect of the dopants to be rather inhomogeneous, we will model it by an evolving effective anharmonic potential shown in Fig. 3.8. The variation in the potential is reminiscent of that examined in our model of $La_{2-x}Sr_xCuO_4$. However, in this case the central well disappears more quickly so that the potential never produces $\alpha > 0.5$. We model the effect of different dopants by assuming that each dopant
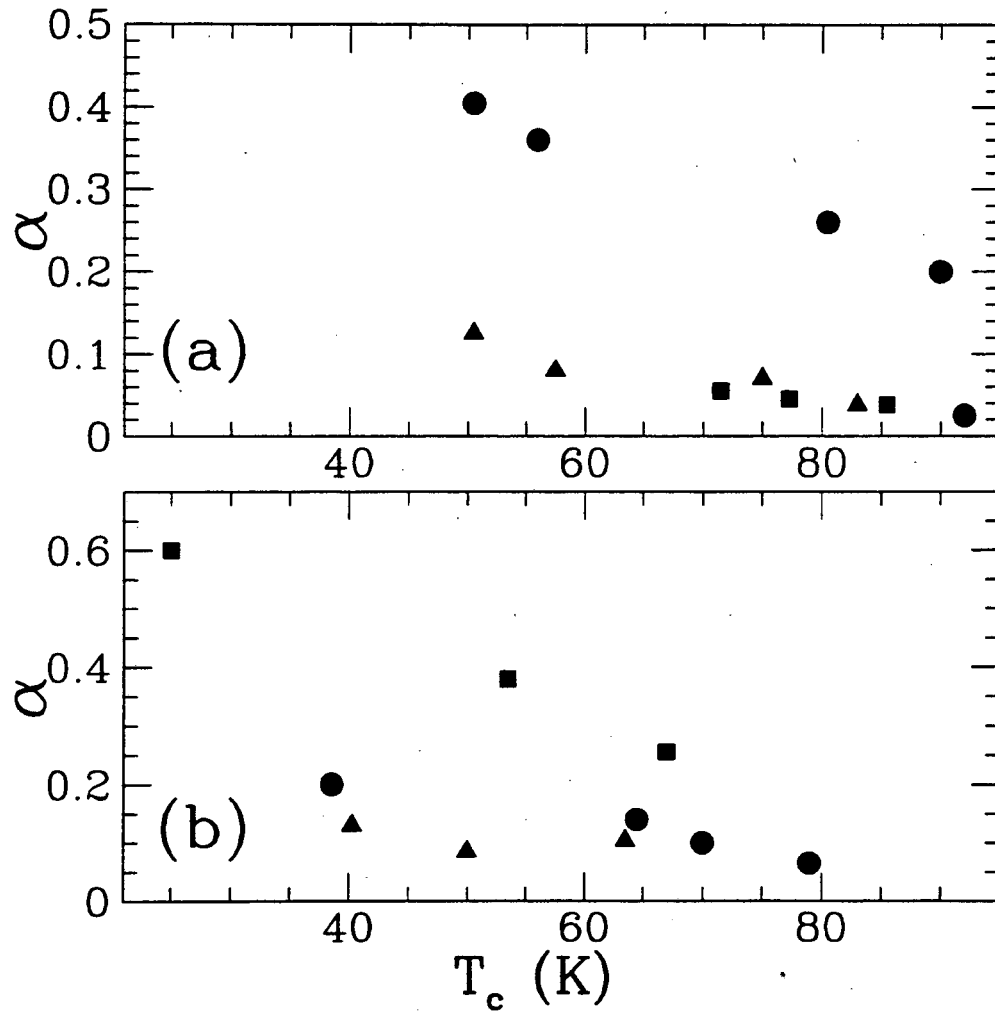
Figure 3.7: Experimental results[45] for the variation of α versus T_c for substitution of M=Fe (circles), Ni (squares) and Zn (triangles) for Cu in (a) $YBa_2Cu_{3-x}M_xO_{7-\delta}$ and (b) $YBa_2Cu_{4-x}M_xO_8$.

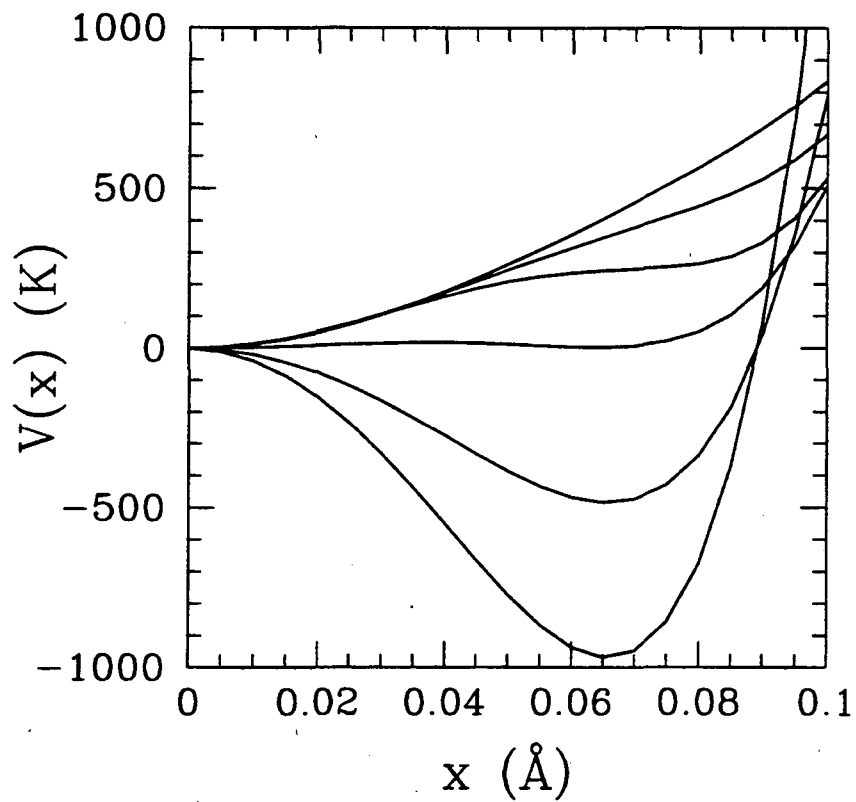Figure 3.8: Series of effective anharmonic potentials used to model Cu-site substitution in $YBa_2Cu_{3-x}M_xO_{7-\delta}$ and $YBa_2Cu_{4-x}M_xO_8$. The potentials become less anharmonic as the doping level increases.

produces the same series of potentials, but with varying values of λ, starting with $\lambda = 2.0$ for the undoped material. Referring to Fig. 3.9, we have produced five theoretical curves. For dopant A, λ decreases from 2.0 to 1.20 at the lowest T_c value. For dopants B, C, D and E, the final values of λ are 0.95, 0.70, 0.45 and 0.20 respectively. In each case, the intermediate values of λ are obtained from a linear interpolation. The swift suppression of λ for dopant E produces an isotope effect that actually decreases with doping. The results for the variation in α with T_c span the breadth of the experimental behavior, with a similar functional form. However, considering the rather ad hoc nature of the proposed potentials, this result should be considered simply a plausibility argument for the relevance of anharmonicity to the variations in T_c and α with Cu-site doping the the high-T_c oxides.

3.5 Isotope Effect in $Y_{1-x}Pr_xBa_2Cu_3O_7$

In general, the substitution of other rare earths for the Y in $YBa_2Cu_3O_7$ has little effect on the superconducting properties[73][74][75][76]. However, introduction of Pr dramatically lowers T_c, with superconductivity disappearing for Pr concentrations above 50% [77][78][79]. Several models have been proposed to explain this behavior. If the Pr ions are tetravalent, they would reduce the carrier concentration thereby suppressing superconductivity. On the other hand, since the 4f electrons of Pr are more extended than those of other magnetic rare earths, they may hybridize more readily and cause magnetic pair breaking. The experimental situation is somewhat unclear, with various results suggesting pair breaking, [80][81][82][83] valency,[82][84] or carrier localization[85]. As the Pr concentration is increased, T_c decreases and the isotope effect exponent increases monotonically, reaching 0.5 for a Pr concentration of 50% and a T_c of 30 K[44]. We have examined the implications of the pair breaking and valency models for reduction of T_c from the viewpoint of both an anharmonic model of high T_c and a nonspecific electronic model.

For illustrative purposes, we model pair breaking in the simplest possible manner.
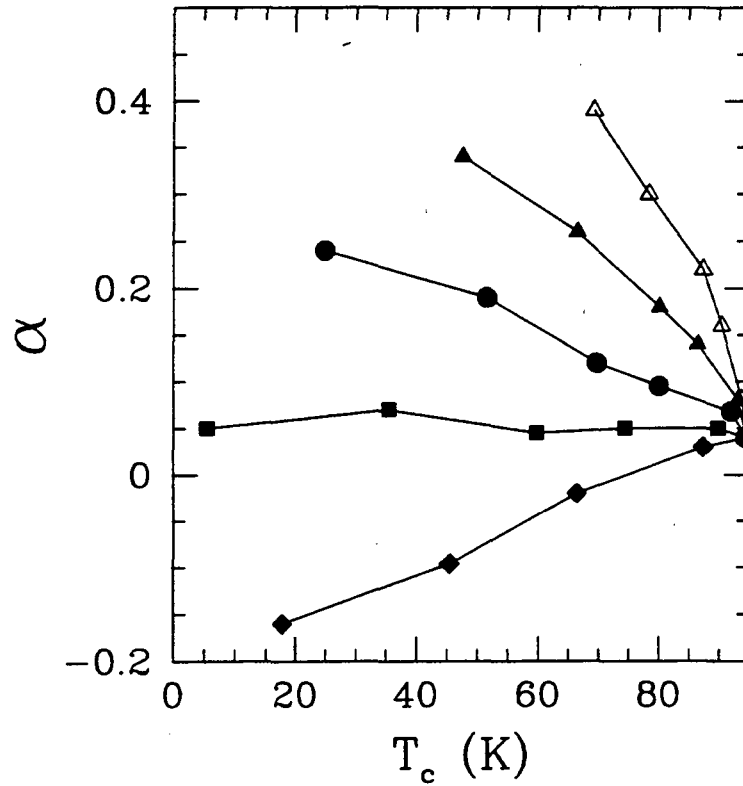
Figure 3.9: Results for α versus T_c for the potentials of Fig. 3.8. Five different effects of

doping on the electron-phonon coupling were considered, as discussed in the text: dopant

A (open triangles), dopant B (filled triangles), dopant C (filled circles), dopant D (filled

squares) and dopant E (filled diamonds).

In the limit of a weak concentration of magnetic ions, the superconducting transition temperature is reduced by a mass-independent factor[86].

$$T_c = T_c^0 - A. \tag{3.16}$$

If we extrapolate this simple form to higher concentrations of magnetic ions, we obtain a simple qualitative formula for the isotope effect exponent as a function of T_c.

$$\alpha = \alpha_0 \left(\frac{T_c^0}{T_c} \right). \tag{3.17}$$

The increase in α upon doping is critically dependent upon the "baseline" isotope effect α_0 present at maximum T_c. A more thorough treatment of pair breaking yields qualitatively similar behavior, with a more pronounced variation in α with decreasing T_c and a similar sensitivity to the value of α_0[87]. Within a pair breaking treatment, large values of α_0 (roughly $\alpha_0 \sim 0.08$) are necessary to fit the experimental results for T_c versus α, at variance with the best characterized experimental results, which yield $\alpha = 0.02$[10]. Although some experiments have yielded $\alpha \sim 0.08$, the present consensus is that $\alpha \approx 0.02$[88].

Turning to the valency mechanism, we examine an electronic model, with a mass-independent electronic mode at 120 K and a harmonic phonon contribution at 480 K. A fit of a higher frequency electronic mode to the experimental values of T_c and α would produce a value of the electron-phonon coupling which is at variance with experimental results[89]. Within the valency model, we assume that the decrease in T_c is caused by a decrease in λ which must be apportioned between the electronic and phonon-mediated terms in α^2F. If we assume that both terms are reduced by the same multiplicative factor, then the electronic mode will dominate for all values of T_c, keeping α small until superconductivity disappears. However, if the addition of Pr selectively depresses the electronic mechanism while leaving the phononic mechanism undisturbed, then α will increase somewhat as Pr is incorporated. Results for the valency model are presented in Fig. 3.10. The increase in α is generally insufficient to explain the experimental results
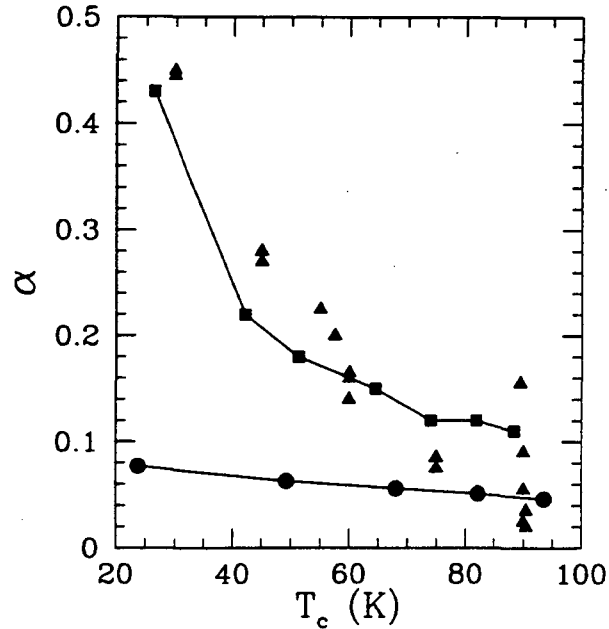
Figure 3.10: The relationship between α and T_c in $Y_{1-x}Pr_xBa_2CuO_7$ for a valence model of T_c suppression. Experimental data[44] (triangles) is compared with two electronic models, both with a 120 K mass-independent electronic mode and a 480 K harmonic phonon mode. One model (circles) has $\alpha(93K) = 0.04$ and $\mu^* = 0.10$, the other (squares) has $\alpha(93K) = 0.10$ and $\mu^* = 0.14$. In both cases, the doping selectively depresses the coupling to the electronic mechanism. Curves are intended as a guide for the eye.

unless the phononic contribution to the coupling is large enough so that the isotope effect exponent at maximum T_c is roughly 0.10, substantially greater than the experimental value of 0.02[10]. A study of models with higher frequency electronic modes yields similar results.

Treatments assuming magnetic pair breaking or selective suppression of a predominately electronic model yield too weak an increase in α with decreasing T_c if the "baseline" isotope effect at maximum T_c is taken to be $\alpha = 0.02$. Since the detailed behavior of an anharmonic phonon model under Pr doping is unclear, we do not present a particular

microscopic model. However, the previous discussion of Zn, Ni, and Fe doping indicates that strong variations in α are possible, even for a material with a vanishing isotope effect at maximum T_c.

The previous treatments have assumed that the density of states near the Fermi level is roughly constant. We note that a Van Hove singularity model for high T_c superconductivity[90] appears consistent with the dependence of T_c on α. A thorough treatment of this situation is given by Carbotte et al. [91][92] The effects of the valency model can be interpreted as a shift in the Fermi level away from the Van Hove singularity. As the singularity begins to leave the region $\pm\Omega_{Debye}$ from the fermi level, the isotope exponent increases, since a small change in Ω_{Debye} will produce a large change in the total number of states within Ω_{Debye} of the fermi level. Meanwhile, T_c will decrease since the singularity is leaving the region in which electron-phonon coupling is operative. If the peak of the singularity crosses the Ω_{Debye} threshold, one would expect α to peak, and then decrease. Perhaps a careful examination of α for the lowest values of T_c will reveal such a decrease in α. However, the Van Hove singularity model has several serious shortcomings as an explanation of high temperature superconductivity,[93] such as increased screening of the electron-phonon vertex and disorder broadening of the singular peak.

In sum, if the suppression of T_c in $Y_{1-x}Pr_xBa_2CuO_7$ is due to valency effects, then a anharmonic model with doping-dependent anharmonicity could reproduce the experimental data on the isotope effect. Under the same assumption, an electronic mechanism with a small phonon contribution is inconsistent with the small value of the isotope effect at maximum T_c. A mechanism based on magnetic pair breaking also appears to fall victim to the small isotope effect at maximum T_c.

3.6   Smoking Guns of Anharmonicity

Direct detection of strong phonon anharmonicity in the high-T_c oxides would con-

stitute strong evidence that an electron-anharmonic phonon mediated mechanism is the source of high transition temperatures and small isotope effects. Unfortunately, phonon phase space is large, and the region of anharmonicity may be relatively small. Optical measurements, which show no evidence of anharmonicity, probe near phonon wavevector q=0. Inelastic neutron scattering, which probes the entire phonon Brillouin zone, detects anomalous behavior near the zone edge for an optical branch near 50 meV in $YBa_2Cu_3O_7$ [94]. An extra branch appears near the zone edge and broadens while rapidly decreasing in frequency, behavior characteristic of strong anharmonicity. A true smoking gun of anharmonicity would be direct measurement of the mass dependence of the phonon frequency, and preferably λ as well. Such a measurement could in theory be acquired via inelastic neutron scattering or an extraction of $\alpha^2F(\omega)$ from high quality tunnelling data. Unfortunately such a measurement probably be difficult or impossible due to the broadness of strongly anharmonic modes. Another signal of multiple-well behavior is a deviation from Debye-like behavior in the low-temperature specific heat. This anomaly, which is seen in amorphous glasses and other complex structures, arises from a picture in which the multiple-well potentials are treated as an ensemble of two-level systems, yielding a specific heat linear in temperature. In a metal with such two-level systems this behavior may be masked by the linear electronic specific heat. The energy gap in a superconductor leads to an exponential contribution to the specific heat which may be easier to separate from a anomalous linear two-level contribution. However, the multiple wells under consideration for high temperature superconductors are not quite in this two-level limit, suggesting that this sign of anharmonicity may not be a promising avenue of exploration. In contrast, a significant mass dependence to λ should show up relatively clearly in a mass dependent gap ratio $\frac{2\Delta}{kT_c}$. Under O^{18} substitution, λ would increase, so that this ratio should also increase. For plausible values of the anharmonicity, we estimate a 5-10% increase in $\frac{2\Delta}{kT_c}$ for complete $^{16}O \rightarrow ^{18}O$ substitution, if anharmonic effects are relevant for the high-temperature superconductivity.

Another footprint of anharmonicity is a downturn in the high temperature resistivity. Once again, however, nature conspires to obscure the effect. First, resistivity saturation has a similar signature (and in fact, anharmonicity may be a significant contributor to the microscopic mechanism behind the phenomenological description of resistivity saturation.) Second, strongly anisotropic systems may exhibit significant deviations between the electron-phonon coupling relevant to transport and that relevant to superconductivity, as will be discussed in chapter 5 of this thesis. The anharmonic modes, if they are suitably anisotropic, may be invisible to transport measurements. The best candidate for the observation of significant anharmonic effects is the gap ratio.

In most theories of high temperature superconductivity a novel mass-independent mechanism is responsible for the large transition temperature. The small positive values of α are due to a small phonon contribution to T_c (see chapter 8). In general, a harmonic weak-coupled BCS model allows a negative value of α for a large value of μ^*, as revealed by a simple two square well model of superconductivity.

$$\alpha = \frac{1}{2}\left(1 - \left(\frac{\mu^*}{\lambda^* - \mu^*}\right)^2\right). \tag{3.18}$$

Substantial negative values of α are possible only for rather low T_c, since we have only weakly coupled phonons under the influence of a large μ^*. This single-mode result also applies to a primarily electronic model of high T_c with a small phonon admixture; the posited small phonon contribution cannot produce a large negative α. In contrast, the anharmonic phonon model could produce significant negative α. For example, a decrease in λ independent of other effects will depress the isotope effect for a multiple-well anharmonic model. However, if the decrease in λ is accompanied by a reduction in the anharmonicity, then the effect on α is unclear. The family of models examined in section 3.4 includes some in which decreased coupling strength is associated with larger α and others in which decreased λ is associated with decreased α. Similarly, the substitution of Ba or Sr for La in La_2CuO_4 changes the doping, therefore changing λ, but the same substitution also

drives the system towards an instability, suggesting a pronounced change in the character of the phonons. The best candidates for negative α are likely the highest T_c compounds, which are likely to have the largest presumptive anharmonicity, and also minor structural variants of optimized compounds, materials such as $YBa_{2-x}Sr_xCu_3O_7$, wherein the posited anharmonicity can be tweaked without major change in the doping level. Measurements on $Bi_{1.6}Pb_{0.4}Sr_2Ca_2Cu_3O_7$ with T_c of 108 K have produced a small negative isotope effect of -0.013±0.002,[45] which suggests the possibility of a larger negative isotope effect in the higher-T_c three layer thallium compounds. In addition, recent site selective isotope effect experiments indicate an inverse isotope effect for substitution of planar oxygen atoms in $YBa_2Cu_3O_7$ [95]. Finally, the *copper* isotope effect in oxygen deficient $YBa_2Cu_3O_7$ is substantial and negative[96]. The general trend of smaller α with higher T_c suggests materials under high pressure as another candidate for $\alpha < 0$. Unfortunately, higher-T_c's imply stronger coupling. Referring to the strong-coupling limit of an anharmonic α

$$\alpha = \frac{1}{2} - \frac{\lambda_M}{2\lambda}, \qquad (3.19)$$

we note that competition between increasing λ_M and increasing λ may prevent α from attaining large negative values.

The measurement of a strong negative isotope effect in a particular high-temperature superconductor would lend support to an anharmonic model, which provides a natural explanation of such an effect, as opposed to a mass-independent model with a small phonon admixture. In fairness, we note that a large negative isotope effect need not be an unambiguous signal of anharmonicity. For example, α-U has a T_c of roughly 2K and an isotope effect exponent of -2.2[99]. Such a strong negative isotope effect in a strongly coupling superconductor cannot be explained by a large μ^*, but instead requires a novel mechanism. One could of course appeal to a similarly novel mechanism for the high temperature superconductors. However, anharmonic effects, which can account for the anomalous values of α both above 0.5 and below 0.0, provide the most natural explanation for a significant

negative isotope effect in the high temperature superconducting oxides.

3.7 Conclusions

Strongly anharmonic multiple-well phonons provide a means to explain several unusual properties of the high temperature superconductors from within a BCS-like mechanism. Multiple-well potentials with a characteristic length scale on the order of 0.1 Å are consistent with a near-zero isotope effect and $T_c \sim 100K$. The counterbalancing effects of increased λ and increased λ_M suggest that α will generally decrease with increasing T_c. Eventually strong coupling effects or structural constraints assume prominence such that the decrease in α may bottom out near the maximum T_c's obtainable. Plausible variations of anharmonic potential with various forms of doping are consistent with most experimental measurements of α in nonoptimally doped materials. Finally, the observation of strong variation in isotope effects both above 0.5 and below 0.0 provides moderate support for an anharmonic mechanism of superconductivity in the high-T_c oxides.

Chapter 4

Site-Selective Isotope Effects in the HTS

Within an anharmonic phonon model of superconductivity the value $\alpha = 0.0$ is not special; the same anharmonic mechanism which could produce small near-zero positive isotope effects is also capable, upon a slight change in parameters, of producing inverse isotope effects. In other words, phonon anharmonicity does not suppress the absolute magnitude of the isotope effect, in contrast with a predominately electronic mechanism with a small phononic admixture, in which a large mass-independent electronic part would swamp the (presumably harmonic) phonon contribution and yield a small, positive isotope effect. The observation of an inverse isotope effect in the high T_c oxides would be evidence in favor of the anharmonic mechanism, which provides a natural explanation for $\alpha < 0.0$, as opposed to a joint electronic/phononic mechanism which provides a natural explanation for only $\alpha > 0.0$. The measurement of a site-selective isotope effect in YBa$_2$Cu$_3$O$_7$[95] has yielded an inverse isotope effect for planar oxygen substitution. In addition to providing moderate support for an anharmonic mechanism, this result provides an opportunity to estimate the relative magnitudes of possible harmonic and anharmonic contributions within a phonon-mediated model of superconductivity, thereby allowing predictions of the site-selective isotope effect in materials with depressed T_c due to doping[98].

Measurement of the selective isotope effect involves back-substitution of ^{16}O into the off-plane sites of a uniformly substituted ^{18}O sample[95]. Two samples, denoted #1 and #2, were studied. When fully substituted with ^{18}O, #1 and #2 showed standard isotope shifts of −0.20 K and −0.23 K respectively. However, the samples with ^{18}O in the planes and predominantly ^{16}O off-plane exhibit *increases* in T_c of 0.10 K and 0.14 K. [95] To clarify these results, we extrapolate the data to the case of perfect site selection. We make

a linear expansion in ΔT_c, the isotope shift, as a function of the change in the average oxygen mass in the planar (P) and off-planar (OP) positions,

$$\Delta T_c^{total} = \beta_P \Delta M_P + \beta_{OP} \Delta M_{OP}. \qquad (4.1)$$

Measurements of isotopic shifts in planar and apical oxygen Raman lines and thermogravimetric analysis allow an estimate of the average mass shifts. It is estimated [95] that the site-selective versions of #1 and #2 have 65% and 80% ^{16}O in the off-plane sites, which implies average off-plane oxygen masses of 16.7 and 16.4 amu respectively. The shifts in planar-mode Raman lines yield average plane-oxygen masses of 17.5 and 17.9 amu for the site selective samples. This estimate assumes that the modes in question are purely harmonic with frequencies linear in the square root of the average oscillator mass. The Raman shifts for the uniformly ^{18}O-substituted samples imply almost complete isotopic substitution. Using these results in Eqn. 4.1 and averaging the coefficients β_P and β_{OP} over the two samples, we obtain an isotope shift of +0.32 K for pure ^{18}O on-plane and pure ^{16}O off-plane, with $\Delta T_c = -0.22$ K for uniform substitution.

Application of an anharmonic phonon mechanism to the site-selective results requires a measure of physical interpretation to obtain a sufficiently constrained description. For the purposes of a descriptive model calculation, we interpret the decrease in T_c under ^{18}O substitution in the off-plane sites as due to a moderate harmonic contribution of off-plane oxygen phonons to the superconductivity. The increase in T_c under additional planar ^{18}O substitution results from a dominant anharmonic contribution from planar oxygen modes combined with a moderate harmonic planar contribution.

We now address the frequency distributions and relative weights of these disparate contributions. Significant shifts in the phonon density of states derived from inelastic neutron scattering[100] provide a means of estimating the frequency range of the dominant contributions to the electron-phonon coupling. Depression of T_c by oxygen deficiency, Zn doping, or Pr doping reduces the phonon density of states in the range 40-60 meV and

produces a new peak around 80 meV. Infrared reflectivity measurements support the interpretation of these changes in terms of electron-phonon coupling[101]. Assuming that anharmonic phonons dominate the superconductivity, these phonons can be assigned to the selectively depressed peaks in the range from 40-60 meV. The remaining density of states is assigned to harmonic modes. For simplicity, we assume that the non-oxygen vibrations occupy the range below 20 meV, and that the harmonic on- and off-plane contributions are equal in magnitude.

The experimental phonon density of states has been fitted to a sum of 26 Lorentzians, which adequately reproduce the salient features of the spectrum. The hypothetical anharmonic peaks are centered at 42 and 53 meV, the peak positions in the neutron scattering spectrum. At this point, the theory has three important free parameters: the total coupling strength λ, the anharmonic (AH) contribution to the coupling λ_{AH}, and the strength of the anharmonicity expressed in terms of the mass dependence of λ^{AH},

$$\lambda_M^{AH} \equiv \frac{M}{\lambda^{AH}} \frac{d\lambda^{AH}}{dM}, \qquad (4.2)$$

an expression discussed in greater detail in previous publications[102, 21]. These three parameters are determined by fitting to the experimental values of T_c, the uniform isotope shift and the site-selective isotope shift. This process yields $\lambda^{total}=2.45$, $\lambda^{AH}=1.72$, and $\lambda_M^{AH}=1.56$. The harmonic (H) contribution to λ decomposes into two parts, $\lambda_{oxygen}^H = 0.64$ from the peaks above 20 meV, and $\lambda_{non-oxygen}^H = 0.09$. For these calculations we have assumed $\mu^* = 0.12$; the effect of larger μ^* will be discussed below.

The value of λ^H is comparable with theoretical estimates of λ from analysis of phonon softening at the superconducting transition. [103, 104] It is also comparable with preliminary estimates of λ from *ab initio* band structure calculations of the electron-phonon coupling of harmonic modes[103]. Additional clues as to the magnitude of the harmonic part of the electron-phonon coupling can be gleaned from the T_c's and α's of transition metal doped samples. Under Fe doping into predominantly chain-Cu sites, α increases

substantially with only a small decrease in T_c[45]. Although iron seems a plausible magnetic pair breaker, the form of T_c versus α is inconsistent with a uniform pair breaking mechanism. However, since Fe primarily enters the chain Cu sites, the hypothetical pair breaking may selectively depress the chain contribution to T_c. This chain-localized pair breaking is reasonable because the c-axis coherence length in the high-T_c oxides is very small. In a superconductor with significant magnetic pair breaking, the change in T_c upon isotopic substitution is maximal when the magnetic pair breaking has almost completely destroyed the superconductivity of the isotopic sample with lower T_c. For this reason, near-complete pair breaking of a small chain contribution to T_c should yield a large increase in α for a small decrease in T_c.

As a simple example, consider modelling the chain contribution to T_c as an independent superconductor with T_c's of 5 K and 5.2 K for ^{18}O and ^{16}O respectively. Within a two square well model, pair breaking yields a depression in T_c given by[87]

$$ln\left(\frac{T_{co}}{T_c}\right) = \Psi\left(\rho + \frac{1}{2}\right) - \Psi(\rho),\tag{4.3}$$

where T_{co} is the transition temperature in the absence of pair breaking, Ψ is the digamma function and $\rho = \frac{1}{2\pi T_c \tau(1+\lambda)}$, where τ is the scattering time for magnetic pair breaking. Under strong pair breaking, one obtains T_c's of 0.01 K and 0.74 K, yielding a much larger isotopic shift in T_c. Taking this hypothetical 5 K superconductor as exemplary of the chain contribution to T_c indicates that a large change in ΔT_c can accompany a small change in the total T_c. The detailed accuracy of this calculation is limited by two effects: different contributions to T_c are not simply additive, and Fe dopants attract extra oxygen, suggesting a more complex influence of Fe doping on the superconducting properties. However, the qualitative considerations of selective pair breaking suggest a contribution of order 5 K to T_c from the Cu-O chains, consistent with a moderate off-plane contribution to λ. Ni doping in the chain Cu sites of $YBa_2Cu_{4-x}Ni_xO_8$ also yields a large increase in α for a small decrease in T_c,[45] suggesting that a similar mechanism

is operative in the 124 compounds.

An additional estimate of the harmonic contributions to λ is afforded by the Zn-doped compounds. Zn primarily enters the plane sites,[105] depressing T_c with only a small increase in α. For larger Zn concentrations, α increases sharply, reaching 0.3, a value consistent with a purely harmonic mechanism, for $T_c \sim 9$ K[106]. Assuming the absence of pair breaking, this result suggests a lower bound of roughly ~ 9 K for the total harmonic contribution to λ, which is again consistent with a moderate harmonic contribution to the electron-phonon coupling.

Although consideration of the results for Fe doping provides a useful clue as to the magnitude of off-plane contributions to the superconductivity, a reasonably clean theoretical discussion of selective isotope effects of doped materials within an anharmonic mechanism requires a system which is not clouded by the possibility of significant magnetic pair breaking. To this end, we concentrate on the systems where Sr and La are doped into the Ba site. We model the effect of doping as a decrease in both the magnitude of the anharmonicity, λ_M^{AH}, and the strength of the coupling to the anharmonic modes, λ^{AH}. In effect, we assume that the dopants perturb a relatively delicate situation that engenders multiple-well potentials. These two parameters are fixed by the experimental values of T_c and α, allowing a prediction of the site-selective isotope effect. The suppression of T_c due to doping is also correlated with a new phonon mode at 80 meV,[100] which is assumed to be harmonic. The results are insensitive to the detailed treatment of this mode.

The results of this analysis are summarized in Table 4.1. The primary qualitative result is that the difference in T_c between samples with different oxygen isotopes off-plane remains relatively constant as T_c is depressed by a non-pair breaking mechanism. This insensitivity results from the assumption that the doping primarily degrades the anharmonic modes. The harmonic off-plane modes are assumed to remain relatively unchanged under doping, and therefore contribute a nearly constant amount to the isotopic shift in T_c. This qualitative explanation suggests that the prediction should be relatively robust

Table 4.1: Analysis of La and Sr doped $YBa_2Cu_3O_7$. The values for total coupling strength λ, and strength of the anharmonicity λ_M have been fit to experimental results for T_c, α at the doping level in question, yielding a prediction for the site-selective isotope effect in the doped materials.

Material	x	T_c (K)	λ	λ_M	λ^{AH}	ΔT_c^P (K)	ΔT_c^{OP} (K)
$YBa_{2-x}La_xCu_3O_7$	0.0	92	2.45	1.56	1.7	+0.34	-0.56
$YBa_{2-x}La_xCu_3O_7$	~0.2	76	2.0	0.80	1.3	-1.0	-0.6
$YBa_{2-x}La_xCu_3O_7$	~0.3	57	1.6	0.40	0.9	-1.3	-0.6
$YBa_{2-x}La_xCu_3O_7$	~0.5	35	1.2	0.12	0.4	-1.0	-0.55
$YBa_{2-x}Sr_xCu_3O_7$	~1.5	76	2.0	1.42	1.3	+1.0	-0.6

to detailed changes in the analysis. An increase in the value of μ^* to 0.2 will yield slightly smaller values of λ_M and slightly smaller values of ΔT_c^{OP}, with the same qualitative behavior. The calculation is also relatively insensitive to variations in the frequency of the proposed anharmonic contributions. A higher frequency anharmonicity implies weaker coupling to a phonon spectrum with a more weakly anharmonic mode, yielding the same qualitative behavior of the site selective isotope effect. The primary sources of uncertainty involve assumptions related to the off-plane modes. If the coupling to harmonic off-plane modes is also depressed by the doping, ΔT_c^{OP} for the off-plane isotopic shift will decrease as T_c decreases, while ΔT_c^P will adjust so that the sum of the α's equals the experimental value for uniform isotopic substitution. If the off-plane modes are themselves somewhat anharmonic, then a reduction in this anharmonicity under doping would likely increase ΔT_c^{OP}. In any case, the primary qualitative conclusion is that the off-plane contribution to the isotopic shift in T_c should remain relatively constant under reduction in T_c from Sr or La doping.

In summary, a model of superconductivity involving a dominant anharmonic phonon contribution and a moderate harmonic contribution is consistent with the changes in T_c under site-selective oxygen isotope substitution in $YBa_2Cu_3O_7$. In addition, this treatment yields semiquantitative predictions for the site selective isotope effect in La and Sr doped $YBa_2Cu_3O_7$. In particular, we emphasize that Sr doped $YBa_2Cu_3O_7$ should show a substantial negative isotope effect under planar ^{18}O substitution.

Chapter 5

Anisotropy

A phonon-mediated model of high temperature superconductivity must explain the small values of the electron-phonon coupling derived from an analysis of both high temperature measurements of the resistivity[195] and measurements of infrared conductivity[107]. One possible explanation ascribes the discrepancy to an underestimation of the electron-phonon coupling in the transport measurements due to variations in the Fermi velocity[41]. This work examines an alternative explanation involving the ramifications of anisotropic electron-phonon scattering upon transport estimates of λ.

We examine the effects of anisotropic electron-phonon coupling in systems with Fermi surfaces that contain flat sheets with a view towards applications in the high-T_c superconductors. Such systems can exhibit apparent inconsistencies between transport properties and superconducting properties. Transport experiments do not directly measure the electron-phonon coupling constant λ, which is relevant to superconductivity, but instead λ_{tr}. Specifically,

$$\lambda = \frac{\sum_{\vec{k}\vec{k}'} \frac{|M_{\vec{k}\vec{k}'}|^2}{\hbar\omega_{\vec{k}-\vec{k}'}} \delta(\epsilon_{\vec{k}})\delta(\epsilon_{\vec{k}'})}{\sum_{\vec{k}} \delta(\epsilon_{\vec{k}})}, \tag{5.1}$$

whereas

$$\lambda_{tr} = \frac{\sum_{\vec{k}\vec{k}'} \frac{(v_{\vec{k}x}-v_{\vec{k}'x})^2 |M_{\vec{k}\vec{k}'}|^2}{\hbar\omega_{\vec{k}-\vec{k}'}} \delta(\epsilon_{\vec{k}})\delta(\epsilon_{\vec{k}'})}{2\sum_{\vec{k}} v_{\vec{k}x}^2 \delta(\epsilon_{\vec{k}})}, \tag{5.2}$$

where $M_{\vec{k}\vec{k}'}$ is the electron-phonon matrix element, $\omega_{\vec{k}-\vec{k}'}$ is the phonon frequency, $v_{\vec{k}x}$ is the Fermi velocity and the sum is over the Fermi surface and the phonon branches[108]. Because the transport coupling coefficient is weighed by the difference in Fermi velocities between the different Fermi surface $\vec{k}$ points considered, certain Fermi surface nesting configurations can depress or increase λ_{tr} relative to λ.

For concreteness we will assume that the superconductivity is mediated by buckling modes of O out of the Cu-O bonds. In $La_{2-x}Sr_xCuO_4$, one such mode is an X-point octahedral tilt mode associated with a low temperature tetragonal to orthorhombic transition. This buckling mode could potentially produce a large electron-phonon coupling[51]. Another such mode involves rigid rotations of the Cu-O octahedra about the c axis. Frozen-phonon calculations produce a multiple-well potential for the octahedral tilt mode and a strongly anharmonic single-well potential for the rotational mode[51, 109]. Note, however, that we will not restrict the discussion to any particular class of modes, instead considering a general electron-phonon anisotropy.

LAPW calculations of $La_{2-x}Sr_xCuO_4$ produce a nearly square Fermi surface arising from states in the Cu-O planes[109]. The sides of the squares are oriented along the Γ-X direction, the same direction as the octahedral tilt mode described above. A small-q phonon in this direction will couple electrons all along each parallel face of the Fermi surface, potentially producing a large λ. However, since the Fermi velocities of the modes along a given face are nearly parallel, the contribution to λ_{tr} would be small. In contrast, a phonon mode in this direction with large enough q to couple states on opposite sides of the Fermi surface could produce large contributions to both λ and λ_{tr}.

Unlike $La_{2-x}Sr_xCuO_4$, the other high-temperature superconductors generally have more than one adjacent Cu-O plane, disallowing the possibility of a rigid octahedral tilt mode. However, one can still consider buckling of the O atoms out of the bonds. Potential induced breathing calculations for $YBa_2Cu_3O_7$ suggest unstable phonon branches for motion of oxygens perpendicular to the Cu-O bond[110]. Such results in the potential induced breathing model often signal strongly (and potentially strongly coupled anisotropic) anharmonic modes. For the multi-layer materials we focus on phonon modes with q's parallel to the planar Cu-O bonds. If such phonon modes are associated with a Peierls-type distortion, they would be very anisotropic, with the strong anharmonicity ay be restricted to certain magnitudes of q. LAPW calculations for $YBa_2Cu_3O_7$ produce a

(a)

(b)   (c)
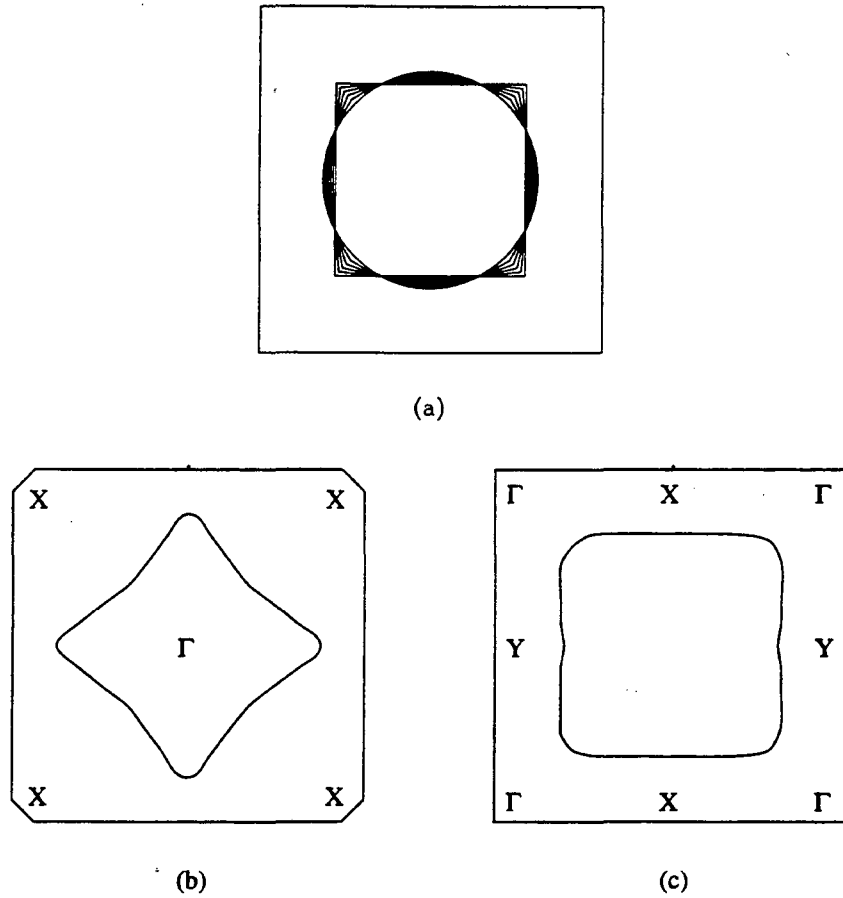
Figure 5.1: Depiction of nearly-square Fermi surfaces. (a) The family of model Fermi surfaces used in the present calculation. (b) Depiction of a portion of the Fermi surface for paramagnetic tetragonal $La_{2-x}M_xCuO_4$ in the $k_z = 0$ plane (M= Sr, Ba). Results shown for x=0.2[109]. (c) Depiction of the Fermi surface of YBa_2CuO_7 calculated using the LAPW method, showing a sheet of the Fermi surface arising primarily from the Cu-O planes[109].

nearly square Fermi surface, rotated by $\frac{\pi}{4}$ from that of $La_{2-x}Sr_xCuO_4$ [51]. The Fermi surface of $Bi_2Sr_2CaCu_2O_8$ also contains roughly square cross sections from the Cu-O and Bi-O planes[111, 112]. Angle resolved photoemission yields Fermi surfaces in good semiquantitative agreement with the LDA results[113, 114, 115]. For these Fermi surfaces the phonon modes considered can nest in a manner similar to that described for $La_{2-x}Sr_xCuO_4$. The coupling of electronic states along flat sheets of the Fermi surface allows the possibility of large superconducting λ and small λ_{tr}.

We now present a simple model calculation to estimate the possible values of λ versus λ_{tr}. In this model, a two-dimensional Fermi surface evolves continuously from a circle to a square. We assume that the phonon modes contributing to T_c involve $\mathbf{q}$'s oriented within a certain opening angle relative to the sides of the square. Contributions from nesting vectors that span the Fermi surface are included, even though these modes should contribute strongly to λ_{tr}. As the Fermi surface shape is varied from circle to square, λ increases while λ_{tr} remains almost constant. The ratio is plotted in Fig. 5.2 for opening angles of 2.3, 5.7, and 11.3 degrees. In this simple model the superconducting electron-phonon coupling can exceed the transport coupling by several times.

Surprisingly, strongly anisotropic electron-phonon coupling within a planar section of a perfectly square Fermi surface will not necessarily produce a gap with a strong signature of anisotropy. Within weak coupling we have the BCS gap equation[1]

$$\Delta_{\mathbf{k}} = -\sum_{\vec{k}'}^{(FS)} V_{\mathbf{k}\vec{k}'} \frac{\Delta_{\vec{k}'}}{2\sqrt{\epsilon_{\vec{k}'}^2 + \Delta_{\vec{k}'}^2}}. \tag{5.3}$$

We model the anisotropy by a sum of delta functions in k space,

$$V_{\mathbf{k}\vec{k}'} = V\left(\delta(k_x - \vec{k}'_x) + \delta(k_y - \vec{k}'_y)\right). \tag{5.4}$$

The choice of k in $\Delta_{\mathbf{k}}$ merely determines the side of the Fermi surface which is summed over; nearly all choices of k yield the same gap equation. The exceptions are the corners of the square Fermi surface, which encompass summations over both adjacent sides, resulting
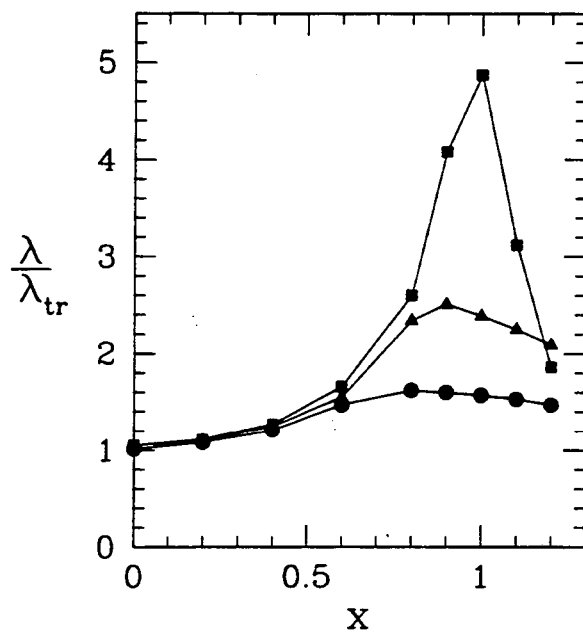
Figure 5.2: Ratio of λ to λ_{tr} for the family of Fermi surfaces shown in Fig. 5.1(a). The parameter x determines the shape of the surface. Taking x=0.0 yields a circle, while x=1.0 produces a square. Values of x above 1.0 produce a square with concave sides. The circles, triangles and squares correspond to opening angles of 11.3, 5.7, and 2.3 degrees respectively.

an a larger gap at these points. On the other hand, in the rather plausible case that the corners are rounded such that the anisotropic interaction only weakly connects the corner states with edges, then the gap will be substantially smaller at the corners of the Fermi surface. These results should also be applicable to strong coupling, since strongly coupled superconductors are expected to exhibit similar, although somewhat weaker gap anisotropies[116],

We note a caveat associated with the assumption of strong electron-phonon coupling along the face of a flat Fermi surface: Migdal's approximation is suspect. For a Fermi surface of arbitrary shape, the second order electron-phonon graph will involve one off-Fermi-surface electron propagator. The contribution from this diagram will be reduced by a factor of the square root of the ratio of ion to electron masses[117]. However, for a flat Fermi surface, the phonon wavevectors can lie in the same plane, so that all propagators are evaluated near the Fermi surface, thereby producing a non-negligible contribution to the total electron-phonon interaction. In this situation, any results for superconducting properties which are based on the Eliashberg equations must be treated with caution.

In summary, we have examined a model of Fermi-nested anisotropic phonons that can account for large differences between superconducting and transport electron-phonon coupling. This model implies that the superconducting gap will be anisotropic, most likely with a smaller gap along directions towards the corners of the Fermi surface.

Chapter 6

Limits on Electronic Mechanisms

A major reason for the proliferation of models involving electronic mechanisms to explain high superconducting transition temperatures are the very small isotope effects observed in the materials with the highest transition temperatures T_c[42, 10, 118, 119]. The apparently felicitous mass-independence of electronic models carries with it a constraint: an electronic mechanism must be consistent with the small *finite* isotope effect in the cuprates. Although at first sight this seems to be a trivial requirement, the isotope shifts are in fact finite albeit small and there are experimental and theoretical estimates that indicate the electron-phonon interaction in these materials is substantial. Thus, any model based on a dominant electronic mechanism for superconductivity must also include the electron-phonon interaction, especially when calculating the isotope shift. The combined electronic and electron-phonon interactions must somehow produce a small isotope effect.

To explore the consequences of this model, the approach taken in Ref. [89] was to solve the Eliashberg equations for combined electronic and phonon-mediated pairing interactions. The electronic mechanism is represented by an attractive interaction at a particular energy, ω_e, with a coupling strength λ_e, while the phonons are represented by an electron-phonon coupling function with a total coupling λ_{ph}. Within the approximation of the McMillan formula for T_c, it was shown that

$$\alpha = \frac{\lambda_{ph}}{2\lambda},\tag{6.1}$$

where $\lambda = \lambda_{ph} + \lambda_e$. As expected, α is reduced by the presence of an electronic mechanism.

To determine whether it is possible to produce the observed values of T_c and α for

reasonable values of λ_{ph}, the Eliashberg equations were solved for specified T_c and α (taken to be 93 K and 0.02 respectively for $YBa_2Cu_3O_7$) by choosing an appropriate phonon spectrum consisting of Lorentzian peaks. For a given energy of the electronic mode, ω_e, the strength of this mode relative to that of the phonon modes as well as λ were varied until correct values of T_c and α were obtained. It was found that the λ_{ph} obtained from these calculations increased as ω_e decreased. However, even for very small values of ω_e down to 30 meV, the resultant values for λ_{ph} were considerably smaller than theoretical and experimental estimates, which range upwards from $\lambda_{ph} = 0.3$. For still smaller values of ω_e, λ becomes unphysically large; $\lambda >> 10$, values which virtually guarantee a structural phase to a structure with smaller λ. It was concluded that low values of ω_e are necessary for this model because they produce the largest values of λ_{ph}, but that the predicted value of λ_{ph} is still less than half of the smallest estimates of that quantity. The present work will show that an electronic mechanism with an inverse isotope effect is capable of resolving this difficulty. As discussed in Ref. [89], it is possible that the Eliashberg model is not adequate to describe the high T_c materials because of low-dimensionality effects, a possible non-Fermi liquid ground state, or a failure to describe the electronic mechanism by the model assumed there. However, it has generally been assumed that many of the central features of superconductivity can be adequately described by the Eliashberg equations and even if this is not the case, it is still instructive to examine the consequences of the conventional theory.

Anharmonic phonons can produce values of T_c and α in agreement with experiment for the high-T_c oxides,[102] and there has been some experimental evidence for the existence of anharmonic modes. A model with large electron-phonon coupling for the anharmonic modes is capable of explaining the values of $\alpha > \frac{1}{2}$ and the dependence of α on doping in La-Sr-Cu-O[102, 43, 22, 97]. Anharmonic phonons can also explain site selective isotope experiments[98]. Here, we take a different point of view and consider a nonphonon mechanism (e.g. electronic) that couples to the lattice so as to produce a positive isotope shift,

(i.e. $\alpha_e < 0$, as opposed to $\alpha_e = 0$ for a purely electronic mechanism or $\alpha_{ph} = 0.5$ for harmonic phonons). This mechanism is modeled an energy ω_e and a coupling strength λ_e relative to the phonon modes, a coupling which is determined by T_c and α. We define a mass dependence to ω_e and λ_e by introducing the definitions

$$\lambda_{e,M} = -\frac{M}{\lambda_e}\frac{d\lambda_e}{dM} \tag{6.2}$$

and

$$\omega_{e,M} = -\frac{M}{\omega_e}\frac{d\omega_e}{dM}. \tag{6.3}$$

Unlike previous models, we also assign a positive isotope shift to the mode by considering negative values of $\omega_{e,M}$ or $\lambda_{e,M}$, either or which will yield an electronic contribution to the isotope effect $\alpha_e < 0$.

Experimental motivation for consideration of such an inverse isotope effect is provided by site-selective oxygen isotope effect experiments[95] A careful choice of exchange conditions allows selective diffusion of plane oxygen sites by exploitation of the different microscopic diffusion rates. An extrapolation of site-selective isotope effect results to perfect site selection implies an *increase* in T_c of 0.32 K for ^{18}O substitution with off-plane oxygen remaining ^{16}O, suggesting the presence of some variety of inverse isotope effect.

To illustrate the changes expected for $\alpha_e \neq 0$, a calculation similar to that which gave Eqn. 6.1 and allowing for a mass-dependent λ_e yields

$$\frac{\lambda_{ph}}{\lambda} = \frac{\alpha - \omega_{e,M} - \frac{\lambda_{e,M}}{\lambda}}{\frac{1}{2} - \omega_{e,M}}. \tag{6.4}$$

where $\lambda = \lambda_e + \lambda_{ph}$. Here we assume harmonic phonons so that $\lambda_M^{ph} = 0$ and $\alpha_{ph} = 1/2$. Because $\alpha = 0.02$ is very small, even modest negative values of $\omega_{e,M}$ and $\lambda_{e,M}$ can increase λ_{ph}/λ substantially, as required to obtain agreement with the estimated values of λ_{ph}. To illustrate this result we consider the case of $\omega_{e,M} < 0$ and $\lambda_{e,M} = 0$. For the purposes of calculating α, a mass-dependent λ_e can be formally incorporated into an effective mass-dependent ω_e which yields the same shift in T_c under isotopic shift of just the electronic
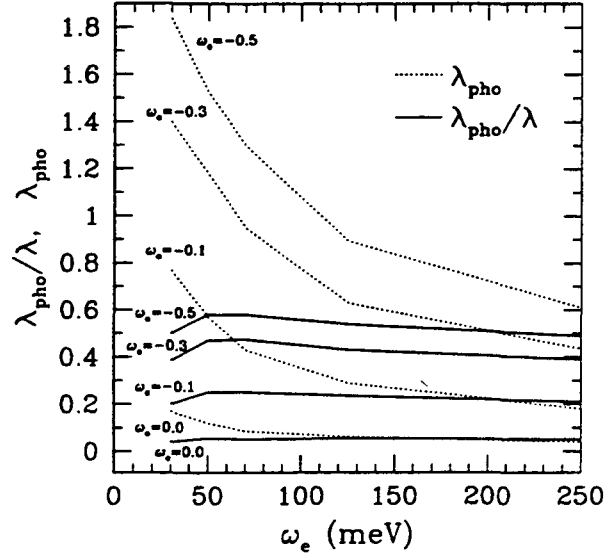
Figure 6.1: Values of the electron-phonon coupling strength, λ_{ph} (dashed), and the ratio of the electron-phonon coupling to the total coupling, λ_{ph}/λ (solid), versus the energy of the electronic mode for various values of the electronic isotope shift, $\omega_{e,M}$=0.0, -0.1, -0.3, and -0.5. The curves are determined by the constraints T_c=93 K and $\alpha = 0.02$.

mode. We choose to examine just $\omega_{e,M} \neq 0$ since in this case we have the simple relation $\omega_{e,M} = \alpha_e$, expressions which will be used interchangeably in the rest of this chapter.

For detailed numerical calculations the phonon spectrum was again modeled by Lorentzian peaks and the Eliashberg equations were solved numerically. The electronic contribution has a strength which depends on its energy ω_e and which is determined by the values T_c=93 K and $\alpha = 0.02$, where $\mu^* = 0.12$ is assumed. Results of the numerical calculations for $\omega_{e,M} = 0.0$, -0.1, -0.3 and -0.5 are shown in Figs. 6.1 and 6.2. In all cases, λ_{ph}/λ is relatively independent of ω_e as predicted by Eqn. 6.4. Eqn. 6.4 is accurate to $\sim$25%, even though it was derived for $\mu^* = 0.0$ and $\lambda < 1.5$. The value of λ_{ph} is seen to increase rapidly with increasing $|\omega_{e,M}|$ for a given value of ω_e. The shape of the curves
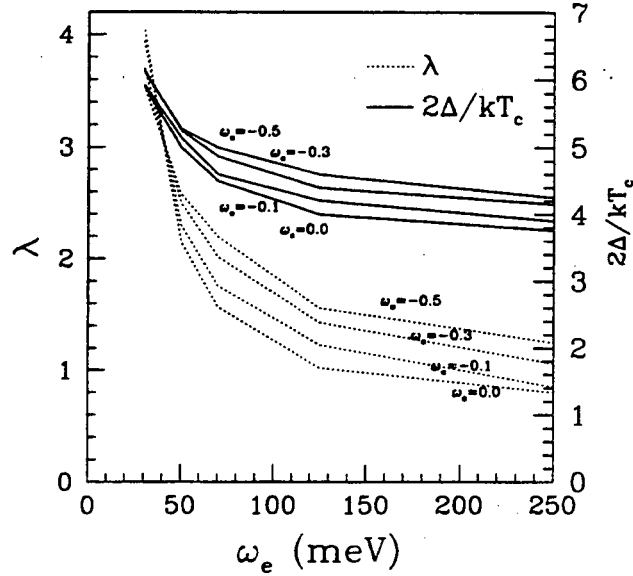
Figure 6.2: Values of the total coupling, $\lambda = \lambda_{ph} + \lambda_e$ (dashed), and $2\Delta/kT_c$ (solid) versus the energy of the electronic mode for various values of the electronic isotope shift, $\omega_{e,M}$=0.0, -0.1, -0.3, and -0.5. The curves are constrained by the conditions T_c=93 K and $\alpha = 0.02$.

describing λ_{ph} in Fig. 6.1 are also described well by Eqn. 6.4 since $\lambda_{ph} \propto \lambda$. The total coupling strength λ must increase with decreasing ω_e as shown in Fig. 6.2 to maintain a constant T_c; hence λ_{ph} also increases for decreasing ω_e according to Eqn. 6.4 as shown in Fig. 6.1. The lower bound on the range of estimates for λ_{ph} in YBa$_2$Cu$_3$O$_7$ is roughly 0.3. As shown in Fig. 6.1, the addition of a small negative $\omega_{e,M}$ yields λ_{ph} above this value for a wide range of electronic mode frequencies. A value of $|\omega_{e,M}|$ as small as 0.02 yields $\lambda_{ph} \sim 0.3$ for an electronic mode at $\omega_e = 30$meV.

The total coupling strength λ and the gap ratio $2\Delta/kT_c$ increase with decreasing ω_e as shown in Fig. 6.2, with λ becoming very large for $\omega_e < 30$ meV. The gap ratio is a weakly increasing function of $|\omega_{e,M}|$. Experimental values for the gap ratio up to $2\Delta/kT_c \sim 8$

have been reported and the current calculations yield $2\Delta/kT_c \sim 6$ for $\omega_e \sim 30$ meV. A careful study of Raman phonon frequency shifts at T_c suggests $2\Delta/kT_c \sim 5$,[120] which is consistent with an electronic mode in the frequency range 40-90 meV. These relatively low frequencies are also most conducive to large values of λ_{ph}, suggesting that this frequency range is most plausible for an electronic model of high T_c.

The preceding analysis assumes that $\alpha^2 F(\omega)$ is entirely due to oxygen-atom phonons. A significant portion of the coupling, particularly in the lower frequency range, could arise from non-oxygen vibrations. This situation has been modeled by using the same form for $\alpha^2 F(\omega)$, but assuming the the modes below 26 meV do not shift upon isotopic substitution. Since a portion of λ_{ph} is mass-independent, this treatment yields values of λ_{ph} roughly 10% larger than those previously obtained.

The site-selective isotope effect experiments provide an additional constraint on the model. These measurements are accounted for within the present model by assuming that the mass dependence of the electronic mechanism depends exclusively on the mass of the in-plane oxygen atoms. The site selective material is modeled by a spectral function in which the electronic contribution is isotopically shifted along with the planar portion of the phonon-mediated contribution. The phonon contribution to $\alpha^2 F(\omega)$ is apportioned between planar oxygen and off-plane oxygen contributions by dividing each of the Lorentzians above 25 meV into two separate peaks, one attributed to planar oxygen phonons and the other off-plane oxygen phonons. The relative strength of these two contributions is varied to obtain agreement with the site-selective isotope effect results. Since the total phonon contribution has not been modified, agreement with the full isotope effect is not affected. For $\omega_{e,M}=-0.3$ or -0.5, the model is consistent with the site selective results if $\sim$75% of the oxygen phonon contribution to λ_{ph} arises from planar oxygens. A value of $\omega_{e,M} = -0.1$ implies that $\sim$50% of the oxygen phonon contribution to the electron-phonon coupling arises from in-plane modes. Smaller values of $|\omega_{e,M}|$ require that a larger fraction of the electron-phonon coupling arise from non-planar phonons.

With a view towards the evaluation of possible physical mechanisms for a negative $\omega_{e,M}$, we determine the minimal possible values of $|\omega_{e,M}|$ which are consistent with the site selective isotope effect and the constraint $\lambda_{ph} > 0.3$. For these calculations μ^* is allowed to vary between 0.1 and 0.2 and the modes in $\alpha^2 F$ below 25 meV are assumed to be non-oxygen. These conditions weaken the experimental constraints on $\omega_{e,M}$ so as to yield a more rigorous lower bound. For electronic mode frequencies below $\sim$100 meV, the primary constraint is the site selective isotope effect, which requires that $|\omega_{e,M}| > 0.05$. Values of $|\omega_{e,M}|$ less than 0.05 imply that less than $\sim$15% of the oxygen contribution to λ_{ph} arises from in-plane modes, a physically implausible situation. (Without the constraint from the site-selective isotope effect, the lower bound on $|\omega_{e,M}|$ for a low-frequency electronic mode is reduced to roughly $|\omega_{e,M}| > 0.02$.) For electronic frequencies above $\sim$100 meV, the primary constraint is the requirement that $\lambda_{ph} > 0.3$. This condition is fulfilled for $|\omega_{e,M}| > 0.1$.

It is instructive to examine the way in which our calculations place restrictions on a particular model for an inverse electronic isotope shift. If it is assumed that the shift in T_c is due solely to the fractional change in lattice spacing, $\frac{\delta a}{a}$, under $^{18}O \rightarrow ^{16}O$ substitution, then the shift in T_c can be estimated from the pressure dependence of T_c[121]. (The variation in T_c with pressure would also involve changes in the phonon spectrum. However, the present model implies that the electronic contribution dominates the superconductivity, suggesting that the increase in T_c under pressure can plausibly be ascribed to changes in an electronic mechanism.) The isotopic shift due to the change in lattice constant can be estimated from the isothermal compressibility and the Gruneisen constants as was done for Ge[122] and the value $\frac{\delta a}{a} \sim 1 \times 10^{-4}$ at T=0 is obtained. This yields $\omega_{e,M} \sim -0.005$, roughly a factor of ten smaller then the minimal value required by our calculations. Obviously there are other models possible for an inverse electronic isotope effect which will require a similar analysis. In particular, there may be interesting classes of electronic mechanisms in which $\lambda_M^e \neq 0$.

Approaching the problem of a negative electronically based isotope effect from the theoretical side, the volume dependence of T_c within an electronic mechanism may arise from variations in the electron hopping amplitude. The transition temperature is generally an increasing function of the hopping amplitude, which tends to increase under lattice compression. However, the decrease in lattice constant due to isotopic substitution is accompanied by a decrease in thermal ionic motion. Since the hopping rate is an increasing function of the inverse distance, thermal motion should increase the hopping rate at a given lattice constant. A semiclassical model of this behavior assumes a hopping rate proportional to L^{-n}, where L is the interatomic spacing and n~2 or 3. The hopping rate, t, averaged over one period of motion, is

$$t \propto \frac{1}{2\pi} \int_0^{2\pi} \left(\frac{1}{L + A \sin t} \right)^n dt, \tag{6.5}$$

where A is the vibrational amplitude. An increase in isotopic mass will decrease both the interatomic spacing $L \to L - \delta L$ and the vibrational amplitude $A \to A - \delta A$. In general, we expect $\frac{\delta A}{A} >> \frac{\delta L}{L}$ and $\frac{A}{L} << 1$. In the case n=2, straightforward algebra yields

$$\frac{\delta t}{t} = -2\frac{\delta L}{L} + 3\frac{\delta A}{A}\left(\frac{A}{L}\right)^2. \tag{6.6}$$

The effect of the decrease in vibrational amplitude on the hopping rate is reduced by a factor of $\left(\frac{A}{L}\right)^2$ relative to the effect of the decrease in interatomic spacing. The qualitative features of this model should carry over into a quantum formulation, since the effects of δA and δD on the hopping rate should remain linear, and the effect of δA should be reduced due to the oscillatory nature of the motion. The relevant scale for such a reduction is $\frac{A}{D}$, and this ratio must be squared, since the sign of the amplitude is irrelevant. Applying this model to YBa$_2$Cu$_3$O$_7$, we estimate $\frac{\delta A}{A} \approx \left(\frac{M_{18_O}}{M_{16_O}}\right)^{\frac{1}{4}} - 1$, and $\frac{\delta L}{L} \approx 2 \times 10^{-4}$ as before. The ratio $\frac{A}{D}$ is estimated as $\sim \frac{0.14\overset{\circ}{A}}{2.0A} \sim 0.02$. We obtain as increase in the hopping rate of $\frac{\delta t}{t} \approx 2 \times 10^{-4}$ for either n=2 or n=3. Neglecting the change in vibrational amplitude yields $\frac{\delta t}{t} \approx 4 \times 10^{-4}$ for n=2 and $\frac{\delta t}{t} \approx 6 \times 10^{-4}$ for n=3, indicating that the change in vibrational amplitude

can reduce the hopping rate significantly, counteracting the effects of the decrease in lattice constant. Taking $T_c \propto t^2$, (as suggested by RVB and some polaronic models) yields $\alpha_e \sim -0.002$, well below that required to reconcile a predominantly electronic mechanism with the experimental and theoretical constraints on λ_{ph}. Of course superconductivity within an RVB model will not be amenable to an Eliashberg-based analysis. However, the present results suggest that the possible RVB-based contributions to the isotope effect are not consistent with the experimentally measured isotope effect and electron-phonon coupling.

In summary, we have shown that an electronic mechanism for superconductivity in $YBa_2Cu_3O_7$ is consistent with values of T_c=93 K and $\alpha = 0.02$ as well as estimates of λ_{ph} if the electronic mechanism couples to the lattice in such a way as to produce an inverse isotope effect. Electronic models for high temperature superconductivity should be evaluated in terms of their ability to produce a significant inverse isotope shift.

Chapter 7

Microscopic Mechanisms

The values of the electron-phonon coupling necessary to produce $T_c \approx 90$ K for an average phonon frequency of $\approx 600K$ on of the order $\lambda \approx 2 - 3$, comparable to the values obtained in Pb and Pb-Bi alloys. However, in these systems, the large values of λ arise predominantly from the low phonon spring constants, as evidenced by the relation

$$\lambda = \frac{N(0)\langle I^2 \rangle}{M\omega^2}, \tag{7.1}$$

where N(0) is the density of states at the Fermi surface, $\langle I^2 \rangle$ is an average electron-phonon matrix element, M is the ionic mass, and $\langle \omega \rangle$ is an average phonon frequency. The maximum T_c obtainable by the strategy of reducing the denominator in Eqn. 7.1 is limited because such a reduction of necessity also reduces the average phonon frequency. Substantial increases in T_c must arise from the numerator, the detailed structure of the electron-phonon matrix elements.

One possible source of a large $\langle I^2 \rangle$ is a dynamic Peierls-type distortion[123], in which a lattice distortion which increases the unit cell size dynamically gaps a suitably shaped Fermi surface, producing strong electron phonon coupling for phonon modes of potentially relatively high frequency. Although Peierls distortions are generally associated with 1 dimensional systems, they can occur in any system in which the locus of k points satisfying $k \cdot G = \pi/2$ where G is a reciprocal lattice vector, coincides with the Fermi surface.

The high T_c oxides generically possess nearly square quasi-two dimensional Fermi surfaces associated with the Cu-O planes. In addition, the nesting vector between opposite sides of the Fermi surface generally closely corresponds to a simple rational fraction of a dimension of the Brillouin zone, namely $\frac{2}{3}$ for $YBa_2Cu_3O_7$ and $\frac{1}{2}$ for $La_{2-x}Sr_xCuO_4$. de

Haas-van Alphen[124] and photoemission[113, 114, 115] measurements corroborate the detailed features of the theoretically determined Fermi surface, giving one confidence that the actual Fermi surface has the properties necessary to encourage Peierls distortions. These features suggest that certain large q static distortions could gap the Fermi level in these materials, implying that corresponding dynamic distortions would yield large electron-phonon coupling. These distortions come in two flavors: those along a Cu-O bond would couple to electrons in first order while those perpendicular to the bonds would couple in second order. The second order contributions could be substantial for a strongly coupled system with $\lambda \sim 2 - 3$. Both forms of distortion produce anisotropic electron-phonon coupling of the sort necessary to yield both an anisotropic gap and a strongly temperature-dependent Hall coefficient[125]. In addition, distortions perpendicular to the bond are particularly appealing in that such a second order coupling corresponds to strong coupling between electronic states along the same side of the Fermi surface, a condition which suppresses the transport-relevant form of the electron phonon coupling as discussed in Chapter 5. Finally, these distortions, in which the system dynamically enters an alternative structure at a local minimum in the total energy, would be described by multiple-well potentials, a form of anharmonicity which would suppress the isotope exponent α.

Indirect evidence for Peierls-like behavior can be found in the sensitivity of the superconductivity to the degree of order in the Cu-O plane. The Peierls-like modes require the underlying lattice to possess medium to long-range order. The high temperature tetragonal (and low temperature tetragonal) phases of $La_{2-x}Sr_xCuO_4$ are disordered arrangements of tilted Cu-O octahedra that average to the structure observed in X-ray scattering experiments. This profound disorder should preclude Peierls-type behavior, as is observed in well-annealed samples of $La_{2-x}Sr_xCuO_4$ [118]. We note that a Nd-doped $La_{2-x}Sr_xCuO_4$oxide exhibits superconductivity in the low temperature tetragonal (LTT) phase. [43] However, in this case it is unclear if the LTT phase is disordered or ordered.

Thermal expansion measurements suggest the presence of a lattice instability which

appears to be occur at the maximum T_c associated with both single layer and double layer compounds[35]. This instability can be interpreted as a change in the symmetry of the Cu-O planes sufficient to suppress the superconductivity. The instability need not be mediated via the actual mechanism of superconductivity; any distortion which weakens the nesting conditions would suffice. Of course such behavior is not unique to a dynamic Peierls model, but applies to any mechanism sensitively dependent on the detailed structure of the Cu-O planes.

Direct evidence of potentially dynamic buckling distortions can be found in various local probes of the lattice dynamics (we note that q=0 optical probes will not be sensitive to the large-q Peierls modes). EXAFS studies of apical oxygen motion can be fit with a double-well potential. The EXAFS results can also be interpreted in terms of planar distortions, which would also be of multiple well character. As mentioned in Chapter 3, neutron scattering pair distribution function measurements in $La_{2-x}Sr_xCuO_4$ [46], $Nd_{2-x}Ce_xCuO_4$[126], $YBa_2Cu_3O_7$ [127] and $Tl_2Ba_2CaCu_2O_8$[128] can be fit to models with structural distortions of the Cu-O planes involving superpositions of planar buckling structures or apical oxygen displacements with hints that these distortions are dynamic. Ion channelling measurements can also be interpreted in terms of structural distortions near T_c on the oxygen sublattice[129]. A Peierls-like mechanism would of necessity involve incipient lattice distortions similar to those described. As a caveat, we note that although clearly there are anomalous lattice dynamics associated with the superconducting transition, available evidence does not indicate whether these distortions are intimately associated with the cause of high T_c or rather simply a side effect of an alternative mechanism.

In the simplest approximation, the potential for a Peierls-like distortion would take the form

$$V(x) = -A|x| + Bx^2, \tag{7.2}$$

where the linear term models the decrease in energy upon gapping the Fermi surface, with the coefficient A a monotonically increasing function of the coupling strength λ. The anharmonicity of the potential as measured by the magnitude of λ_M will also be a monotonically increasing function of A, analogous to the situation with the potentials in Fig. 3.8. The doping dependence of T_c would arise from the necessity of matching the Fermi surface size to a commensurate wavevector. Unfortunately, in a realistic system both the readjustment of the other electronic bands and the effects of zero point motion may change the form of the potential sufficiently such that Eqn. 7.2 is no longer accurate. The qualitative feature of multiple wells is likely to survive in a form related to that considered in Chapter 3.

This speculative discussion presents one idea for the genesis of multiple vibrational potentials in a strongly coupled system. The model makes use of several of the special electronic features of the copper oxide superconductors, namely the two-dimensionality and the strong Fermi surface nesting at commensurate wavevectors. The model predicts either secondary maxima or plateaus in the superconducting transition temperature at other doping levels which yield less favorable, but still commensurate nesting wavevectors.

Chapter 8

Introduction to C_{60} Systems

An important first step towards understanding the solid state physics of a new material is an understanding of the electronic structure. The theoretical results for the electronic structure of pristine and doped fullerenes rely primarily upon one electron theory and LDA band structure, with a few theoretical quasiparticle band structure results. These approximations appear to be plausible although several researchers have questioned the applicability of theories of this kind in view of the possible importance of electron correlation in these relatively narrow-band systems. Experimental results generally support the one-electron picture. A solid grounding in electronic structure facilitates the later discussion of phonon dynamics, electron-phonon coupling, transport and superconducting properties of alkali doped fullerenes[130]. The necessary background on superconductivity is repeated in abbreviated form so that the fullerene section of this work may be read independently of the earlier chapters.

8.1   Electronic Structure

The electronic structure of an isolated C_{60} molecule provides a convenient starting point. The bonding character of C_{60} is predominantly sp^2 with a small admixture of sp^3 character due to the non-zero curvature. For this reason, the electronic states can be decomposed into approximate π and σ states. The bonding σ states reside well below the highest occupied level, which is composed of orbitals having primarily π character[131, 132]. The nearly spherical structure of the C_{60} suggests a labelling of these electronic states in terms of spherical harmonics, with the σ and π electrons corresponding to different radial quantum numbers. The carbon-derived potential splits the degenerate energy levels of the

spherical potential, producing the level structure shown in Fig. 8.1. The non-spherical part of the potential is dominated by an $\ell = 10$ contribution, which splits electronic levels having $\ell \geq 5$ [133].

Fifty π electrons fill orbitals from $\ell = 0$ to $\ell = 4$, and ten electrons occupy part of the $\ell = 5$ shell. The carbon potential splits the eleven (ignoring spin) degenerate states of this $\ell = 5$ level into a five-fold degenerate highest occupied molecular orbital (HOMO) of h_u symmetry, a three-fold degenerate lowest unoccupied molecular orbital (LUMO) of t_{1u} symmetry, and an additional three-fold degenerate level at slightly higher energy. The ten $\ell = 5$ electrons fill the five-fold level, yielding a closed-shell configuration.

C_{60} forms a Van der Waals solid wherein the fairly weak overlap between molecular levels yields relatively narrow bands. Doping with alkali atoms yields an ionically bound solid still with relatively weak dispersion. Electronic band theory provides a consistent explanation of semiconducting fcc C_{60} [133, 134], doped metallic systems such as K_3C_{60} [135, 136] and semiconducting K_6C_{60} [137]. We focus on fcc C_{60} and K_3C_{60} as prototype materials for examining normal-state and superconducting properties.

Although there are still some open questions related to the effects of electron-electron correlation energy for these materials,[138] it has been argued [133, 134] that one-electron band theory yields consistent results for C_{60} and K_3C_{60} with band widths ~ 0.5eV. The outstanding difficulty of one electron theory appears to be the nonmetallic nature of K_4C_{60}, which according to band theory should be a metal. Putting this unusual material aside for the purposes of this discussion, we describe the prototype systems C_{60} and K_3C_{60} using standard band theory.

Solid fcc C_{60} is bound by van der Waals attraction between the clusters with a nearest-neighbor separation of 10 Å. This relatively large separation compared to the C-C separations within the clusters (~ 1.45 Å) results in flat bands formed from the predominantly sp^2 states. As in the isolated molecule, the resulting band states near the band gap have π character. If a spherical harmonics decomposition is used for the wavefunctions as in the

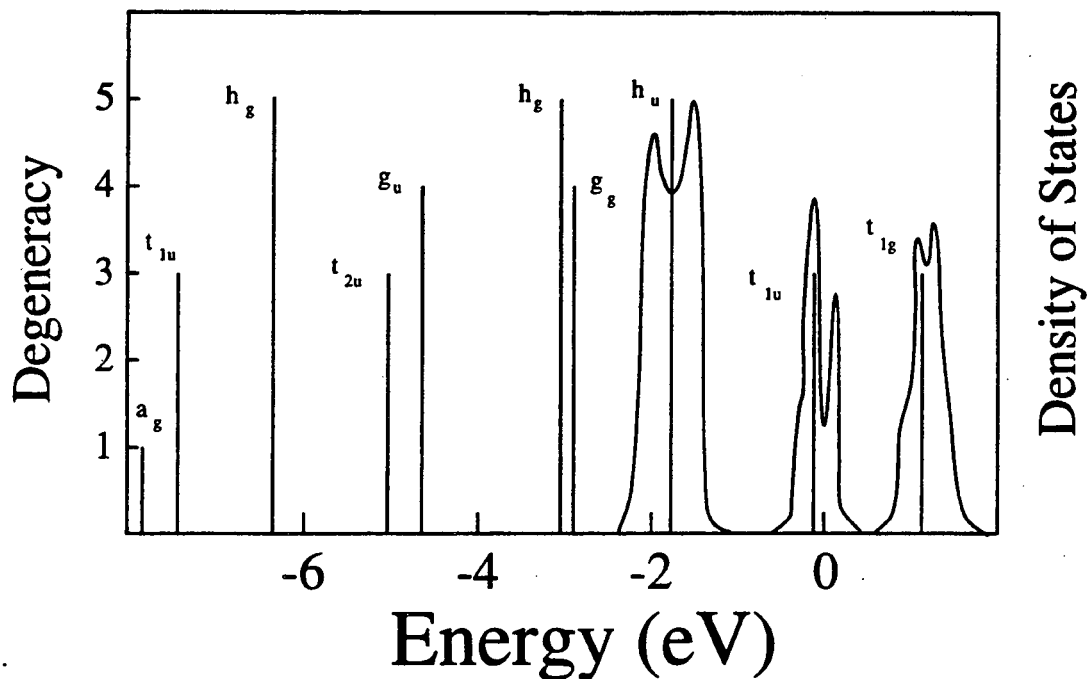Figure 8.1: Electronic energy levels of π states in an isolated C$_{60}$ molecule.[131, 132, 133] The highest σ states, which have been omitted for clarity, lie at roughly -4 eV. The density of states of the bands in K$_3$C$_{60}$ which correspond to the h$_u$, t$_{1u}$ and t$_{1g}$ states of the molecule has been superimposed.[134, 135, 143, 144, 145, 146] The Fermi level of the solid is set at 0 eV.

molecular system, then the states near the band gap have angular momentum character of $\ell = 4$ and 5.

Band structure calculations by Saito and Oshiyima (SO)[135] and by Martins and Troullier (MT)[136] give similar results and differ only in the finer details. Both calculations employ pseudopotentials and the local density approximation (LDA). SO employ a gaussian-orbital basis which is considerably smaller than the plane wave basis set used by MT, which has as many as ~30,000 plane waves. Both the SO and MT calculations include total energy estimates of lattice constants, bulk moduli, and cohesive energies. It is encouraging that the results of these calculations are similar considering the differences in the wavefunction expansion.

Some general features of the band structure can be discussed in terms of the relation of the bands to molecular orbitals. Since there are 240 electrons per primitive cell, one expects 120 (90 σ and 30 π) filled bands. The 90 filled σ-bands are well below the Fermi energy. The top five bands are derived from the h_u five-fold degenerate HOMO of C_{60}. The lowest three valence bands are related to the t_{1u} LUMO. The remaining three of the 11 $\ell = 5$ states are contained in an upper unoccupied t_{1g} state. Both the valence band maximum and conduction band minimum lie at the X-point of the Brillouin zone, with a gap separation of ~ 1.5 eV. The relative orientations of the C_{60} clusters can affect the band structure. Here the highest symmetry configuration, T_h, is assumed for the fcc lattice of rigid molecules. The rotation of the molecules above ~260K[139] alters the band structure and broadens the bands.

Because the states near the band gap originate from states of u-symmetry, optical transitions between the top of the valence band and the bottom of the conduction band are forbidden in lowest order. Although the LDA calculations are best suited for ground state properties, photoemission [140] and inverse photoemission[141] data are in reasonably good agreement with the predictions of the pseudopotential-LDA calculations.

When alkali atoms are placed in the two interstitial tetrahedral sites and the octahedral

site, a rigid-band model would predict that the t_{1u} derived bands are half full, implying that K_3C_{60} should be metallic. In the gas phase, the C_{60} molecule can accommodate two electrons and form a stable C_{60}^{-2} ion. [142] In the solid phase, analysis of K_3C_{60} and K_6C_{60} suggest that the potassium 4s electron is transferred to the C_{60} molecule, resulting in a strongly bonded ionic metal for K_3C_{60} and a semiconductor with a band gap of ~ 1 eV [137] for K_6C_{60}. Hence, the charge state of C_{60} is strongly influenced by its local environment. The Madelung energy of the crystal, electron affinity of the C_{60}, and ionization energy of the alkali are major factors in the bonding and charge states.

Although evidence for the inadequacy of a strict rigid band model exists [140], the concept of alkali metal doping appears to be representative of the situation for K_3C_{60}. Electrons are transferred and the weakly bonded van der Waals crystal transforms into a more strongly bound ionic metal. The Fermi level crosses the lowest two t_{1u} bands with the electrons occupying almost all of the lowest band and more than half of the second of the three bands. The Fermi level lies on a steep downward slope in the density of states, as indicated in Fig. 8.1, so that the density of states is a sensitive function of the lattice constant. For these reasons, theoretical results for the density of states at the Fermi level, $N(E_F)$ vary from 10 to 30 states per eV per C_{60}. Because of the band dispersion between Γ and X, hole-like Fermi surfaces exist at Γ for both the first and second conduction bands. The first band also contains hole surfaces near the L point of the Brillouin zone. For the next highest band there are both hole and electron surfaces, yielding a Fermi surface with at least two hole-like and two electron-like branches[143, 144, 145, 146, 147, 148].

In contrast to the undoped material, K_3C_{60} exhibits low-temperature orientational disorder, with equal population of two orientations related by a $\frac{\pi}{2}$ rotation[149]. This disorder will smear out peaks in the density of states[150] and contribute to a large residual resistivity[151]. Electronic structure results based on a perfect crystal should be used with caution in light of this microscopic orientational disorder.

8.2 Phonons

The phonons of C_{60}-based solids can be conveniently divided into low frequency interball and high frequency intraball modes. The interball phonons are further divided into librational, vibrational, and alkali-atom modes. Each of these modes could plausibly contribute to some degree to the electron-phonon coupling necessary for the BCS theory of superconductivity. The mechanisms of electron-phonon coupling will be described later; here we consider the various phonon modes and give a qualitative discussion of the possibilities for electron-phonon coupling for each class of modes.

The lowest-energy phonons of doped C_{60} are the rotational motions of the C_{60} molecules. In contrast to pristine C_{60}, the doped material does not exhibit quasi-free molecular rotation[152]. Instead, the C_{60} molecules of the doped materials undergo small-amplitude librational motions. These librational modes have very low frequencies – on the order of 20 or 30 K [153], as expected due to the large oscillator mass, near-spherical nature of C_{60} and the rather weak van der Waals binding between the C_{60} molecules. Since the band dispersion of solid C_{60} is determined by the electronic overlap between molecules, which in turn is sensitive to the relative orientation of adjacent molecules, the librational modes could potentially exhibit significant electron-phonon coupling. However, the low frequency of these modes suggests that they will not make substantial contributions to the superconducting transition temperature.

The fullerene systems also possess low-frequency modes of translational character. These are expected to have somewhat higher frequencies than the librational modes, since bulk translational motions should induce greater interaction between the molecules than rotations. A rough estimate of their frequencies based on the bulk modulus of the material[154] yields $\omega \sim 60$ K. Inelastic neutron scattering[155] and Raman scattering[156] reveal broad peaks near 50 K and 150 K which have been identified with these modes. Low to moderate $\vec{q}$ translational modes induce local changes in the lattice constant, which

induces local changes in the bandwidth. A tight-binding picture of interball interaction yields small to moderate electron-phonon coupling for these distortions[157, 158].

The alkali atoms reside in the tetrahedral and octahedral interstitial sites of the fcc C_{60} lattice. Electron energy loss spectroscopy [159] suggests that the vibrational modes of the alkalis in these sites have frequencies around 100-200 K. Local density calculations indicate that the sites are effectively "holes" in the C_{60} lattice, with little charge density other than that residing immediately atop the alkali atom. This result allows the possibility that the alkali atoms reside in strongly anharmonic potentials with a significant quartic component and perhaps a weak multiple-well character, results that could have implications for a possible alkali atom superconducting isotope effect. The large electron affinity of the C_{60} molecule guarantees that the alkali atoms will be almost completely ionized. The positively charged ions will polarize the electrons on adjacent C_{60} molecules, thereby coupling the alkali motions to the electronic system. An estimate of the potential electron-phonon coupling due to a static displacement of the alkali atoms suggests extremely strong coupling[160]. However, a model of superconductivity based entirely on the alkali atom vibrations encounters significant difficulties in explaining the large carbon isotope effect, as will be discussed in more detail later.

The high-frequency intraball phonons subdivide into two ill-defined classes, the lower-frequency radial modes and the higher-frequency tangential modes. The tangential modes involve stretching and compression of the carbon-carbon bonds, as opposed to the primarily radial motions of the carbon atoms for the lower-frequency modes. The situation is analogous to that in graphite, in which the modes with in-plane displacements have higher frequencies than those involving buckling motions out of the graphitic sheets. The curvature of C_{60} produces hybridization between the radial p_z orbitals and the s orbitals which allows new scattering channels for the electron-phonon coupling which are absent in planar graphite. [161, 162] In contrast to doped C_{60}, alkali-intercalated graphite systems have superconducting transition temperatures $\sim$1 K [163].

Table 8.1: Experimental phonon frequencies[162] for intraball modes in *undoped* C_{60} of the correct symmetry to mediate electron-phonon coupling. Upon doping, the energies shift by a few percent.

Mode	$\omega(K)$
$H_g(1)$	393
$H_g(2)$	629
$H_g(3)$	1022
$H_g(4)$	1071
$H_g(5)$	1581
$H_g(6)$	1799
$H_g(7)$	2055
$H_g(8)$	2266
$A_g(1)$	715
$A_g(2)$	2114

We concentrate on the C_{60} intraball phonon modes of A_g and H_g symmetry, since group theory implies that only these modes will couple with the t_{1u} symmetry electronic states at the Fermi level. The relevant phonons are enumerated in Table 8.1 [164]. The lower-frequency A_g mode corresponds to a breathing motion, whereas the higher frequency mode involves out-of-phase oscillations of the single and double bonds. The lowest frequency H_g mode produces a radial distortion of the C_{60} molecule into an ellipsoid, whereas the higher frequency H_g modes possess progressively more tangential character[165], as anticipated.

By fortune, the selection rules for electron-phonon coupling and Raman scattering are the same, so that these same ten modes are also Raman active. Electron-phonon coupling will cause decay of phonons into electron-hole pairs, yielding a finite phonon lifetime, which may be evidenced by the non-zero widths of the Raman peaks. [166] In theory, $\vec{q} = 0$ Raman-active modes will not couple to the electrons because of phase space factors; however, the strong orientational disorder in the doped system will allow wavevector-nonconserving processes. A study of the broadening of the Raman lines upon doping indicates a significant coupling to the $H_g(2)$ mode at 560 K, and moderate coupling to the higher frequency $H_g(7)$ and $H_g(8)$ modes[167, 168] Inelastic neutron scattering[155] also indicates substantial broadening of several of the H_g modes. If this broadening is interpreted in terms of electron-phonon coupling, then a reasonably consistent argument for electron-phonon superconductivity can be made.

8.3 Superconductivity

In contrast to the high-T_c copper oxides, the C_{60}-based superconductors[169], with T_c's exceeding 30 K, are isotropic three-dimensional systems At first glance, the C_{60} systems look more amenable to theoretical analysis than the oxides. However, there is still not a general consensus on the origin of superconductivity or on the nature of various electron-electron interactions in these materials. The discussion proceeds from the assumption that

the doped C_{60} materials are conventional BCS superconductors, with a brief discussion of the ramifications of more exotic pairing mechanisms

In BCS and Eliashberg [1, 4] models for T_c, the primary parameters determining the superconducting properties are the electron-phonon coupling constant λ, the Coulomb repulsion μ, and some average phonon energy E_D. For standard band structure models of metals, μ is renormalized to μ^*,

$$\frac{1}{\mu^*} = \frac{1}{\mu} + \ln\frac{E_F}{E_D} \tag{8.1}$$

and μ is typically reduced by a factor of 2 to 5. Strong coupling effects arising from electron-phonon renormalization and quasiparticle damping change λ to $\lambda^* = \lambda/(1 + \lambda)$ yielding a McMillan [2] equation for T_c of the form

$$T_c = 1.14\omega_c\, e^{\left(-\frac{1}{\lambda^* - \mu^*}\right)}, \tag{8.2}$$

which is appropriate for $\lambda < 1.5$. Numerical constants can be included in Eqn. (8.2), as was done by McMillan to fit the case of Nb.

The electron-phonon coupling parameter λ can be expressed [2] in terms of $\langle I^2 \rangle$, a Fermi surface average of the square of the matrix elements representing the scattering of electrons by an atomic displacement. We obtain

$$\lambda \sim \frac{N(E_F)\langle I^2 \rangle}{M\langle \omega^2 \rangle}, \tag{8.3}$$

where M is the atomic mass and $\langle \omega^2 \rangle$ represents an average of the square of the phonon frequencies [2]. Eqn. 8.3 for λ can be interpreted as the ratio of an average electronic spring constant and an average lattice vibrational or phonon spring constant. If the $\langle \omega^2 \rangle$ are related to the C-C bond oscillations, then one would expect similar phonon spring constants for C_{60} solids and graphite[161, 162]. Hence, from this point of view the significantly higher T_c's for M_3C_{60}, where M is an alkali metal atom, arises from the numerator in Eqn. 8.3. As mentioned earlier, it is expected that the curvature of the C_{60} molecule

opens up additional scattering channels not available in doped graphite. In graphite the mirror plane symmetry yields $\langle I^2 \rangle = 0$ for several displacement-induced electron scatterings when matrix elements are taken between s and p_z states. The curvature in the C_{60} case mixes these states and yields non-zero matrix elements which can increase λ substantially above that in graphite intercalated compounds.

It is widely held that the intraball vibrational modes dominate the electron-phon coupling. In this model, the C_{60} molecules reside in a sea of electrons with sufficient charge transfer to create bands ≤ 1 eV in width. Electronic charge density plots [135, 136] reveal spread-out charge distributions consistent with the itinerant-electron picture of this model. The diameters of the C_{60} molecules and their separations are both ~ 10 Å. Hence electrons pair via phonons localized on the molecules, but retain their band-like itinerant nature. In most of these models, vibrations arising from coupling between molecules or from movement of the alkali atoms are considered to be less important than intraball excitations because of the higher energies (and presumably significant coupling) of the latter.

The above model of pairing via intraball phonons has been justified to some extent by measurements of T_c as a function of pressure and as a function of different substitutions for M in M_3C_{60}. A negative dependence on pressure was found for M=K and Rb [170], where $\frac{\partial T_c}{\partial P} \sim$ -0.8/Kbar. A similar effect arises when larger alkalis are used [171]. A increase in lattice constant or volume causes a decrease in band width, an increase in $N(E_F)$, and a concomitant increase in λ. For example, T_c increases from 19.3 K for K_3C_{60} to 29.4 K for Rb_3C_{60} when the lattice constant increases from 14.253 Å to 14.436 Å.

Although the data for T_c versus lattice constant is monotonic, it is not exactly linear as is sometimes claimed. A striking linear relation has been found found [172] between the measured T_c and the calculated $N(E_F)$. It is tempting to interpret this dependence as a signal of non-BCS behavior since the weak-coupling formula most commonly used for T_c is exponentially dependent on $N(E_F)$. However, T_c varies exponentially with λ at low

λ and as $\sqrt{\lambda}$ at large λ. In fact, a good approximation to the solution of the Eliashberg equations for $\mu^* = 0$ is [9, 10]

$$T_c = 0.25 \frac{\sqrt{\langle \omega^2 \rangle}}{\sqrt{e^{\frac{2}{\lambda}} - 1}}. \tag{8.4}$$

This function has a linear dependence on λ in an intermediate range of λ. Hence, the linear dependence of T_c on $N(E_F)$ can be explained within conventional BCS-Eliashberg theory if the coupling parameters are in the appropriate range.

One assumption inherent in the above model is that the variation of $N(E_F)$ does not significantly change λ or μ apart from a multiplicative factor. Screening effects could reduce the electron-phonon matrix elements for the larger values of $N(E_F)$, yielding a nonlinear dependence of λ on $N(E_F)$. This is an open problem at this point, and it bears on the relevance of the model.

The various theoretical on-ball phonon-induced pairing proposals differ primarily in the phonons considered to be important for the pairing. Because of the wide spectrum of phonon energies, the choice of the parameters λ and μ depend sensitively on the choice of phonon frequencies. In the models proposed, the average phonon energies and coupling strengths are $\omega \sim 1100$ K with $\lambda \sim 0.6$[161], $\omega \sim 1300$ K with $\lambda \sim 0.6$ [173], $\omega \sim 2000$ K with $\lambda \sim 0.5$ [174], and $\omega \sim 500$ K with $\lambda \sim 1.0$ [175]. Since weakly and strongly coupled superconductors have different experimental signatures for various properties, these could be used to constrain the values of λ. Two experiments which bear on this distinction are the superconducting gap-to-T_c ratio $2\Delta/kT_c$ and the discontinuity in the heat capacity at T_c. We are unaware of data for the latter, while infrared measurements [176] of Δ suggest that $\frac{2\Delta}{k_B T_c} \sim 3.5$, which suggests weak coupling and hence moderate values of λ.

Raman scattering provides another approach for estimating λ [166]. By examining broadening effects on various phonon contributions to the Raman spectrum, an estimate of the electron-phonon coupling can be obtained. Some theoretical distillation of the data is necessary and extrapolations to obtain contributions of phonons having non-zero q are

needed. In general, the results yield couplings which are consistent with the theoretical models of the superconductivity and suggest a particularly important role for the lower $H_g(2)$ mode with $\omega \sim 600$ K.

Critical field data provide another source of information on the superconducting parameters. Measurements of the upper critical field of single crystal K_3C_{60}[177] yield H_{c2}=17.5 T, which implies a coherence length of 45 Å. Analysis of $H_{c2}(T)$ yields a scattering time $\tau \sim 1 - 2 \times 10^{-14}$ sec, in accord with transport measurements[157]. Using a penetration depth of roughly 5000 Å, as suggested by muon spin relaxation data[178] and Ginzburg-Landau theory[157, 179], we obtain $\kappa \sim 100$, indicating strong type-II behavior.

Although the evidence to date favors the phonon models of superconductivity based on intraball vibrations, we briefly consider the possibilities of "rescuing" an alkali-mediated mechanism. The low alkali vibrational frequencies require strong coupling to reproduce the experimental T_c's. The alkali phonons could strongly polarize the adjacent C_{60} molecules, yielding strong coupling [160]. The main objections to such a mechanism are the lack of a change in T_c upon substitution of Rb for K at the same lattice constant, and the large carbon isotope effect.

As discussed previously, the alkali atoms probably vibrate in strongly anharmonic potentials, which could decrease the superconducting isotope effect for these modes [22, 102] as seen in PdH(D) [17, 18, 71]. In addition, the potential will change form for ions of different radius. These effects could explain the slight increase in T_c upon substitution of Rb for K, although a quantitative analysis awaits a better knowledge of the alkali atom vibrational potentials. However, the lack of a significant [87]Rb to [85]Rb isotope effect[180] reduces the attractiveness of this mechanism. Should the primary carbon phonon contribution to λ be of high frequency, then even a strong anharmonicity to the alkali atom vibrations will not reconcile a small alkali isotope effect with a significant electron-alkali phonon coupling. On the other hand, if the main carbon phonon contribution to λ arises from the low frequency interball modes, then a reasonable anharmonicity to the alkali vibrations

is sufficient to depress the alkali isotope effect even for large alkali atom electron-phonon coupling.

A mechanism based purely on alkali vibrations cannot account for the substantial carbon isotope effect. One is forced to include a contribution from phonons involving carbon atoms. Consider a model in which interball vibrational motions supplement the alkali atom contributions to the electron-phonon coupling. The M_3C_{60} system is close to a phase transition to the M_4C_{60} bct phase[181, 182]. The bulk motions of the C_{60} molecules corresponding to distortions into this structure could be anharmonic, with a softening of the quadratic potential. This form of potential could enhance the carbon isotope effect, [102, 21] yielding $\alpha_{carbon} \approx 0.3$ even though the carbon phonons do not dominate the superconductivity. Such potentials should be pressure-dependent, implying an unusual pressure dependence of the carbon isotope effect. Another possible source of an isotope-effect enhancing anharmonic potential is the very low frequency librational modes.

Within an alkali-phonon model, the broadening of the intraball Raman-active phonons upon doping would be interpreted as an effect of the orientational disorder of the doped phase. A large value of the gap ratio [183, 207] becomes a natural consequence of strong coupling. The possibility of a large value of the Coulomb repulsion μ^* [160] would not have as profound an effect on T_c as in a weakly coupled superconductor. However, the relatively low frequencies of the alkali vibrations appears inconsistent with the temperature dependence of the resistivity, which shows curvature at high temperatures. This temperature dependence cannot be accounted for by temperature-dependent anharmonic contributions to the resistivity from the various multiphonon transitions which become important at higher temperatures since such transitions will contribute negative curvature to the temperature dependent resistivity. The most likely phonon mechanism by far for superconductivity remains weak-to-moderate coupling to high frequency intraball phonons.

The previous discussion has assumed that the electron-phonon interaction is the cause

of superconductivity in the doped fullerenes. We now consider the possibility that correlation effects between electrons on the same C$_{60}$ molecule could produce an effective pairing interaction. The standard starting point for a discussion of strong electron correlation is the Hubbard Hamiltonian [184]

$$H = -t \sum_{(nn)} (c_{i\sigma}^{\dagger} c_{j\sigma} + h.c.) + \frac{U}{2} \sum_{i,\sigma} n_{i\sigma} n_{i-\sigma}, \qquad (8.5)$$

where the first term describes the kinetic energy of the electrons hopping between sites i and j and the second term describes the Coulomb repulsion between electrons of different spins on the same site. The model assumes that the Coulomb interaction is strongly screened, since only an on-site Coulomb term is incorporated.

We consider a Hubbard model where the site index refers to individual carbon atoms on a C$_{60}$ molecule. The pair binding energy is defined as the difference in energy between two C$_{60}$ molecules with three electrons each and one molecule with two and another molecule with four. At first glance, the repulsive nature of the Coulomb interaction appears to guarantee that the electrons will prefer to spread out uniformly between the balls, resulting in a negative pair binding energy. However, strongly correlated electron systems often exhibit subtle behavior. Exact numerical solutions for small model systems [185], and second-order perturbative results for a 60-site system [186, 187] yield a positive binding energy for intermediate values of the ratio $\frac{U}{t}$. Examination of the spin-charge correlation function on a C$_{60}$ molecule[188] indicates that this pair binding cannot be interpreted in terms of spin-charge separation[187, 189]. Instead, the pair binding results from the dominance of the pair-scattering contributions to the energy[188].

The model allows for a substantial carbon isotope effect through isotopic variation in the hopping matrix element t. The hopping rate between carbon atoms will be a function of the bond length, which will change upon isotopic substitution due to the influence of anharmonic terms on the zero-point motion. The pairing energy is a function of the hopping matrix element, and the transition temperature is a sensitive function of the

pairing energy,

$$T_c \sim W e^{-\frac{W}{E_{pair}}},$$ (8.6)

where W is the electronic bandwidth. The change in the C-C bond length upon substitution of ^{13}C for ^{12}C yields a change in T_c of roughly 0.5 K,[190] in accord with experiment. The tiny isotopic change in bond length is a factor of ten or twenty smaller than the dynamic changes in bond length due to intraball phonons, suggesting an important role for fluctuations in this model of superconductivity.

A difficulty with this model is the assumption that the Coulomb interaction is screened completely over the distance of a carbon-carbon bond. The inclusion of a nearest-neighbor Coulomb repulsion strongly suppresses the pair binding, resulting in no pairing for a nearest-neighbor repulsion on the order of $\frac{U}{20}$ [185]. Perturbative results for a screened Coulomb interaction indicate that the regime of negative pair binding energy for a more realistic system occurs at values of $\frac{U}{t}$ beyond those which are likely to be physically relevant,[191] and also well beyond the values for which the perturbation theory is accurate. In fact, a Hubbard-like model is more likely to be relevant to interball hopping and on-ball Coulomb interactions.

8.4 Conclusions

The one-electron theory of relatively narrow bands arising from molecular states of different orbital character appears to work reasonably well for the pristine and doped C_{60} systems. The most plausible model of the superconductivity involves high-frequency on-ball carbon phonons weakly to moderately coupled to the electrons. The following chapters provide detailed analysis of experimental results relevant to the normal state and superconducting properties of these novel systems.

Chapter 9

Upper Critical Field

Upper critical field measurements provide a wealth of information on the microscopic parameters relevant to superconductivity and normal-state transport. We discuss results of magnetoresistance measurements in A. Zettl's group on K and Rb-doped single crystal C_{60}, beginning with the measurements on K_3C_{60}.

The measurements of K_3C_{60} directly yield the upper critical field between T_c=19.7 K and 13 K. Further analysis nets the intrinsic parameters $H_{c2}(0)$, the coherence length ξ, the penetration depth λ, the scattering time τ, the mean free path ℓ, and the zero-temperature resistivity $\rho(0)$. These parameters provide a self-consistent picture of the normal and superconducting states within Bloch-Boltzmann transport and Eliashberg theory.

K-doped C_{60} single crystals were prepared using a sublimation/growth method developed in A. Zettl's group[192]. X-ray diffraction of the crystals prior to doping confirmed the well-known fcc structure. Electrical measurements were made using van der Pauw and in-line four probe contact geometries with gold leads attached with silver paint to evaporated silver pads. The sample temperature was monitored with a carbon-glass resistance thermometer.

Fig. 9.1 shows the resistivity near the superconducting transition of a K_3C_{60} sample for applied fields up to 7.3 T. The inset shows the zero field resistivity over an extended temperature range. Above $T_c(H=0)$=19.7 K (transition midpoint) the resistivity displays a metallic temperature dependence. The transition to the superconducting state is sharp, $\Delta T \approx 250$ mK at zero field. The applied dc current was small enough to ensure minimal Joule heating effects. Although the transition broadens slightly under the higher magnetic fields, the increase in ΔT evidences none of the anomalous broadening seen in the copper
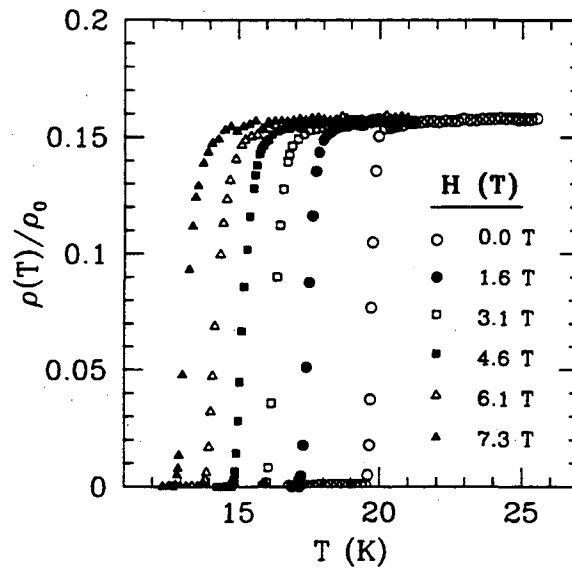
Figure 9.1: Normalized resistivity of K_3C_{60} near T_c for different applied fields H. ρ_0 is 0.4 times the resistivity at T=300 K.

oxide superconductors. This sharpness allows a clear identification of $H_{c2}(T)$.

Using the resistivity midpoints to define the T-H critical line we obtain $H_{c2}(T)$ as shown in Fig. 9.1. A linear fit near $T_c(H = 0)$ yields $\frac{dH_{c2}}{dT} = -1.34$ K. Because it is not immediately clear if K_3C_{60} is in a clean or dirty limit, we perform an analysis valid for arbitrary mean free path.

The $H_{c2}(T)$ data is analyzed to extract the scattering time τ. The critical field is related to the scattering time by the expression [193]

$$\frac{1+\lambda}{\lambda - \mu^*} = 2\pi \frac{T}{T_c} \sum_{i=0}^{N_c} \frac{1}{\chi_i^{-1} - (2\tau^*)^{-1}}, \tag{9.1}$$

where

$$\chi_i = \frac{2}{\sqrt{\alpha^*}} \int_0^\infty e^{-q^2} tan^{-1} \left(\frac{q\sqrt{\alpha^*}}{(2i+1)\pi \frac{T}{T_c} + \frac{1}{2\tau^*}} \right) dq. \tag{9.2}$$

The magnetic field enters through the expression

$$\alpha^* = \frac{1}{2} e H_{c2}^* v_f^{*2}, \tag{9.3}$$

where we have the renormalized quantities

$$H_{c2}^* = \frac{H_{c2}}{(1+\lambda)T_c}, \tag{9.4}$$

$$v_f^* = \frac{v_f}{\sqrt{(1+\lambda)T_c}}, \tag{9.5}$$

and

$$\tau^* = \tau(1+\lambda)T_c. \tag{9.6}$$

The sum is limited to the range

$$i < N_c = \frac{1}{2} \left(\frac{\bar{\omega}}{\pi T} + 1 \right). \tag{9.7}$$

These expressions derive from a two-square well analysis of the Eliashberg theory of the upper critical field. Within this two-square well model we have

$$T_c = 1.13\bar{\omega}e^{-\frac{1+\lambda}{\lambda - \mu^*}}, \tag{9.8}$$

which determines λ for given values of T_c, $\bar{\omega}$, and μ^*. Pauli limiting has been neglected, an approximation consistent with the relatively small value of $\frac{dH_{c2}}{dT}\frac{1}{1+\lambda}$ [193].

In order to proceed with the analysis, we must assume values for the Coulomb repulsion μ^*, the average phonon frequency $\bar{\omega}$, and the Fermi velocity v_f. The Coulomb repulsion is taken to be in the range $0.1 \leq \mu^* \leq 0.3$. We obtain the Fermi velocity from a band structure calculation[147] which yields $v_f = 1.8 \times 10^7 \frac{cm}{sec}$. The average phonon frequency is estimated within various theoretical electron-phonon models of the superconducting properties of this material[174, 175, 173]. These three models yield very similar results. The models of Schluter et al. and Jishi et al. yield $\tau \approx 1.7 \times 10^{-14}$ sec for $\mu^* = 0.2$, whereas the model of Varma et al. yields $\tau \approx 1.6 \times 10^{-14}$ sec. Assuming $\mu^* = 0.1(0.3)$ produces scattering times roughly 0.2×10^{-14} sec smaller (larger). Taking into account the uncertainties in the calculation, we estimate the zero-temperature scattering time of the sample to be of the order $1 - 2 \times 10^{-14}$ sec, with a mean free path of 27 ± 7Å. The extrapolated zero-temperature upper critical field is 17.5 T, implying a coherence length of 45 Å, which indicates that K_3C_{60} is in neither the clean nor the dirty limit.

The calculation is sensitive to the Fermi velocity, with τ varying roughly as the inverse Fermi velocity squared. The band structure calculation which yields v_f assumes orientational order of the C_{60} molecules, at variance with experimental results[149], which imply random occupation of two orientations. A tight-binding calculation[150] indicates that this disorder will smear out the peaks in the density of states. However, the density of states at the Fermi level is roughly equal for the ordered and disordered systems, suggesting (but not guaranteeing) that the actual Fermi velocity is not substantially different from the oriented case.

Knowledge of the scattering time and the plasma frequency allows a derivation of the resistivity by the relation $\rho = \frac{4\pi}{\omega_p^2 \tau}$. A band structure calculation[147] yields a plasma frequency of 1.2 eV, close to the free electron value of 1.3 eV for three electrons per C_{60} and an effective mass of $m^* \approx 3.6m_e$, the value which brings the free electron Fermi velocity
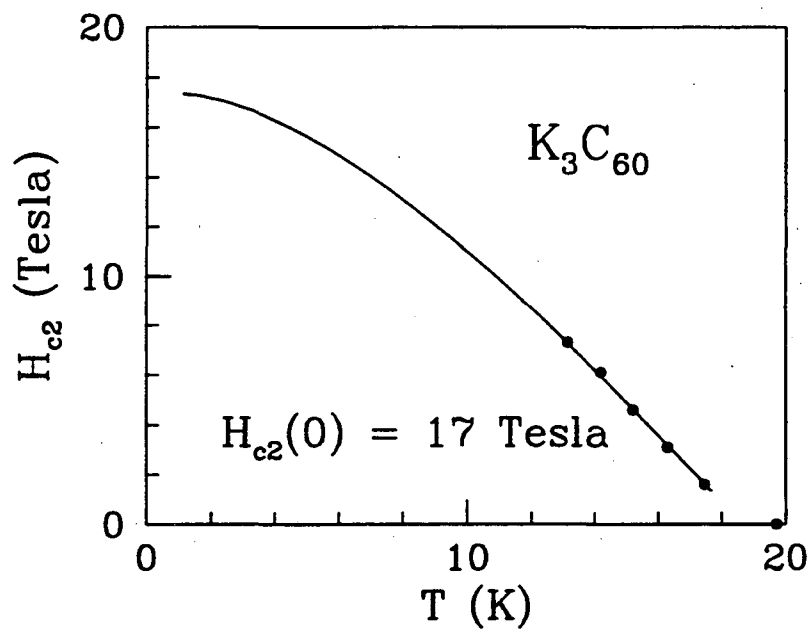
Figure 9.2: Temperature dependence of H_{c2}. Circles are experimental data and solid line is theoretical calculation.

into agreement with the band structure result. Using a plasma frequency of 1.2 eV and $\tau = 1.7 \pm 0.5 \times 10^{-14}$ sec, we estimate the zero temperature resistivity to be of order $\rho(0) = 0.18 \pm 0.06 \text{m}\Omega\text{-cm}$. This value is in good agreement with $\rho(0) \approx 0.12 \text{m}\Omega\text{-cm}$ from fluctuation conductivity measurements[194]. Although uncertainties in effective sample geometry complicate direct measurements of the resistivity, the most reliable results to date yield $\rho(0) \approx 0.5 \text{m}\Omega\text{-cm}$, the same order of magnitude as the indirect results and comparable to measurements on thin film samples[195].

We briefly consider the sensitivity of the calculation to errors in the bare plasma frequency. The plasma frequency varies as $\omega_p \sim \sqrt{\langle N(0)v_f^2 \rangle}$, so that a smaller plasma frequency may imply a smaller Fermi velocity, which implies a longer scattering time. A smaller plasma frequency and longer scattering time tend to cancel in the calculation of the resistivity, suggesting that the calculated resistivity is relatively insensitive to uncertainties in ω_p. The mean free path, the product of the scattering time and the Fermi velocity, behaves similarly.

Assuming a plasma frequency of 1.2 eV, we obtain a London penetration depth of $\lambda_L = \frac{c}{\omega_p} = 1560$ Å. Using Ginzburg-Landau theory with $\tau = 1.7 \pm 0.5 \times 10^{-14}$ sec yields $\lambda(0) \approx 2400 \pm 300$ Å. For comparison, muon spin relaxation measurements yield $\lambda \approx 4800 \pm 800$Å[178], whereas lower critical field measurements on powder samples[196] suggest $\lambda \approx 2400$Å. The Ginzburg-Landau theory can also be applied to derive the clean limit coherence length $\xi_0 \approx 135 \pm 20$Å. This value is slightly larger than that obtained from Allen's formula

$$\xi_0 = \sqrt{\frac{4\zeta(3)}{7}} \frac{\hbar v_f}{2\pi k_B T_c (1 + \lambda)}, \qquad (9.9)$$

which yields $\xi_0 \approx 80 - 110$ Å for $\lambda = 0.5 \rightarrow 1.0$, the relevant range for the models studied.

We note a caveat in the Ginzburg-Landau analysis in that real systems deviate somewhat from the Ginzburg-Landau temperature dependence. The quoted errors in $\lambda(0)$ and ξ_0 take into account uncertainties in τ but do not include deviations from the simple version

of Ginzburg-Landau theory used. Our analysis also ignores interball electron-electron cor-relations which may be significant for this relatively narrow band system. We also remark that our analysis assumes metallic conduction, i.e. $k_f \ell > 1$. Although K_3C_{60} crystals appear to satisfy this condition, the relatively high normal state resistivity suggests the possibility of nonconventional scattering mechanisms. The results for the superconducting and normal state parameters of K_3C_{60} have been summarized in Table 9.1 for convenience.

Similar experiments were performed for Rb-doped single crystal C_{60}. In contrast to K_3C_{60}, the resistive transition in Rb_3C_{60} is substantially broadened by the magnetic field, necessitating a detailed treatment of the resistive transition to extract accurate values of $T_c(H)$. In analogy to the copper oxide superconductors, we consider two mechanisms of broadening, thermodynamic fluctuations[194] and dissipative flux line motion[197]. The results suggest that the transition onset is dominated by thermodynamic fluctuations while the broadening near the transition "foot" is mediated by flux creep with a characteristic activation energy substantially lower than that found for conventional superconductors. The analysis of fluctuation magnetoconductivity provides accurate estimates of the true thermodynamic T_c, thereby yielding the upper critical field $H_{c2}(T)$. The H_{c2} data are then analyzed in a manner similar to that for K_3C_{60} to extract the scattering time τ.

High quality C_{60} single crystals were prepared by vapor transport and characterized by x-ray diffraction. Rb doping procedures were similar to those used for K[192]. The electrical resistivity was measured using a dc four probe Van der Pauw configuration. The inset to Fig. 9.3 shows the metallic resistivity of Rb_3C_{60} over a wide temperature range for H=0. Good sample homogeneity is indicated by the similarity of the functional forms for the two components of the Van der Pauw resistance. The superconducting transition width is less than 200 mK. The main body of Fig. 9.3 shows the resistive transition for different applied fields. Measurements on different samples yield similar results, indicating that the broadening is intrinsic. Comparison of the fitted values of $\frac{dH_{c2}}{dT}$ for T_c defined as transition onset (-4.04 T/K) versus the transition midpoint (-3.14 T/K) clearly indicates the need
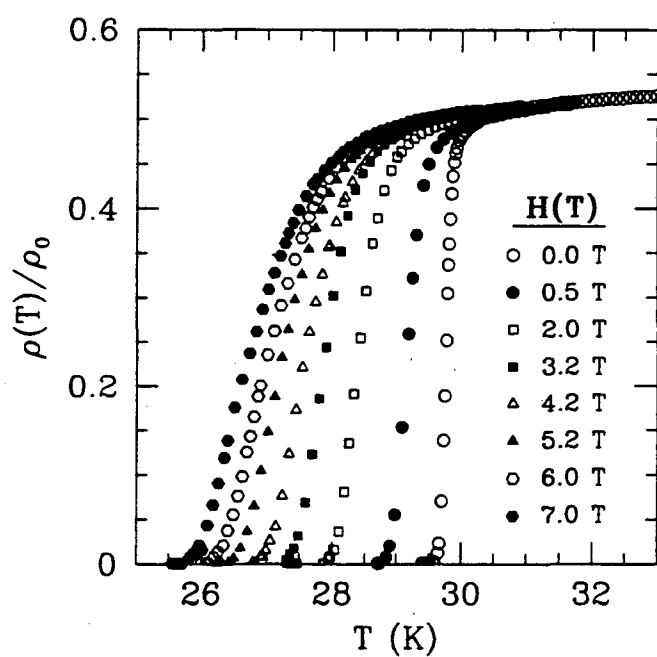
Figure 9.3: Resistivity versus temperature for Rb_3C_{60} at the superconducting transition for several applied fields H.

for a detailed analysis of the transition broadening to extract the true thermodynamic T_c.

We first investigate the origin of the magnetic field induced broadening for the upper portion of the resistive transition. In the absence of applied magnetic field, Rb_3C_{60} displays fluctuation conductivity with excess conductivity proportional to $t^{-\frac{1}{2}} \equiv \left(\frac{T-T_c}{T_c}\right)^{-\frac{1}{2}}$[194], the behavior expected of a bulk three dimensional superconductor. Under finite field the divergence of the fluctuation conductivity shifts to lower temperatures and becomes anisotropic. For a bulk superconductor in the dirty limit with H parallel to the dc current the excess conductivity in the high field limit is $\sigma \propto H^{\frac{1}{2}}t^{-\frac{3}{2}}$, similar to the result for one-dimensional filaments (in both cases the allowed states in momentum space are cylinders). H perpendicular to the current yields $\sigma \propto H^{\frac{1}{2}}t^{-\frac{1}{2}}$, with the same temperature dependence as the zero field case. Although the applied fields do not access the high field limit, a small admixture of this functional form may occur. In addition, the application of magnetic field near the transition onset will make it energetically favorable for the real-space regions of fluctuating superconductivity to elongate along the field axis, potentially yielding a one-dimensional contribution to the fluctuations even when the sample is not in the high-field limit.

The crystals in the study concerned were roughly $0.5 \times 0.5 \times 1.0 mm^3$ with the magnetic field approximately perpendicular to the largest surface. Because the conductivity was measured in the Van der Pauw configuration, the current has components both parallel and perpendicular to the field, implying a magnetic field dependent fluctuation conductivity of the form $\sigma \approx AH^{\frac{1}{2}}t^{-\frac{3}{2}} + BTH^{-\frac{1}{2}}t^{-\frac{1}{2}}$ where A and B are field and temperature-independent fitting parameters. Fig. 9.4 shows the fits thus obtained. Fig. 9.5 shows in detail the resistive transition for H=3.2 T along with the calculated magnetofluctuation curve, exhibiting the good agreement and showing the fitted value of T_c(3.2 T). similar fits for different applied fields yield a well defined thermodynamic T_c(H) (or H_{c2}(T)). However, before turning to a discussion of H_{c2}(T) we first investigate a second mechanism which can explain the lower portion of the broadened superconducting transition, dissipative flux
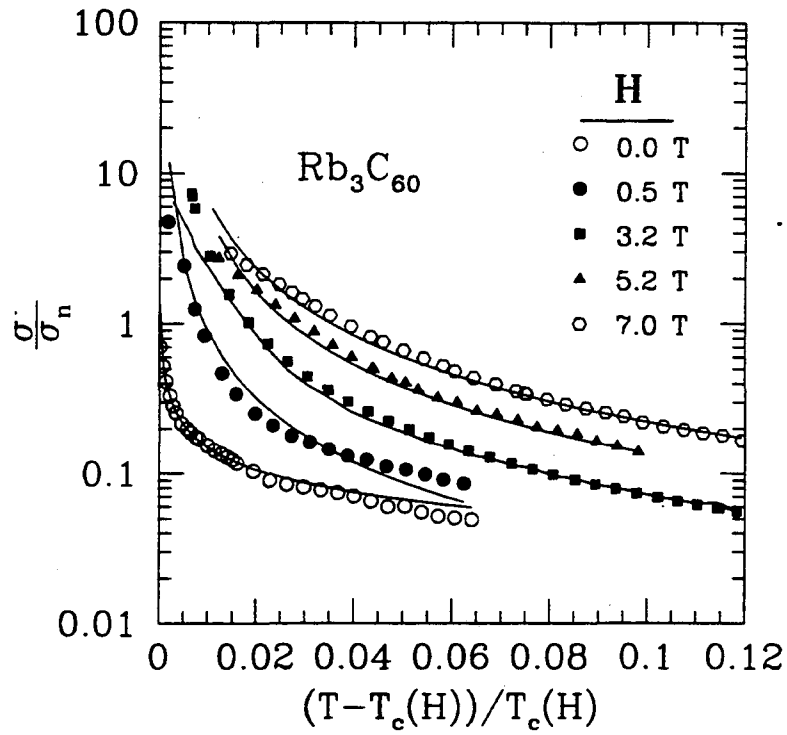
Figure 9.4: Normalized excess fluctuation conductivity versus reduced temperature for Rb$_3$C$_{60}$ in different applied magnetic fields. Solid lines are fits to $\sigma' = AH^{\frac{1}{2}}t^{-\frac{3}{2}} + BTH^{-\frac{1}{2}}t^{-\frac{1}{2}}$ (see text) with fitting parameters $A = 1.23 \times 10^{-4}$ and $B = 5.5 \times 10^{-5}$.
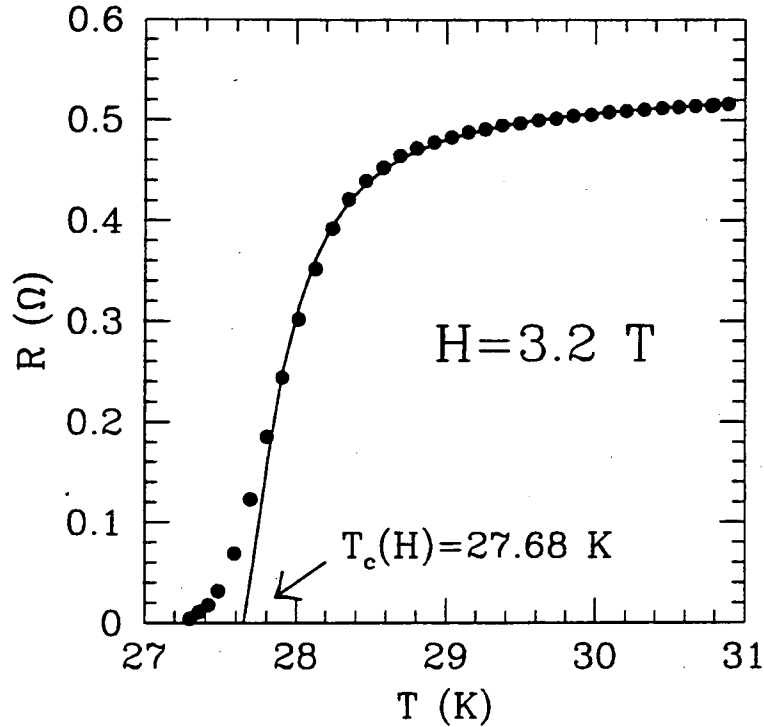
Figure 9.5: Resistance versus temperature for H=3.2 T. Solid line is the fit to fluctuation conductivity σ'.

creep.

The fit in Fig. 9.5 is excellent for the upper portion of the transition but degrades at lower temperatures, suggesting an additional mechanism of broadening which is proposed to be dissipative flux line motion. Taking a thermally activated jumping rate proportional to $e^{-\frac{U}{k_BT}}$ with U the activation energy we obtain a resistivity of[198]

$$\rho = \frac{2\nu_0 LH}{J} \exp -\frac{U}{k_BT} \sinh \frac{JHV_cL}{k_BT}, \tag{9.10}$$

where ν_0 is the attempt frequency for hopping of flux lines or bundles, U is the barrier height, L is the hopping distance and V_c is the volume of a vortex. Taking a hopping

distance equal to the intervortex distance a_0 leads to the relation $V_c L \approx a_0^3 L_c$, where L_c is the flux line length. For small current density (the region explored by experiment) we obtain

$$\rho \approx \frac{2\nu_0 \Phi^2 L_c}{k_B T} \exp - \frac{U}{k_B T} = \rho_c \exp - \frac{U}{k_B T}, \tag{9.11}$$

where $\Phi = H a_0^2$ is the flux quantum. Motivated by results for copper-oxide supercon-ductors, we assume the simple scaling form $U(T,H) = U(H)(1 - t^2)^{\frac{3}{2}}$ where $U(H)$ is a field dependent activation energy. The prefactor ρ_c depends weakly on temperature and is taken as a constant in the temperature region of interest. The semilog plot of Fig. 9.6 confirms the relevance of Eqn. 9.11 with constant ρ_c. Fig. 9.7 shows $U(H)$. Taking a power law form for $U(H)$ yields two field regimes, $U \propto H^{-0.32}$ for $H < 2$ T and $U \propto H^{-1.25}$ at larger fields.

We emphasize two salient features of flux creep dissipation in $Rb_3 C_{60}$. First, the activation energies are small, less than 1 eV, as compared to several eV for conventional superconductors. Second, the ratio of the resistivity prefactor ρ_c to the normal state resistivity is less than unity and independent of field, temperature and sample, a situation in marked contrast to the copper oxides, wherein the ratio $\frac{\rho_c}{\rho_n}$ attains extremely large values to which it is difficult to give a physical interpretation[199]. Finally, we note that near the transition onset, the regions of fluctuating superconductivity in real space will have dimension much smaller than the penetration depth, suggesting that the dissipative flux creep broadening will not greatly interfere with the fluctuation conductivity contributions in this temperature range.

A linear fit to the fluctuation-determined T_c's yields $\frac{dH_{c2}}{dT} = 3.28$ T/K. The H_{c2} data have been analyzed in a manner similar to that previously applied to $K_3 C_{60}$. The fairly large value of $\frac{dH_{c2}}{dT} \frac{1}{1+\lambda}$ for $Rb_3 C_{60}$ indicates the importance of Pauli limiting, which has been included in the analysis[193].

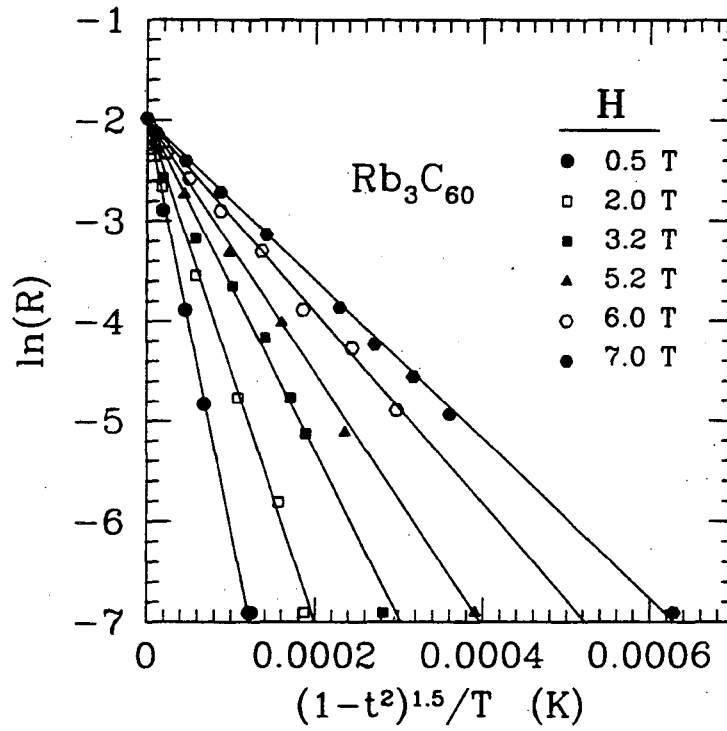The treatment requires values for the Coulomb repulsion μ^*, the average phonon fre-

Figure 9.6: $\ln R$ versus $\frac{(1-t^2)^{\frac{3}{2}}}{T}$ in the flux creep regime. The solid lines are fits to Eqn. 9.11.
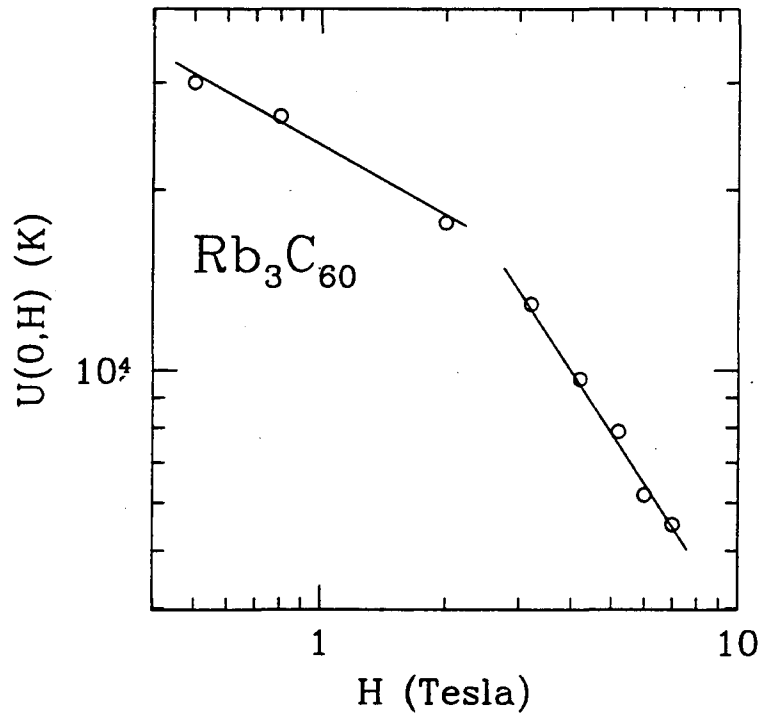
Figure 9.7: Field dependent activation energy U(0,H). Solid lines are fits to power law behavior, $U_0 \propto H^{-m}$ where m=1.25 for H>3 T and m=0.35 for H<2 T.

quency $\bar{\omega}$, and the Fermi velocity v_f. The Coulomb repulsion is taken to be in the range $0.1 \leq \mu^* \leq 0.3$. The Fermi velocity can be approximated in two manners. A preliminary band structure calculation for K_3C_{60} at the Rb_3C_{60} lattice constant yields $v_f \approx 1.56 \times 10^7 \frac{cm}{sec}$ [200]. This value is corroborated by a simple rescaling of the K_3C_{60} Fermi velocity by the ratio of the density of states for Rb and K doped C_{60}, [172] which yields $v_f \approx 1.47 \times 10^7 \frac{cm}{sec}$. We take $v_f \approx 1.5 \times 10^7 \frac{cm}{sec}$. Estimates of the average phonon frequency are loosely based on three theoretical electron-phonon models of the superconducting properties of this material[174, 175, 173]. The models of Jishi et al., Schluter et al. and Varma et al. are taken to have $\bar{\omega} \approx$500 K, 1000 K, and 2000 K respectively. Taking $\mu^* = 0.2$, we obtain $\tau \approx 5.5 \times 10^{-15}$ sec (Jishi), $\tau \approx 7 \times 10^{-15}$ sec (Schluter) and $\tau \approx 7.5 \times 10^{-15}$ sec (Varma). Assuming $\mu^* = 0.1(0.3)$ produces scattering times roughly 1.0×10^{-15}sec smaller (larger). Taking into account the uncertainties in the calculation, we estimate the zero-temperature scattering time of the sample to be of the order $0.4 - 1.0 \times 10^{-14}$sec, implying a mean free path of $l \approx 11 \pm 5$Å, several times the interatomic spacing. The extrapolated zero-temperature upper critical field is 62 T, which yields a coherence length of $\xi(T = 0) \approx$24 Å. (For comparison, a treatment neglecting Pauli limiting would have yielded a critical field of 68 T.) Since the coherence length is of the same order as the mean free path, Rb_3C_{60} is in neither the clean nor the dirty limit. For comparison, we note that a previous rf absorption measurement suggested that Pauli limiting is significant and yielded a result of $H_{c2}(0)$=73 T [201].

Knowledge of the scattering time and the plasma frequency allows an estimation of the resistivity from the relation $\rho = \frac{4\pi}{\omega_p^2 \tau}$. A preliminary band structure estimate[202] yields a plasma frequency of 1.11 eV, close to the free electron value of 1.25 eV for three electrons of effective mass $3.6m_e$ per C_{60} (this value of the effective mass reproduces the band structure Fermi velocity). This value is corroborated by reflectivity and electron energy loss measurements on K_3C_{60}, which is expected to have a comparable plasma frequency (theoretical estimates suggest a plasma frequency for K_3C_{60} roughly 10% larger

than that of Rb_3C_{60}). Infrared reflectivity measurements have been fit by a Drude model with a plasma frequency of 1.56 eV [203]. Electron energy loss spectroscopy measures the plasma frequency screened by the background dielectric constant of $\epsilon = 4.4$[204]. These measurements yield a peak in the loss spectrum at 0.55 eV which corresponds to an unscreened plasma frequency of 1.15 eV [205]. For resistivity calculations, we use the theoretical value of $\omega_p = 1.11$ eV and the scattering time of $0.4\text{-}1.0\times10^{-14}$ sec to obtain a zero-temperature resistivity of 0.57 ± 0.21 mΩ-cm. This value compares well to theoretical calculations of 0.39 mΩ-cm[151] and 0.42 mΩ-cm[206] and infrared measurements of 0.7 mΩ-cm [207]. The present result is slightly larger than an estimate based on analysis of fluctuation conductivity near T_c which yields 0.23 mΩ-cm.

Knowledge of ω_p, $\xi(0)$ and τ allows estimation of the penetration depth λ and BCS coherence length ξ_0 within Ginzburg-Landau theory[179]. A plasma frequency of 1.11 eV implies a London penetration depth of $\lambda_L = \frac{c}{\omega_p} = 1690$Å in the clean limit. Allowing for the finite value of τ within Ginzburg-Landau theory yields $\lambda(T = 0) = 3200 \pm 800$ Å. Similarly, the experimental value for the zero temperature coherence length, $\xi(0) = 24$ Å, together with $\tau \approx 0.4 - 1.0 \times 10^{-14}$sec yields a BCS clean limit coherence length of $\xi_0 \approx 85 \pm 15$Å. Similar to the case of K_3C_{60}, this value is somewhat larger than that obtained from Allen's formula,

$$\xi_0 = \sqrt{\frac{4\zeta(3)}{7}} \frac{\hbar v_f}{2\pi k_B T_c (1 + \lambda)}, \tag{9.12}$$

which yields $\xi_0 \approx 46 \pm 8$ Å for $\lambda = 0.6 \to 1.3$, the relevant range for Rb_3C_{60}.

The linear relation between H_{c2} and temperature breaks down for fields below roughly 2 Tesla. A similar nonlinearity has been seen in Rb_3C_{60} powder and K_3C_{60} powder and doped single crystal samples. The observation in doped single crystals indicates that the deviation is likely not caused by sample inhomogeneity. Instead, this "foot" may be the result of flux creep, since a large thermally activated flux creep near T_c would drastically reduce the critical current and in effect suppress T_c[197]. A flux creep model predicts
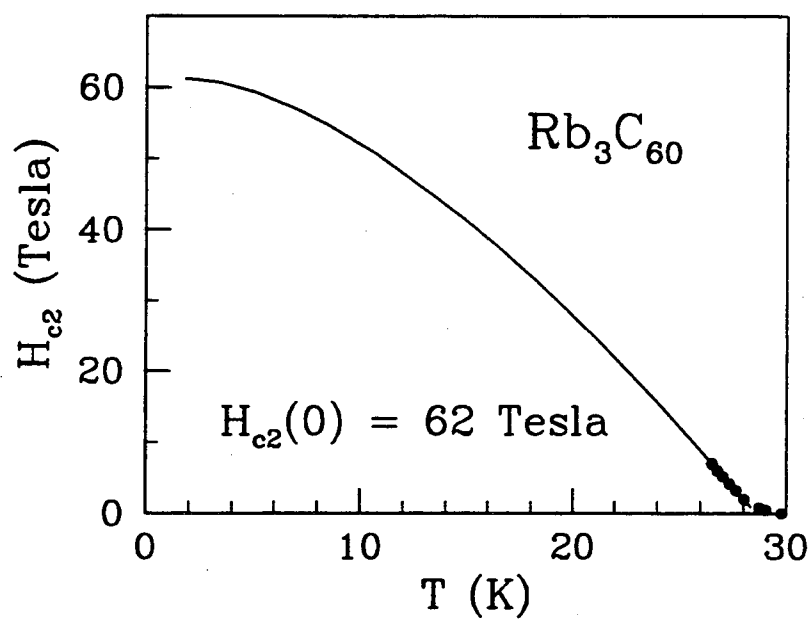
Figure 9.8: Upper critical field $H_{c2}(T)$ for Rb_3C_{60}. Solid dots are experimental data with transition temperatures derived from fits to fluctuation conductivity. Solid line is theoretical result.

$H_{c2} \propto (T_{c0} - T)^{1.5}$, as compared to a best fit exponent of 1.52 for H<2 T and $T_c0=29.8$ K. Prominence of thermally activated flux creep at low field and high T_c is consistent with the small activation energy derived from the flux creep analysis of the transition broadening.

Alternatively, the "foot" could arise from a breakdown of Ginsburg-Landau theory in the regime where the fluctuations in the order parameter are of the same order as the order parameter itself[208]. Such a situation arises in the temperature range

$$|T - T_c| < 10^{-9} \frac{\kappa^4 T_{c0}^3}{H_{c2}(0)} \tag{9.13}$$

where κ is the ratio of penetration depth to coherence length. Within this range one obtains $H_{c2}(T) \propto (T_{c0} - T)^{1.34}$[208], with a crossover to linear behavior at lower temperature. Taking $\kappa \approx 130$ yields a range of roughly 0.1 K, somewhat smaller than that observed experimentally for the low field foot.

In conclusion, upper critical field measurements yield a wealth of information on the intrinsic parameters characterizing the normal and superconducting states of K_3C_{60} and Rb_3C_{60}. These results are summarized in Table 9.1, which provides a reasonably self-consistent picture of the transport properties of the alkali-doped fullerenes.

Parameter	K_3C_{60}	Rb_3C_{60}
T_c	19.7 K	30.8 K
$\frac{dH_{c2}}{dT}$	-1.34 T/K	-3.28 T/K
$H_{c2}(0)$	17.5 T	62 T
$\xi(0)$	45 Å	24 Å
ξ_0	96 ± 16 Å[a] ,130 ± 15 Å[b]	46 ± 8 Å[a], 85 ± 15 Å[b]
$\lambda(0)$	2400 ± 300 Å[b]	3200 ± 800 Å[b]
λ_L	1560 Å[c]	1690 Å[c]
κ	53 ± 10	130 ± 40
τ	$1.7 \pm 0.5 \times 10^{-14}$ sec	$0.7 \pm 0.3 \times 10^{-14}$ sec
ℓ	31 ± 7 Å	11 ± 5 Å
$\rho(T \to 0)$	0.18 ± 0.06 mΩ-cm[d]	0.57 ± 0.21 mΩ-cm[d]

Table 9.1: Superconducting and normal-state parameters of K_3C_{60} and Rb_3C_{60}.

[a] from Allen's formula 9.12

[b] within Ginzburg-Landau theory [179]

[c] from Ref. [147]

[d] assuming $\omega_p(K_3C_{60})$=1.2 eV[147], $\omega_p(Rb_3C_{60})$=1.1 eV[200].

Chapter 10

Transport

10.1 Superconducting Fluctuations

Just above T_c, thermodynamic fluctuations produce small transient regions of the superconducting state, causing an anomalous increase in the normal state conductivity. The form of the temperature dependence of fluctuation conductivity is strongly dependent on dimensionality. Measurements on K and Rb doped single crystal C_{60} in A. Zettl's group provide the first (to our knowledge) observation of pure three dimensional fluctuation conductivity. These results in addition allow an indirect determination of the normal state resistivity, an important intrinsic parameter. Synthesis of K_3C_{60} and Rb_3C_{60} followed standard techniques pioneered in the Zettl group. A standard in-line four probe contact configuration with small (10-100μA) dc current provided the resistivity measurements.

Figs. 10.1 and 10.2 show a detailed view of the superconducting transition for K_3C_{60} and Rb_3C_{60}. Just above T_c, the resistivity deviates from normal-state behavior before dropping precipitously at T_c. We associate this deviation with superconducting fluctuations. The fluctuation conductivity σ' is obtained by subtracting the extrapolated normal state conductivity from the measured values. The appropriate form for extrapolation at low temperatures is expected to be the Bloch T^5 form, although in the relevant temperature range a simple linear extrapolation also provides a reasonable fit. Both materials were fit the normal state to the temperature range from 1.4 T_c to 2.0 T_c, using a T^5 form for K_3C_{60} and a simple linear fit for Rb_3C_{60}, choices which provide good agreement both at high temperatures($T{\sim}2.0T_c$) and (for K_3C_{60}) at lower temperatures ($T{<}1.4T_c$)under finite magnetic field. The conclusion that three dimension fluctuation conductivity has
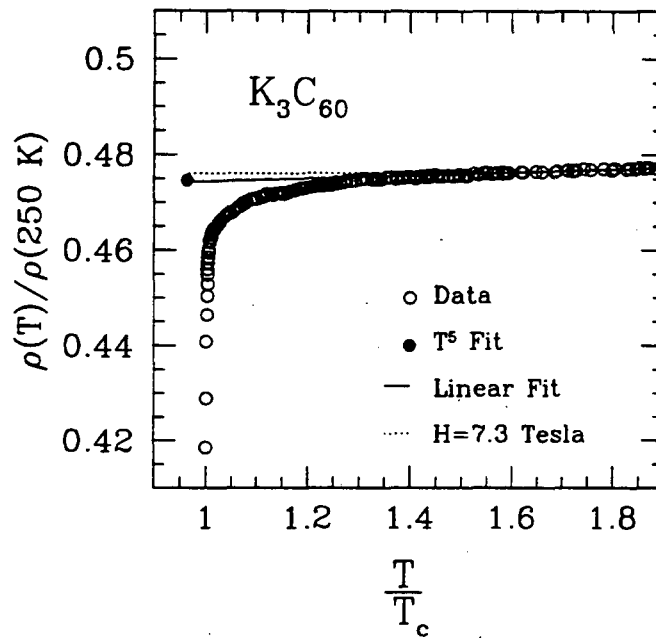
Figure 10.1: Normalized resistivity as a function of $\frac{T}{T_c}$ for K_3C_{60}. Circles are experimental data and lines are extrapolations of the normal state resistivity. Solid line is a linear extrapolation, dashed line is a T^5 extrapolation. A single high-magnetic-field resistivity point is also shown.
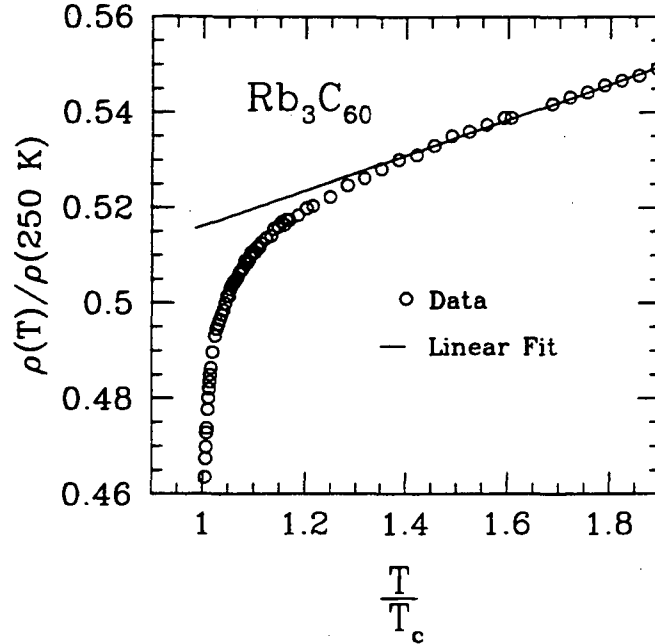
Figure 10.2: Normalized resistivity as a function of $\frac{T}{T_c}$ for Rb_3C_{60}. Circles are experimental data and solid line is a linear extrapolation of the normal state resistivity.

been observed is not sensitive to the choice of fitting form. The ambiguity in fitting form introduces roughly a 20% error into the values derived for the intrinsic normal state residual resistivity.

The Aslamazov-Larkin fluctuation conductivity is given by[209]

$$\sigma'_{AL} \sim t^{\frac{4-d}{2}}, \tag{10.1}$$

where d is the dimensionality of the sample and t is the reduced temperature $t \equiv \frac{T-T_c}{T_c}$. The AL term, known as the regular fluctuation conductivity, arises from the direct acceleration of fluctuation-induced superconducting pairs of quasiparticles. The Maki-Thompson term[210, 211], an additional source of fluctuation conductivity, arises from the scattering of normal state quasiparticles by the superconducting fluctuations. The sum of these two

terms yields

$$\sigma'_{3d} = \sigma'_{AL} + \sigma'_{MT} = \sigma_{excess}\left(t^{-\frac{1}{2}} + \frac{4}{t^{\frac{1}{2}} + \delta^{\frac{1}{2}}}\right) \qquad (10.2)$$

where δ is a pair-breaking parameter which determines the relative strength of the Maki-Thompson term[212]. The prefactor σ_{excess} is related to the coherence length by

$$\sigma_{excess} = \frac{e^2}{32\hbar\xi(0)}. \qquad (10.3)$$

The log-log plots of Figs. 10.3 and 10.4 show the best fits to the data for three dimensional fluctuation conductivity as expressed by Eqn. 10.2. The K_3C_{60} data is best fit by a fairly small Maki-Thompson contribution with $\delta \approx 0.58$, whereas the fit to the Rb_3C_{60} data yields a negligible anomalous contribution and a large δ, a result consistent with a larger electron-phonon coupling in Rb_3C_{60}[213]. The fit to the Rb_3C_{60} excess conductivity also shows the best fits for dimensionalities 1 and 2, providing strong support for an interpretation in terms of three dimensional fluctuation conductivity.

As a superconductor approaches T_c from above the coherence volume of the superconducting fluctuations grows monotonically unless limited by reduced dimensionality at larger length scale, as would be the case for a granular superconductor. Granular superconductors exhibit zero dimensional crossover in the form of the fluctuation conductivity as the Ginzburg-Landau coherence length approaches $\sim \frac{1}{3}$ of the characteristic grain size[214]. Such crossover would be signaled by an increase in slope at small t. The absence of zero dimensional crossover down to $t \approx 0.0005$ gives a lower limit for the grain size of roughly 0.6μm, a value at least 100 times the zero-temperature coherence length, a value guaranteeing that local physical parameters measured on these samples represent intrinsic properties of the K_3C_{60} phase.

Uncertainties in effective sample geometry render difficult a direct measurement of the absolute resistivity of alkali doped fullerenes. Although different samples yield identical normalized fluctuation conductivity curves (i.e. identical $\frac{\sigma'}{\sigma_n}$), these samples show scatter in the absolute magnitude of σ_n. However, nature is kind in that the coherence

Figure 10.3: Log-log plot of the normalized fluctuation conductivity versus $\frac{T}{T_c}$ for K_3C_{60}. Circles are experimental data and line is theoretical fit.
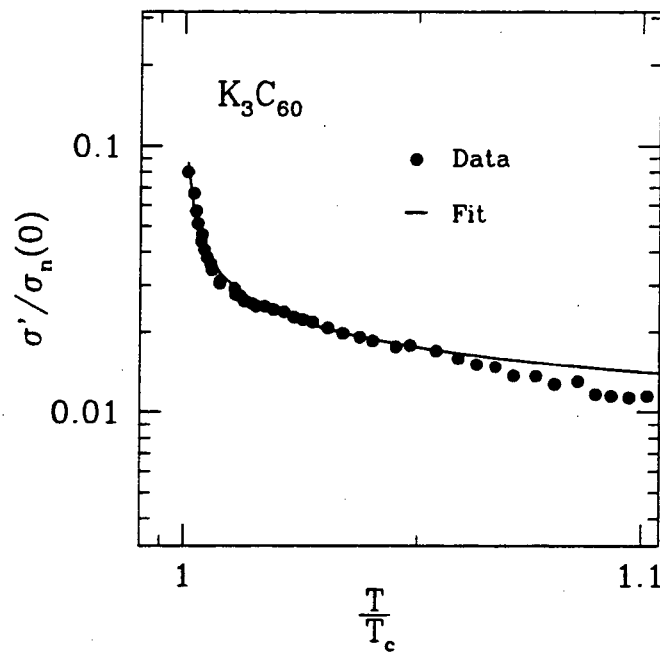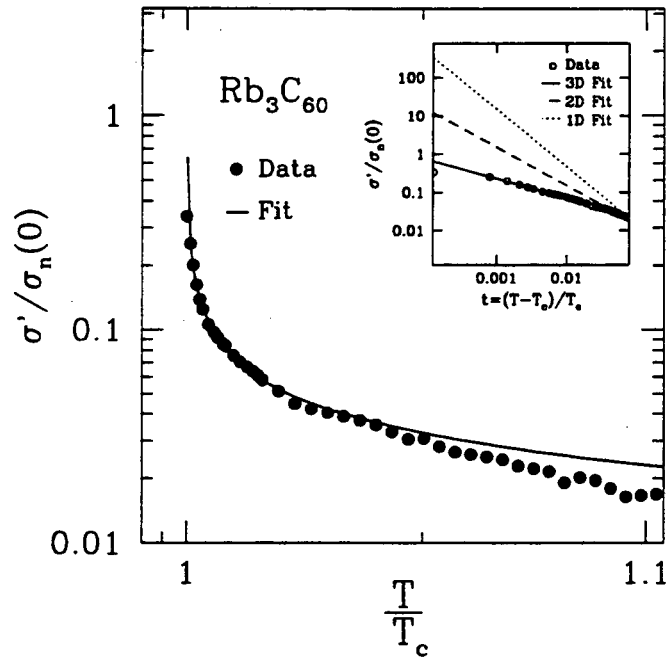
Figure 10.4: Log-log plot of the normalized fluctuation conductivity versus $\frac{T}{T_c}$ for Rb_3C_{60}. Circles are experimental data and line is theoretical fit. Inset shows a log-log plot of the normalized fluctuation conductivity versus reduced temperature $t \equiv \frac{T-T_c}{T_c}$ for theoretical fits with different dimensionalities

length determined by upper critical field measurements provides a means to determine the absolute magnitude of σ_{excess} through Eqn. 10.3. Using the experimental values $\frac{\sigma_{excess}}{\sigma_n} \approx 2 \times 10^{-3}$ and $\xi \approx 45\text{Å}$ for K_3C_{60} and $\frac{\sigma_{excess}}{\sigma_n} \approx 7.3 \times 10^{-3}$ and $\xi \approx 24\text{Å}$ for Rb_3C_{60} yields $\rho(T=0) \approx 0.12m\Omega$-cm for K_3C_{60} and $\rho(T=0) \approx 0.23m\Omega$-cm for Rb_3C_{60}, with uncertainties of roughly 20%. These estimate are in reasonable agreement with the most reliable direct measurements ($\rho \approx 0.5m\Omega$-cm for K_3C_{60})[195, 215], infrared studies ($\rho \approx 0.4m\Omega$-cm for Rb_3C_{60})[207], calculations based on H_{c2} measurements ($\rho \approx 0.18m\Omega$-cm for K_3C_{60} [177] and $\rho \approx 0.57m\Omega$-cm for Rb_3C_{60}[216]) and disordered supercell calculations ($\rho \approx 0.39m\Omega$-cm for both materials[151]).

As this is to our knowledge the first observation of pure three dimensional fluctuation conductivity in an isotropic superconductor, it is appropriate to address the difficulty in observing similar behavior in other materials (most conventional superconductors are of course three dimensional). Fluctuation conductivity has been reported for the high-temperature cuprate superconductors; however, strong anisotropy, materials difficulties and uncertainties as to the microscopic mechanism have clouded the situation and there is at present no consensus as to the dimensionality of the observed fluctuations. For conventional superconductors, the fractional change in conductivity $\frac{\sigma'}{\sigma_n} \approx \frac{k_B T_c}{E_f} \frac{1}{k_f \ell} t^{\frac{1}{2}}$ is of order $\sim 10^{-7} t^{\frac{1}{2}}$, much too small to be observed in any accessible temperature interval above T_c (E_f is the Fermi energy, k_f is the Fermi wavevector and ℓ is the mean free path). In such materials one must introduce large concentrations of impurities or defects in order to reduce ℓ and increase $\frac{\sigma'}{\sigma_n}$. These modifications generally imply reduced dimensionality in the form of granularity. In contrast, the isotropic fullerene-based superconductors possess a very short intrinsic mean free path (due to orientational disorder), a short coherence length, a relatively small Fermi energy and a high T_c, all of which contribute towards the salience of three dimensional fluctuation conductivity.

10.2 Temperature-Dependent Resistivity of K_3C_{60}

Determination of the transport mechanisms in alkali-doped C_{60} can provide valuable information pertinent to superconductivity. Transport measurements[192, 177] for K- and Rb-doped single crystals of C_{60} have been analyzed in terms of both electron-electron and electron-phonon scattering processes. For simplicity, it is assumed that one or the other mechanism is dominate so as to elucidate the primary physical consequences of either scattering process.

The small bandwidth and large on-site Coulomb interaction[138] in the doped fullerenes suggest a role for electron-electron interactions. The standard treatment of electron-electron scattering yields a T^2 temperature dependence due to phase-space factors. Motivated by these considerations, the resistivity data have been fit to a form $\rho(T) = a + bT^2$, shown as the solid line of Fig. 10.5. A log-log plot of the raw experimental data actually yields a slope of 1.73. The situation is reminiscent of the organic conductors, several of which exhibit a nearly quadratic temperature dependence up to high temperatures[217]. However, the theoretical T^2 dependence assumes constant volume. Thermal expansion will increase the density of states at the Fermi level, producing a resistivity $\rho(T) = a + b(N_0(T)T)^2$, where $N_0(T)$ is the temperature-dependent density of states at the Fermi level. We have taken account of this effect by combining thermal expansion data for *undoped* C_{60}[218] and density of states versus lattice constant results from a pseudopotential calculation[172] (use of thermal expansion for doped C_{60} yields essentially equivalent results). The quality of the fit decreases, as evidenced by the dashed line in Fig. 10.5. The insert shows a log-log plot of the resistivity data corrected for thermal expansion compared to a line of slope 2. The thermally corrected data have a shallower slope and are slightly nonlinear. (mention results with correct thermal expansion data) In this context we note that theoretical results that suggest that metallic screening could be very efficient,[219] suggesting that electron-electron interactions are not domi-

nant. More importantly, direct measurements at constant sample volume yield a near linear temperature dependence to the resistivity[220], a further indication that electron-electron scattering is not the primary scattering mechanism. Unfortunately, the results at constant volume have not yet been reproduced, so the detailed analysis to follow focuses upon the well characterized constant pressure measurements.

The absolute magnitude of the resistivity is inconsistent with a predominantly electron-electron scattering mechanism. On a very simplistic level, the first Born approximation for a Coulomb potential screening by a Thomas-Fermi screening length of 0.45 Å yields an electron-electron scattering time of $\tau_{ee} \sim 10^{-12}$ sec at 250 K. A much more rigorous calculation[221] yields $\tau_{ee} \approx 4 \times 10^{-13}$ sec at 250 K for K_3C_{60}. In these derivations the alkali-doped system was treated as a free electron gas with an effective mass of $3m_e$. This value for the effective mass gives reasonable agreement with band structure results for the Fermi velocity and the plasma frequency. This compares to a much smaller experimental non-residual scattering time of $\tau \approx 1.7 \pm 0.5 \times 10^{-14}$ sec at 250 K, another indication that the temperature-dependent resistivity in alkali-doped C_{60} is not due to electron-electron scattering.

We next examine the data from the point of view of electron-phonon coupling. We begin with the Ziman resistivity formula, [222]

$$\rho(T) = \frac{8\pi^2}{\omega_p^2 k_B T} \int_0^{\omega_{max}} \frac{\hbar\omega \alpha_{tr}^2 F(\omega)}{\cosh\left(\frac{\hbar\omega}{k_B T}\right) - 1} d\omega, \qquad (10.4)$$

which relates the resistivity to the transport electron-phonon coupling function $\alpha_{tr}^2 F(\omega)$. In most cases $\alpha_{tr}^2 F(\omega)$ provides a reasonable approximation to $\alpha^2 F(\omega)$, the expression relevant to superconductivity. The transport expression weighs the differences in Fermi velocities between different points on the Fermi surface. The two expressions could be significantly different if the electron-phonon matrix elements have a strong dependence on wavevector. However, the intramolecular phonons should exhibit very little dispersion, strongly suggesting that the electron-phonon coupling for these modes is isotropic in k-
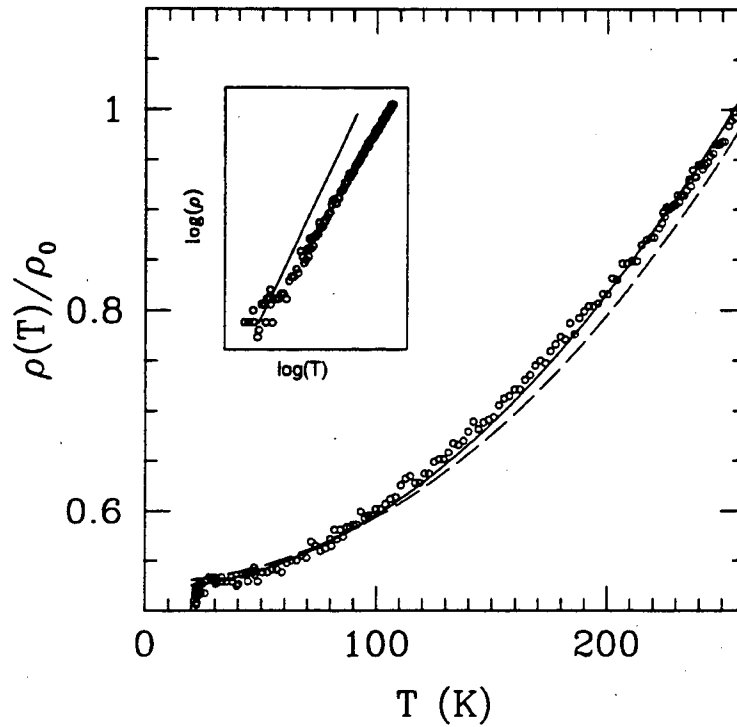
Figure 10.5: Fits of theoretical electron-electron scattering models to the experimental resistivity (circles). The solid line is a fit to the form $a + bT^2$. The dashed line is a fit to the form $a + b(N_0(T)T)^2$, where $N_0(T)$ is the temperature-dependent density of states. The experimental data have been normalized to the value at T=260 K. The insert shows a log-log plot of the resistivity after correction for thermal expansion compared to a line of slope 2.

space. Meroscopic orientational disorder[149] should further encourage isotropic coupling. The situation is less clear for the lower frequency librational, vibrational and alkali modes. Phase space factors suggest that phonons along cartesian directions will be preferentially weighed in the electron-phonon coupling integral. These nesting phonons have two flavors: those that bridge across necks of the Fermi surface and those that nest along the flat sides of these necks. The first (second) variety yields fairly large (small) differences in Fermi velocities. If the electron-phonon matrix elements for the low frequency phonons are anomalously large or small for either variety of nesting wavevector, then these modes could contribute to $\alpha_{tr}^2 F(\omega)$ and $\alpha^2 F(\omega)$ to differing degrees. As a caveat, the phase space results assume orientational order, at variance with experiment[149].

The Ziman formula assumes an isotropic, energy-independent scattering time. An fcc crystal such as K_3C_{60} should be reasonably isotropic. The approximation of an energy-independent scattering time typically overestimates of the resistivity at intermediate temperatures[222]. In addition, the Bloch-Boltzmann transport formalism assumes that $N(0)\omega_{Debye}$ is small[223], a questionable assumption for a system with high phonon frequencies and a potentially large density of states. A final concern is that the Bloch-Boltzmann theory fails for mean free paths on the order of the interatomic spacing. Recent upper critical field measurements on single crystal samples imply a T=0 mean free path on the order of 27 Å[177], substantially larger than the interatomic separation and somewhat larger than the intermolecular spacing.

Before analyzing the experimental resistivity data, we discuss the importance of the absolute magnitude of the resistivity to the calculations. Experimental geometrical uncertainties imply that the magnitude of the resistivity is uncertain by roughly a factor of two. For this reason, we appeal to an analysis of upper critical field data, which suggest a scattering time of $1.7 \pm 0.5 \times 10^{-14}$ sec [177]. The fitted values of λ are dependent solely on the scattering time, not the resistivity. The scattering time determines the overall scale of the electron-phonon coupling, while the functional form of the temperature dependence

provides a constraint on the frequency distribution of the electron-phonon coupling.

In order to gain a measure of physical insight into the form of $\alpha_{tr}^2 F(\omega)$, we first fit the data with a delta-function form, $\alpha_{tr}^2 F(\omega) = \frac{1}{2}\lambda\omega\delta(\omega - \bar{\omega})$, yielding $\bar{\omega} \approx 400$ K and $\lambda \approx 0.6$. This drastic simplifying assumption is not directly physically relevant. However, the simple fit implies that a more physical analysis should involve modes with frequencies both above and below 400 K.

To proceed further, we consider various theoretical calculations for the electron-phonon coupling. The model of Jishi et al.[175] (JD) emphasizes the lower-frequency radial intra-ball modes, producing an average frequency of roughly 500 K and $\lambda \approx 1$. The models of Schluter et al.[173] (SLNB) involves contributions from a broad range of H_g modes with an average frequency of $\omega_{log} \sim 1000K$ and $\lambda \approx 0.6$. The particular model chosen for detailed analysis is the first listed in Table I of [173]. In contrast, the calculations of Varma et al.[174] (VZR) yield significant coupling only to the two highest H_g modes at frequencies near 2000 K, with $\lambda \approx 0.5$. These models are evaluated by two criteria: the correspondence of the theoretical and experimental temperature dependences, and the magnitude of λ necessary to reproduce the experimentally measured resistivity. For each model, the overall coupling strength and the residual resistivity were adjusted in a least-squares fit to the data.

Referring to Fig. 10.6, JD produces a reasonable fit to the temperature dependence over the range 0-260 K. At high temperatures the theoretical curve has a somewhat smaller slope than the experimental results. SLNB and VZR do not adequately reproduce the measured temperature dependence. The quality of the fits is decreased further if the residual resistivity is fixed at the experimental value. The insufficient curvature at low-temperatures suggests additional coupling at a lower frequency. Motivated by this consideration, we include a lower frequency contribution of adjustable strength, with the results presented in Fig. 10.7. The new phonon mode was set at a frequency of 150 K, but the quality of the fit and the magnitude of the coupling to this lower mode are roughly unchanged for
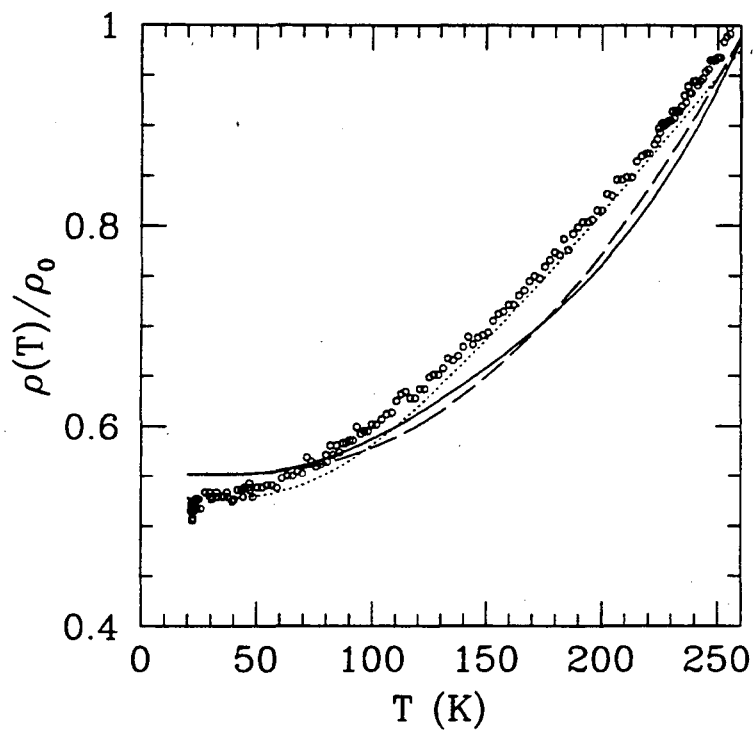
Figure 10.6: Fits of theoretical electron-phonon scattering models to the experimental resistivity for K_3C_{60} (circles). The solid, dashed, and dotted lines are for the models VZR[174], SLNB[173], and JD[175] respectively. The data have been normalized to the value at T=260 K.
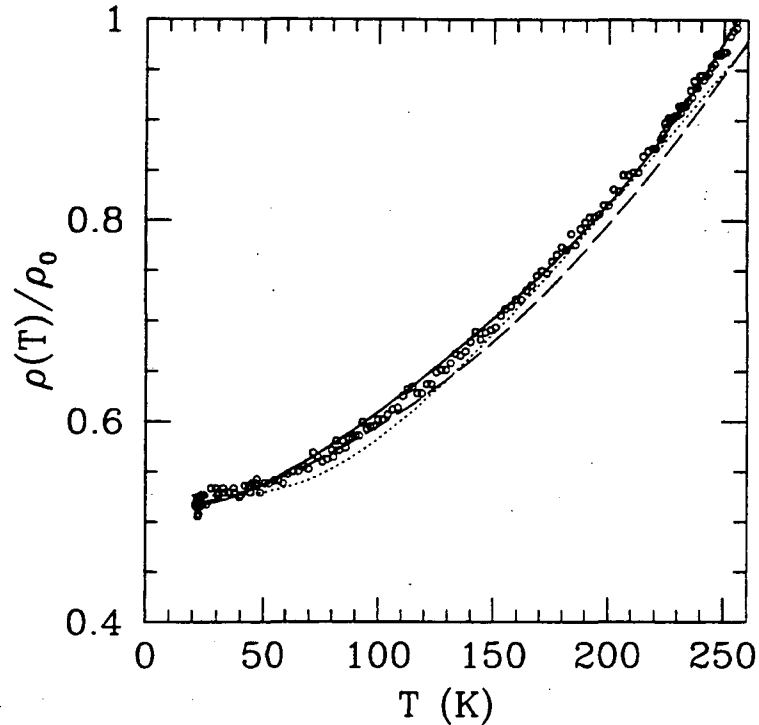
Figure 10.7: Fits of theoretical electron-phonon models with an additional phonon mode at 150 K to the experimental data for K_3C_{60}. The curve assignments are the same as Fig. 10.6.

frequencies in range 20-200 K. For SLNB and VZR, this modification greatly improves the agreement with experiment. This result is not an artifact of the additional free parameter; the fit is not improved if the additional mode is placed at a frequency above 400 K. Within the accuracy of the analysis, these three models yield agreement with experiment which is comparable to or better than that obtained by the electron-electron analysis. Consideration of the results at constant volume strengthens this conclusion.

Is there a physical motivation for the inclusion of a lower frequency mode? A back-of-the-envelope calculation yields an estimate of λ for interball translational modes. Within

a tight binding model, the bandwidth W varies as an overlap integral between electronic states $\phi(\vec{r})$ and $\phi(\vec{r} + \vec{R})$. Consider the change in the overlap integral under a change in lattice constant, where we assume that the on-ball electronic states are unchanged,

$$\delta W \sim \int \phi^*(\vec{r})\delta U(\vec{r})\phi(\vec{r} + \vec{R})d\vec{r}, \tag{10.5}$$

where U(r) is the deviation from superposed molecular potentials. This expression has the same form as a real-space formulation for the McMillan-Hopfield parameter $\langle I^2 \rangle$, which enters the expression for λ as $\lambda = \frac{N(0)\langle I^2 \rangle}{M\langle \omega^2 \rangle}$, [2] where $\langle \omega^2 \rangle$ is an average squared phonon frequency, M is the molecular mass, and N(0) is the density of states at the Fermi level. A low-q longitudinal interball vibrational phonon will produce a local change in the lattice constant. Using pseudopotential calculations to estimate the bandwidth and change in density of states upon lattice contraction, [172] we approximate λ by the expression $\lambda \sim \frac{W^2\left(\frac{\delta N}{\delta a}\right)^2}{NM\langle \omega^2 \rangle}$, which yields λ of order 0.1 for a mode of frequency ~ 100 K. More sophisticated tight-binding calculations for high-$\vec{q}$ intermolecular modes indicate large changes in the band structure, indicative of significant electron-phonon coupling[158]. Low-frequency librational modes could also exhibit significant coupling, since the overlap integrals between buckyballs will be sensitive functions of their relative orientations. Polarization of the C_{60} molecules by alkali atom vibrations could also produce a low-frequency contribution to the electron-phonon coupling[160].

The resistivity has also been fit to an $\alpha^2 F(\omega)$ corresponding to a uniformly scaled version of the inelastic neutron scattering intensity[155]. The approximation of constant coupling strength is unlikely to be valid, since the scattering data includes modes of qualitatively distinct character. In fact, this naive fit yields too strong a temperature dependence at low temperatures, suggesting excessive coupling to low frequency modes. If the modes below 25meV are removed by hand, the fit is too flat at low temperatures, suggesting that the lower frequency modes contribute to the scattering process, but less so then implied by the magnitudes of the peaks in the neutron scattering.

Table 10.1 shows the values of λ deduced from the fits to the resistivity data for each of the theoretical forms for $\alpha^2 F(\omega)$. The range of values corresponds to variations in the scattering time from 1.2-2.2×10^{-14} sec. JD yields λ slightly lower than that required to produce the observed T_c, whereas VZR yields λ too big. These results suggest that an electron-phonon model for superconductivity should include contributions from a broad range of intramolecular vibrations.

A correction for the effect of thermal expansion on the density of states yields a 10-15% reduction in the coupling to the higher frequency modes and little change in the coupling to the lower frequency mode. These changes do not substantively alter the conclusions of the analysis. The temperature dependence of the resistivity is reproduced to the same accuracy with or without the treatment of thermal expansion.

An estimate based on theoretical results for other superconductors[193] suggests that the preceding analysis will yield a near-BCS gap ratio of $\frac{2\Delta}{k_B T_c} \approx 3.6 - 4.0$. Preliminary tunneling measurements yield $\frac{2\Delta}{k_B T_c} = 5.3$,[183] while infrared measurements suggest $\frac{2\Delta}{k_B T_c} \sim 3.5$ [176]. The unambiguous determination of this important superconducting parameter merits further effort.

In conclusion, an analysis of resistivity data on doped single crystals of $K_3 C_{60}$ suggests that the superconductivity is consistent with conventional electron-phonon coupling involving a range of intramolecular phonons. Within this analysis, the coupling strength to lower frequency modes does not contribute significantly to either the superconducting transition temperature or the gap ratio.

10.3   Temperature-Dependent Resistivity of $Rb_3 C_{60}$

The temperature-dependent resistivity of Rb doped single crystals was analyzed by use of the Ziman resistivity formula in a manner similar to that used for a K-doped sample[157]. The absolute values of λ are derived by using a T=0 scattering time of

Model	λ_{High}	λ_{Low}
SLNB	1.0 - 2.5	$\cdots\cdots$
SLNB(low)	0.7 - 1.6	0.1 - 0.25
SLNB(low,thermal)	0.6 - 1.4	0.1 - 0.25
VZR	2.2 - 5.4	$\cdots\cdots$
VZR(low)	1.5 - 3.7	0.1 - 0.25
VZR(low,thermal)	1.3 - 3.1	0.1 - 0.3
JD	0.4 - 0.9	$\cdots\cdots$
JD(low)	0.4 - 0.9	0.01 - 0.02
JD(low,thermal)	0.3 - 0.8	0.03 - 0.06

Table 10.1: Best-fit values of λ_{High} and λ_{Low} to the temperature dependent resistivity for various theoretical models of the electron-phonon coupling. The expression λ_{High} refers to the total coupling to on-ball modes, while λ_{Low} refers to the coupling a mdoe at 150 K. The appellation "low" refers to the coupling function with this additional low frequency mode at 150 K. The appellation "thermal" implies that a correction for thermal expansion has been applied.

$\tau = 0.7 \pm 0.3 \times 10^{-14}$ sec., the value derived from upper critical field data[216]. The frequency distribution of the electron-phonon coupling is obtained from three different theoretical models of intramolecular electron-phonon coupling, denoted JD[175], SLNB[173] and VZR[174]. Additional contributions arise from interball and alkali modes, which occupy two frequency ranges. Interball librations for Rb_3C_{60} lie in the frequency range $\sim$50 K, whereas interball vibrations/alkali atom optical modes have frequencies around 150 K [155]. These two possible sources of additional electron-phonon coupling were considered separately. First, the three theoretical models were augmented with a variable-strength mode at 50 K which models librational modes. Second, each model was augmented by a mode at 150 K which models the vibrational and alkali modes. The range of results from these separate models should encompass the actual physical situation which is expected to be a combination of both low-frequency contributions.

The results of the analysis are summarized in Table 10.2 and Figs. 10.8 and 10.9. JD, which stresses the lower-frequency intramolecular phonons, is too linear at high temperatures. The introduction of an intermolecular contribution to the electron-phonon coupling does not improve the agreement with experiment. The actual values of the electron-phonon coupling derived from this analysis are consistent with the measured T_c of Rb_3C_{60}.

In contrast to JD, the model of VZR is dominated by the two highest-energy H_g modes. Before introduction of a low-frequency contribution, this model yields poor agreement with experiment at low temperatures. The introduction of either a 50 K or 150 K mode greatly improves the quality of the fit, with little difference between the two cases (only the 150 K case is shown). VZR yields rather large λ's which necessitate an extremely large Coulomb repulsion ($\mu^* \approx 0.7 - 0.9$) in order to be consistent with the measured T_c. These large values of μ^* yield very small isotope effect exponents, at variance with experimental results[224, 225]. In addition, these very large values of λ begin to approach the range in which the system would be expected to be unstable to a structural phase transition.

Like VZR, the model of SLNB profits greatly from the introduction of a low frequency
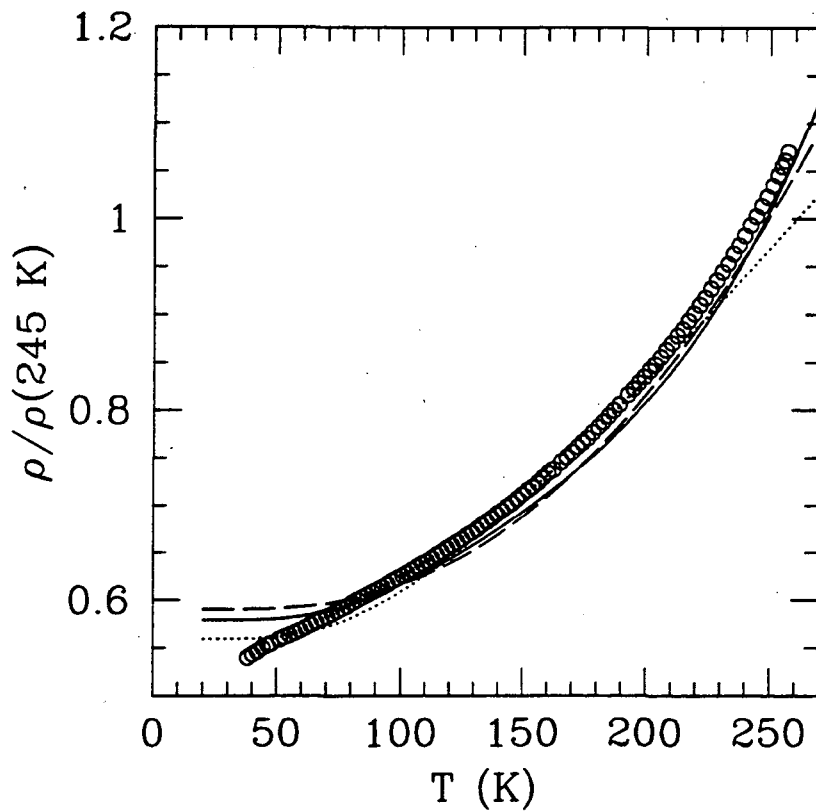
Figure 10.8: Fits of theoretical electron-phonon scattering models to the experimental resistivity for Rb_3C_{60} (circles). The solid, dashed, and dotted lines are for the models VZR[174], SLNB[173], and JD[175] respectively. The data have been normalized to the value at T=245 K.

Figure 10.9: Fits of theoretical electron-phonon models with an additional phonon mode at 150 K to the experimental data for Rb_3C_{60}. The curve assignments are the same as Fig. 10.8.

Table 10.2: Best-fit values of λ to the temperature dependent resistivity for various theoretical models of the electron-phonon coupling. The expression λ_{High}^{Rb} refers to coupling to the high frequency on-ball modes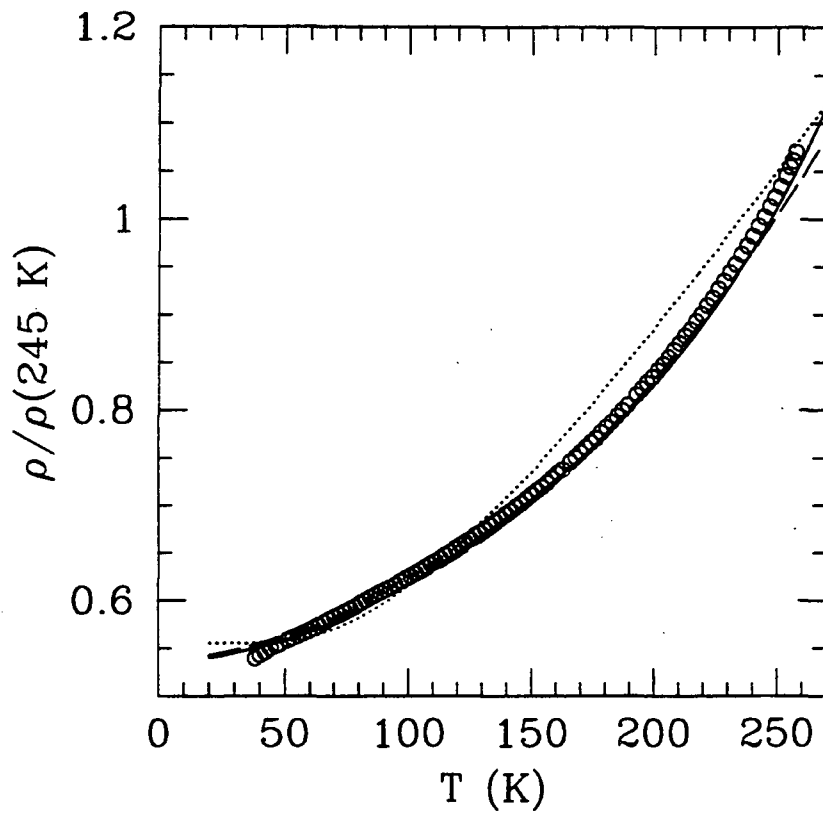 while λ_{Low}^{Rb} refers to an additional low frequency mode at 150 K. A correction for thermal expansion has been applied.

Model	λ_{High}^{Rb}	λ_{Low}^{Rb}
SLNB	2.0 ± 0.8	0.2 ± 0.08
VZR	5.4 ± 2.2	0.18 ± 0.07
JD	0.85 ± 0.34	~ 0.00

mode. In this case, the model with a mode at 150 K provides the best agreement with experiment. Like JD, SLNB yields values of the electron-phonon coupling for K and Rb doped C_{60} which are reasonably consistent with the measured superconducting transition temperatures.

We briefly consider the effects of phonon anharmonicity on the treatment of the resistivity. The best candidates for strong phonon anharmonicity are the vibrations of the alkali atoms, which reside in relatively large interstitial sites that could be associated with flat-bottomed potentials, as is seen for hydrogen atoms intercalated into the octahedral interstitial sites of a fcc palladium lattice. This anharmonicity would affect both the temperature dependence of the resistivity and the isotope effect exponent. A model of anharmonic phonons in superconductivity[21, 102] can be extended to a treatment of the resistivity. The temperature-dependent anharmonic electron-phonon coupling relevant to superconductivity, Eqn. 5.1, is identified with the electron-phonon coupling function relevant to transport processes, Eqn. 5.2. The resistivity is then calculated with the Ziman resistivity formula. We note a caveat that λ_{tr} may differ from λ if the electron-phonon coupling is anisotropic[223, 40]. Although the coupling to the low frequency mode

is weak, its contribution to the resistivity changes significantly upon assumption of anharmonic behavior, leading to substantial changes in the fitted values of λ. Preliminary analysis indicates that a treatment of SLNB in which the low-frequency contribution to the electron-phonon coupling is assumed to be purely quartic yields λ_{high} roughly 30% higher and λ_{low} roughly 20% smaller then a treatment assuming purely harmonic modes. The size of the electron-phonon coupling is still reasonably consistent with the experimental values of T_c and α. Similar changes in λ_{high} and λ_{low} are observed for VZR; however, the increase in λ_{high} for this model increases the disagreement with experiment. The model of JD, on the other hand, is almost unaffected by the introduction of low-frequency anharmonicity, since this treatment requires only a very small low-frequency contribution. In summary, the assumption of strong anharmonicity of the low frequency mode produces modest changes in the fitted values of the electron-phonon coupling, but not enough to affect the agreement with experiment.

10.4 A brief reanalysis of the temperature-dependent resistivity

The preceding analysis depends on an analysis of critical field data to determine the scattering time and thereby set the overall scale of the electron-phonon coupling. An alternative method is available, using fluctuation conductivity results to determine the absolute scale of the resistivity and then using the plasma frequency to derive the scattering time from $\rho = \frac{4\pi}{\omega_p^2 \tau}$.

Fluctuation conductivity results yield $\rho(T \approx 20K) = 0.12m\Omega$-cm for K_3C_{60} and $\rho(T \approx 30K) = 0.23m\Omega$-cm for Rb_3C_{60}. These values are reasonably consistent with an analysis of the upper critical field [177] which suggests resistivities of 0.18 ± 0.06mΩ-cm and 0.57 ± 0.21mΩ-cm for K_3C_{60} and Rb_3C_{60} respectively. Band structure calculations[147, 200] suggest bare plasma frequencies of $\omega_p^{K_3C_{60}} = 1.2eV$ and $\omega_p^{Rb_3C_{60}} = 1.1eV$. The value for Rb_3C_{60} is actually a preliminary result from a calculation of K_3C_{60} at the Rb_3C_{60} lattice

constant[200], which should be an adequate approximation.

An analysis similar to that performed previously, but using these parameters yields the values of λ given in Table 10.3. The results for K_3C_{60} are slightly lower than those of the original analysis, while the values of the coupling for Rb_3C_{60} are substantially smaller. For Rb_3C_{60}, the model of Jishi et al. yields values of the electron-phonon coupling which are generally too low to account for the superconductivity. Allowing for a 50% error in the fitted values of λ and taking a rather small value of $\mu^* = 0.08$ for the Coulomb repulsion, the model of JD implies a maximum for Rb_3C_{60} of T_c=7.1 K with $\alpha = 0.45$.

This analysis is beset by uncertainties in the plasma frequency, which enters the calculation squared. However, this uncertainty actually turns to our advantage. A slight modification of the value of plasma frequency used will reconcile the two methods of determining the coupling strength. Using the infrared reflectivity result of $\omega_p = 1.56$ eV for Rb_3C_{60} [203] instead of the theoretical value of 1.1 eV increases the fitted values of λ in the present by a factor of $\left(\frac{1.56}{1.1}\right)^2 = 2$, bringing these results into closer agreement with the original analysis in Tables 10.1 and 10.2. The original analysis in terms of critical field data experiences a concomitant modification, maintaining the same values of λ (since the scattering time has not changed but yielding values of the resistivity smaller by the same factor of two. From this point of view, there are certain robust conclusions. Only the values of λ for the model of Schluter et al. are in the correct range to account for the observed T_c. The other models yield λ at variance with experimental results for T_c and α. Specifically, using the coupling function of Schluter et al. and solving the Eliashberg equations with $\mu^* = 0.18$ yields T_c=17.6 K, α=0.32 for K_3C_{60} and T_c=32.8 K, α=0.34 for Rb_3C_{60}, in good agreement with the experimental results of T_c=19.2 K, α=0.3±0.06[225] for K_3C_{60} and T_c= 30.8 K[180], α=0.37±0.05[224] for Rb_3C_{60}.

The present state of experimental and theoretical knowledge precludes a definitive statement regarding the exact values of the plasma frequency, the intrinsic resistivity and the electron-phonon coupling in the alkali-doped fullerenes. However, a detailed analysis

Table 10.3: Best-fit values of λ to the temperature dependent resistivity for various theoretical models of the electron-phonon coupling. The absolute values of λ are determined by using the theoretical values for the plasma frequency[147, 200] and fluctuation conductivity results for the resistivity[194]. The expressions λ_{High} refer to coupling to the high frequency on-ball modes whereas λ_{Low} refers to an additional low frequency mode at 150 K. A correction for thermal expansion has been applied.

Model	λ_{High}^{K}	λ_{Low}^{K}	λ_{High}^{Rb}	λ_{Low}^{Rb}
SLNB	0.58	0.08	0.82	0.08
VZR	1.50	0.07	2.15	0.07
JD	0.27	<0.02	0.34	0.00

of several sources of information strongly supports a model with moderate electron-phonon coupling to phonons with an average frequency of ≈ 1000 K.

10.5 Resistivity Saturation

The family of alkali-doped fullerenes contains the highest-T_c isotropic three dimensional superconductors presently known. Several experimental results point towards electron-phonon mediated superconductivity in these materials. In particular, the carbon isotope effect is substantial[225, 224] and both Raman measurements[167] and inelastic neutron scattering[155] yield phonon linewidths consistent with moderately strong electron-phonon coupling. Theoretical calculations of the electron-phonon coupling lend additional credence to this model[175, 173, 174, 226]. On the other hand, the alkali-doped fullerenes have several characteristics which suggest that the detailed preconditions of the

standard BCS theory may not be fulfilled. The characteristic phonon energy scale ($\approx$ 0.1 eV) approaches the energy scale of intraband electronic dynamics ($\approx$ 0.4 eV) Calculations of metallic screening in the doped material suggest that the Coulomb interaction is efficiently screened, but with the possibility of a significant long-range Hubbard U[219]. Measurements of normal-state transport properties provide a means to evaluate the degree to which these materials can be described within Bloch-Boltzmann transport theory, a treatment which assumes a separation of vibrational and electronic timescales and a single-particle view of electron dynamics. In particular, Bloch-Boltzmann theory predicts its own demise: a "run-of-the-mill" conductor will exhibit resistivity saturation as the mean free path approaches the interatomic spacing. The low temperature mean free path in the alkali-doped fullerenes is fairly short, suggesting that these materials are plausible candidates for the observation of resistivity saturation at high temperatures. However, if the alkali-doped fullerenes are dominated by correlative effects they will not necessarily be hostage to high-temperature resistivity saturation.

Previous experimental work has been interpreted as evidencing an absence of saturation for temperatures up to 550 K in K_3C_{60} and Rb_3C_{60} thin films[195]. These measurements were taken to support the possibility of novel transport mechanisms such as resonant tunnelling. However, as pointed out by these authors, an accurate evaluation of the high temperature resistivity in these materials requires a detailed consideration of the temperature dependent density of states, an effect which could mask the signature of resistivity saturation.

We report high temperature pulsed heating resistivity measurements up to 800 K on K- and Rb- doped C_{60} single crystals. The data are analyzed within the parallel-resistor extension to Bloch-Boltzmann transport theory[227] with a temperature-dependent density of states to obtain a saturation mean free path of $l_{sat} \approx 1 \pm 0.4$Å for Rb_3C_{60}, on the order of the carbon-carbon bond length of 1.4 Å. K_3C_{60} does not show obvious signs of saturation up to 800 K, suggesting an upper bound of $l_{sat} < 1.5$Å. Both results are consistent

with the expectations of resistivity saturation within Bloch-Boltzmann transport theory. These results indicate that the electronic states relevant to high-temperature transport have a characteristic length scale significantly smaller than the fcc lattice constant.

Single crystals of C_{60} were doped with Rb and K in the standard fashion[192], with iterative dope/anneal stages proceeding until a final resistivity minimum is reached. Since the metallic phase A_3C_{60} (A = K, Rb) is not the saturation phase of the intercalation process, it is useful to ask if a uniform A_3C_{60} phase can be easily obtained in a bulk sample. In this context we note that direct resistivity measurements on bulk samples yield results which are often 2-3× higher than estimates based on various indirect, theoretical, or optical probes[194, 177, 216, 228, 151, 207]. Doping of bulk samples most likely begins with the formation of islands of doped material in pristine C_{60}. The finite vacancy energy of A_3C_{60} guarantees that the equilibrium dopant concentration at moderate temperature and dopant level will be somewhat substochiometric. In addition, at sufficiently high doping rate it may become possible to nucleate A_4C_{60} or A_6C_{60} inside the doped portions of the sample before the substochiometric A_3C_{60} phase diffuses through the crystal. A heterogeneous doping profile would account for the discrepancy between direct and indirect measurements of the DC resistivity in A_3C_{60}. We emphasize that the *functional form* of the temperature dependent resistivity is independent of detailed doping profile. Modulo differences in effective geometry, the temperature dependent resistivity of different samples of both K_3C_{60} and Rb_3C_{60} is precisely reproducible.

A major concern of high-temperature resistivity measurements in these materials is the possibility of thermally-driven rearrangement of the intercalant species, in particular deintercalation and/or formation of A_4C_{60}, A_6C_{60}, or solid solution A_xC_{60} phases at high temperature. To minimize these effects, a pulsed heating apparatus was used which can heat the sample from room temperature to 800 K on a timescale of a few seconds. Details of the experimental techniques can be found in reference [229].

Fig. 10.10 shows the results of several runs of pulsed heating on single samples of both
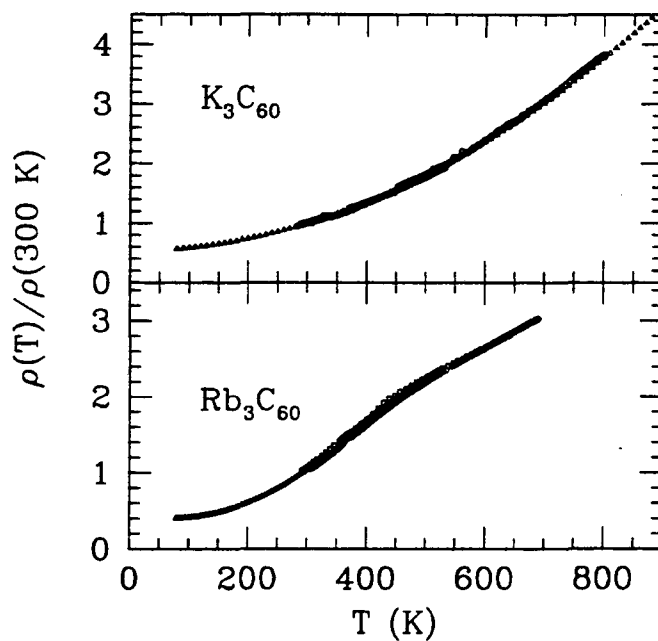
Figure 10.10: High temperature resistivity of K_3C_{60} and Rb_3C_{60}. Different symbols represent sequential pulsed heating runs. Data for $T < 300$ K were obtained using conventional slow-cooling techniques.

K_3C_{60} and Rb_3C_{60}. The dashed lines below 300 K are dc resistivity data for the same samples obtained by the more conventional slow-cooling technique. The high-temperature data in Fig. 10.10 are reproducible over several pulsed heatings excursions, indicating minimal deintercalation or irreversible intercalant rearrangement. Similar results were obtained for different crystals of K_3C_{60} and Rb_3C_{60}. We note that freshly doped samples of K_3C_{60} often exhibit an interesting resistive anomaly near 380 K consisting of small, smooth hysteretic resistive step of order 10%, possibly accompanied by a very slight change in slope. This anomaly is also observed in samples that are heated in a non-pulsed manner. The origin of this anomaly is at present unclear, but it may reflect a change in effective geometry of the conducting portion of the sample or a change in lattice constant in the A_3C_{60} portion of the sample, either a stress-induced expansion due to a structural transition in a minority phase or an expansion local to the A_3C_{60} phase due to an orientational order/disorder transition in the doped material. In any case, this anomaly is "annealed out" and disappears after one or two high temperature cycles of the sample, yielding the smooth and reproducible $\rho(T)$ behavior shown in Fig. 10.10.

Turning to data analysis, we begin with a discussion of the theoretical treatment of resistivity saturation. Bloch-Boltzmann transport theory fails as the electronic mean free path approaches the lattice spacing. One can account for this effect by imposing a phenomenological minimum electron scattering time τ_{sat}, which corresponds to a length scale, $\ell_{sat} = \tau_{sat}v_f$, on the order of the interatomic spacing. This minimal time acts as an offset to the Poisson distribution of electron scattering events, yielding a parallel resistor model of resistivity saturation,[227, 230]

$$\frac{1}{\rho} = \frac{1}{\rho_{BB}} + \frac{1}{\rho_{sat}}. \tag{10.6}$$

At all temperatures, the finite offset τ_{sat} yields a resistivity lower than that expected from conventional transport theory. At high temperatures, the resistivity eventually saturates at the value ρ_{sat}. The Bloch-Boltzmann resistivity ρ_{BB} is composed of two parts, a residual

resistivity ρ_0 and an electron-phonon resistivity ρ_{ep}, which are assumed to contribute additively in accord with Mattheisen's rule. The electron-phonon contribution is modelled within the Ziman resistivity formula[222] for three different models of the on-ball electron-phonon coupling with different weights of contributions from the range of on-ball phonon frequencies. These models yield average phonon frequencies of $\bar{\omega} \approx 500K[175]$, $\bar{\omega} \approx 1200K[173]$, $\bar{\omega} \approx 2000K[174]$. Each model is augmented by the addition of variable coupling to a low-frequency mode set at $\omega = 150K$. This low frequency mode is a generic representation of possible contributions from alkali atom optic modes, librational modes, or interball translational modes. In all cases, the coupling to this mode turns out to be small, and the important features of the calculated resistivity are not sensitive to variations in the frequency of this mode from 50 to 200 K.

At first sight one might think that the presence of resistivity saturation could simply be read off of a graph of resistivity versus temperature. However, the special properties of the alkali-doped fullerenes necessitate a detailed theoretical treatment. In particular, the characteristic phonon frequency is quite high; within the experimentally accessible temperature range the system may never reach the high-T limit in which the resistivity is strictly proportional to the temperature. More importantly, the density of states at the Fermi level N(0) for the alkali-doped fullerenes is a sensitive function of the lattice constant which varies considerably due to thermal expansion. The electron-phonon component of the resistivity is expected to be proportional to the density of states squared, one factor of N(0) from ω_p^2, another from the scattering time in the formula $\rho_{ep} = \frac{4\pi}{\omega_p^2 \tau}$ where ω_p is the plasma frequency. Alternatively, the density of states dependence can be recast as a dependence on Fermi velocity wherein the conductivity is proportional to the Fermi velocity squared. Taking $v_f \sim \frac{1}{N(0)}$, we again obtain a resistivity proportional to density of states squared. An increasing N(0) as a function of T will contribute positive curvature to $\rho(T)$, obscuring the signature of saturation. The temperature dependence of the residual resistivity is less clear. Theoretically, one expects a density of states dependence

to the residual resistivity if the residual scattering mechanism is slaved to a microscopic time scale or energy scale, and a density of states-independent residual resistivity if the mechanism is slaved to a microscopic length scale. Experimentally, the residual resistivity of Rb_3C_{60} shows a significant pressure dependence[220]. In addition, several sources of information[195, 194, 177, 216] indicate that the residual resistivity in K_3C_{60} is roughly $\frac{1}{2}$ of the residual resistivity of Rb_3C_{60}, a difference which could be attributed to the difference in density of states between these two materials. In the present analysis we assume that the residual resistivity scales as the density of states squared. Should this assumption be in error, the effect upon the final results should be small since the low temperature residual resistivity is a small fraction of the total resistivity at high temperatures.

We obtain the temperature dependent density of states by combining the density of states as a function of lattice constant from a LDA band-structure calculation[172] with the experimental coefficient of thermal expansion to yield the density of states as a function of temperature. The result is in reasonably good agreement with NMR measurements of the temperature dependence of $\sqrt{\frac{1}{T_1 T}}$[231]. The thermal expansion for both K_3C_{60}[232] and Rb_3C_{60}[233] has been measured from 5 K to 300 K. Above 100 K the lattice constant is accurately modelled with a linear temperature dependence, the form chosen for extrapolation to 800 K. The density of states has been calculated for lattice constants from 14.0 Å to 14.435 Å. Treatment of the Rb_3C_{60} experiment requires extrapolation beyond the range of calculated values. We compared two functional forms for this extrapolation, a least squares cubic polynomial fit, and a fit to the form $N(a)=N_o\,(a-\bar{a})^\eta$, with N_o, $\bar{a}$ and η as fitting parameters. Both forms yield comparable fits with similar extrapolations. The variations in extrapolation are taken into account in the estimation of uncertainties.

We normalize the experimentally determined resistivity curves by appeal to an analysis of upper critical field data which yields values of the T=0 scattering time[177, 216]. Combining these results with theoretical values for the plasma frequencies of K_3C_{60} and Rb_3C_{60} (1.2 and 1.11 eV respectively)[147, 200] yields values of the T=0 resistivity of
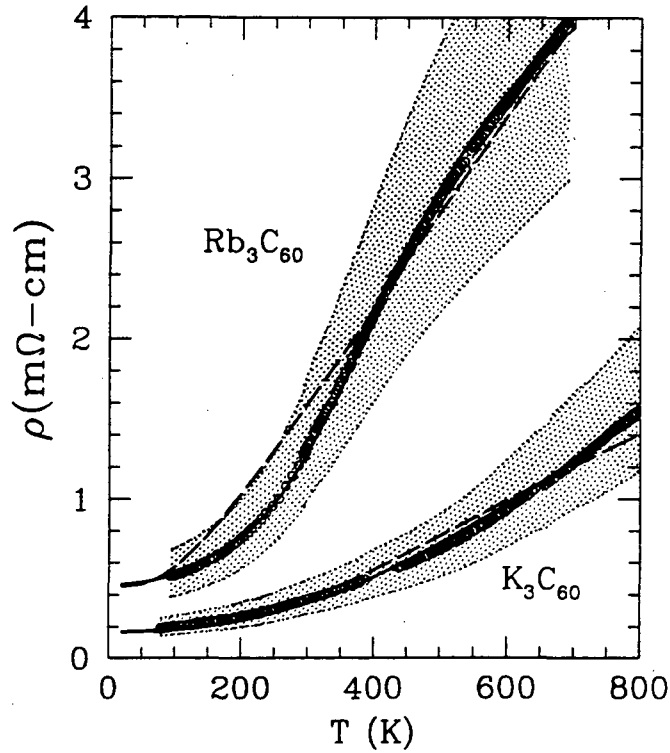
Figure 10.11: Normalized resistivity versus temperature for K_3C_{60} (lower curve) and Rb_3C_{60} (upper curve). Shaded areas indicate indicate uncertainties in resistivity normalization. Solid and dashed curves are theoretical fits. For Rb_3C_{60} the dashed line fit uses the electron-phonon coupling spectrum from Jishi et al. ($\bar{\omega} \approx 500$ K), whereas the solid line fit uses the spectrum of Varma et al. ($\bar{\omega} \approx 2000K$). Both models include a temperature-dependent density of states. The fits to the K_3C_{60} data use the coupling spectrum from Schluter et al. ($\bar{\omega} \approx 1200$ K). The solid fit includes a temperature-dependent density of states whereas the dashed fit does not.

$0.18\pm0.06m\Omega$-cm and $0.57\pm0.21m\Omega$-cm respectively. Normalizing the data of Fig. 10.10 to these values yields the absolute resistivity curves in Fig. 10.11 (open circles). The shaded areas indicate the range of uncertainty in the normalization. Representative theoretical fitting curves are included in this figure.

Two ancillary points are immediately evident from the theoretical analysis. First, a temperature-dependent density of states is necessary to obtain a satisfactory fit to the full range of experimental data for K_3C_{60}. The continuous (dashed) curve following the K_3C_{60} data in Fig. 10.11 shows the best fit with (without) a temperature-dependent density of states for the model with $\bar{\omega} \approx 1200K$. The fit at constant $N(0)$ is substantially worse. Secondly, the fits using the coupling spectrum with lowest average frequency ($\bar{\omega}$=500 K) are quite poor, as evidenced by the dashed fit to the Rb_3C_{60} data in Fig. 10.11 . This result suggests that the relative contributions of on-ball phonons to the electron-phonon coupling is centered at moderate to high frequencies. Finally, we note that the values of the total electron-phonon coupling λ derived from these analyses are in accord with the range expected for a BCS superconductor[157].

The high-temperature resistivity of Rb_3C_{60} is in reasonably good agreement with the parallel resistor model of saturation. The model with $\bar{\omega} \approx 1200K$ yields $\rho_{sat} = 5.1\pm1.9m\Omega$-cm while the model with $\bar{\omega} \approx 2000K$ yields $\rho_{sat} = 6.3 \pm 2.4m\Omega$-cm (this fit is shown in Fig. 10.11 as the solid curve following the Rb_3C_{60} data). The saturation length can be derived from these values by appeal to theoretical values for the plasma frequency and Fermi velocity (1.8×10^7 cm/sec for K_3C_{60} and 1.6×10^7 cm/sec for Rb_3C_{60}) which are obtained from LDA electronic structure calculations in the orientationally ordered structure[147, 200]. The results for Rb_3C_{60} are $\ell_{sat} = 0.9 \pm 0.4$Å for $\bar{\omega} \approx 1200$ K and $\ell_{sat} = 1.0 \pm 0.5$Å for $\bar{\omega} \approx 2000$ K.

The K-doped sample does not show obvious signs of saturation. The theoretical analysis yields a lower bound on the magnitude of the saturation resistivity. The solid curve following the K_3C_{60} data in Fig. 10.11 is the best fit to the model with $\bar{\omega} \approx 1200$ K

and $\rho_{sat} = 6.4 \pm 2.0$ mΩ-cm. Smaller values of ρ_{sat} yield unsatisfactory fits to the data. The model with $\bar{\omega} \approx 2000$ K yields an analogous bound of $\rho_{sat} > 4.8 \pm 1.5$ mΩ-cm. Taking 4.8 ± 1.5mΩ-cm as a lower bound on ρ_{sat} yields a bound on the saturation length of $\ell_{sat} < 1.1 \pm 0.4$Å. Like the situation for Rb$_3$C$_{60}$, this value is consistent with the C-C bond length. A comparison of the normalized resistivity data for K$_3$C$_{60}$ and Rb$_3$C$_{60}$ in Fig. 10.11 clearly shows that even at the highest temperatures reported ($\sim$800 K) the K$_3$C$_{60}$ sample has not yet reached a resistivity regime similar to that in which the Rb$_3$C$_{60}$ sample begins to exhibit resistivity saturation.

We note two experimental uncertainties which could have significant impact of the conclusions of this work. First, the absolute value of the resistivity is somewhat in question. We note that estimates of the resistivity from fluctuation measurements[194] are smaller than the values used in the present analysis. Using these fluctuation-derived values would yield saturation lengths 2× larger for Rb$_3$C$_{60}$ and 1.5× larger for K$_3$C$_{60}$. On the other hand, if one believes that the direct measurements of the resistivity represent intrinsic properties, one obtains saturation lengths roughly 2-3× shorter than derived in this work. These values, substantially smaller than the carbon-carbon bond length, would be at odds with the parallel resistor extension to Bloch-Boltzmann transport theory. We believe that the direct measurements of the absolute resistivity are least accurate due to uncertainties in the effective volume of the sample. Second, we note that an experimental measurement of the low-temperature *constant volume* resistivity[220] suggests that the spurious positive curvature introduced by constant pressure measurement is substantially greater than that predicted by a temperature dependent density of states, indicating that the signature of saturation adjusted to constant sample volume may be stronger than that resulting from the present analysis, yielding a longer ℓ_{sat}. Detailed consideration of this point awaits experimental data on the constant volume resistivity at higher temperatures. Finally, we remark that inclusion of the temperature dependence of the low frequency interball modes would yield slightly ($\sim$10%) longer saturation mean free paths without substantively

altering the conclusions of the analysis.

In passing we note several additional effects which could contribute anomalous temperature dependence to $\rho(T)$ at a 5-10% level. The low-frequency librational modes are strongly temperature dependent. The interball translational modes are expected to also be strongly temperature dependent. In addition to a large Gruneisen effect, the electron-phonon coupling to these modes should be proportional to the squared derivative of the bandwidth with respect to the lattice constant,[157] a derivative which varies significantly over the temperature range of interest. The instantaneous distribution of local effective lattice constants in a macroscopic sample of A_3C_{60} will show thermal variation on a length scale of a lattice constant, causing the electrons to see an effective density of states slightly different from the average value. These effects are estimated to effect the results for saturation mean free path at the 5-10% level or less.

We note that the strong temperature dependence to the density of states will interfere with the backwards extrapolation of the high temperature resistivity to $\rho_{BB} = 0$ at T=0. In the present work, a backwards linear extrapolation of the Rb_3C_{60} data does in fact intersect the origin. However, this result should be regarded as fortuitous in light of the temperature dependent density of states. Previous backwards extrapolations (at lower temperatures)[195] which fall below the (ρ_{BB}, T) origin should not be taken as *prima facie* evidence of a novel transport mechanism.

The present results indicate that the single particle states relevant to transport at high temperature have a characteristic length scale much smaller than the fcc lattice constant of roughly 14 Å. Although calculations for the orientationally disordered A_3C_{60} lattice[228] suggest that the extended-state description of electron dynamics is applicable at T=0, the present work indicates that the character of the appropriate electronic states changes significantly from low to high temperatures.

Chapter 11

Hall Effect

The alkali-doped C_{60} superconductors[169] compose a family of uniquely tunable binary superconductors with high transition temperatures. Variations in lattice constant yield variations in T_c over an order of magnitude from ~ 3 K to ~ 30 K[154]. The electronic structure[150, 234] and transport properties[151, 228, 229] of these materials are strongly affected by the orientational disorder of the C_{60} constituents, raising questions as to the most appropriate picture for the electronic states. Measurements of the Hall effect should provide information as to the nature of the relevant electronic structure. Unfortunately, the only existing Hall effect measurements were performed on a granular K-doped C_{60} film[235] with a non-metallic resistivity and zero-dimensional fluctuation conductivity near T_c. Since Hall effect measurements are known to be sensitive to sample granularity[236], experiments on single crystal samples are necessary to obtain accurate information on electronic and transport processes.

We present the first measurements of the Hall effect in K and Rb-doped single crystal C_{60} samples. The temperature dependence of the Hall coefficients of K_3C_{60} and Rb_3C_{60} from the superconducting transition to room temperature can be described by a universal function of lattice constant. The results are interpreted within a conventional band picture with significant disorder broadening of electronic states near the Fermi level and a lattice constant-dependent density of states. In the temperature range of these measurements the Fermi surface is strongly modified by scattering processes on a length scale on the order of the inter-ball distance.

Thin platelike C_{60} single crystals of typical size $500 \times 200 \times 30\mu m^3$ with shiny facets were doped with K or Rb according to standard techniques[192]. Prior to doping, eight
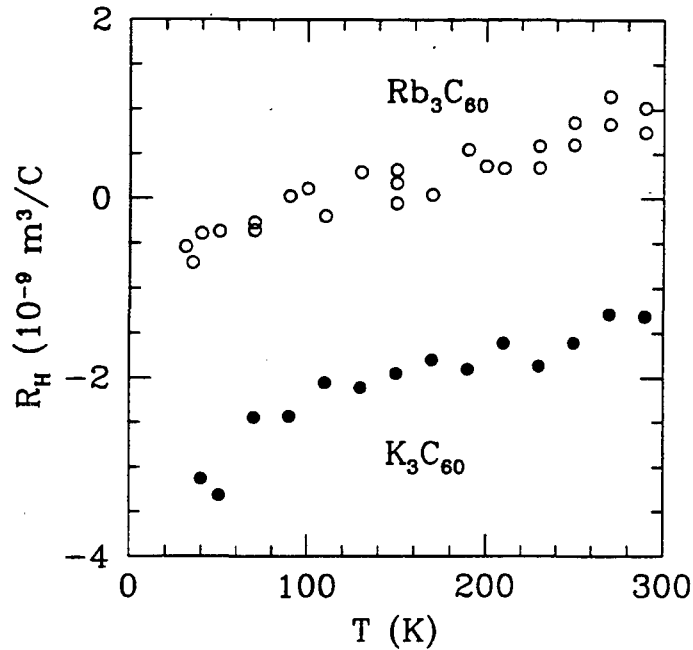
Figure 11.1: Temperature-dependent Hall coefficient of the optimally doped K_3C_{60} and Rb_3C_{60} samples.

gold wires were bonded to the edges of the crystal. The iterative dope/anneal process was guided by *in situ* monitoring of the two and four probe resistance. The Hall effect was determined applying an external magnetic field of up to 8 Tesla perpendicular to the largest crystal face and passing an AC current of $\sim$10 mA at 37 Hz through the sample. A current balance technique[237] was used to zero the Hall voltage at zero applied magnetic field. Both positive and negative magnetic field sweeps were used throughout to eliminate low frequency drift effects.

Fig. 11.1 shows the temperature-dependent Hall coefficient R_H from just above the superconducting transition to 300 K for optimally doped K_3C_{60} and Rb_3C_{60} samples. R_H for K_3C_{60} is negative and linearly increasing with increasing temperature with a slope
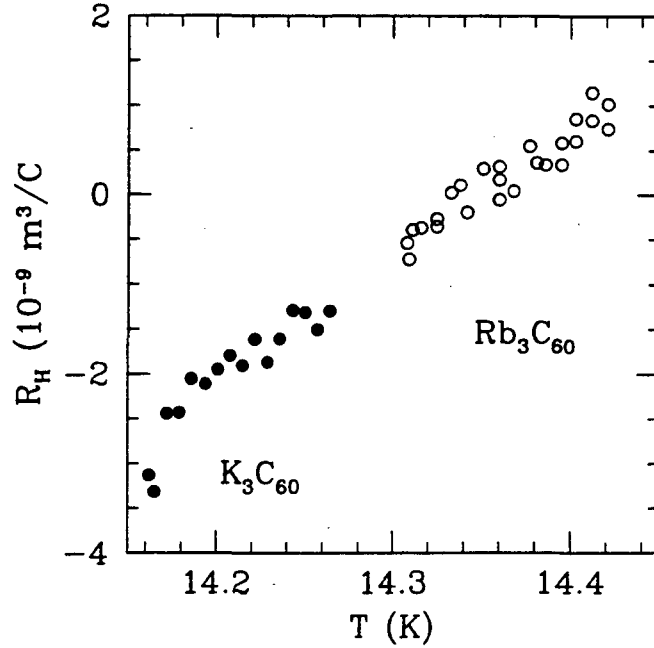
Figure 11.2: Hall coefficient as a function of lattice constant for the optimally doped K_3C_{60} and Rb_3C_{60} samples.

of $0.0055 \times 10^{-9} \frac{M^3}{CK}$. The room temperature value of $-1.4 \times 10^{-9} \frac{M^3}{C}$ coincides with the free electron value for three electrons per C_{60}. We emphasize, however, that a direct comparison with the free electron result is of limited utility in a system with a complex Fermi surface. The Hall coefficient for Rb_3C_{60}, also linearly temperature-dependent with similar slope, is displaced upwards from that of K_3C_{60} and has a zero crossing at T~120 K.

We characterized the possible effects of variations in effective sample geometry by systematically measuring the doping-dependence of ρ and R_H. The functional form of $\rho(T)$ is doping independent, indicating that neither the intrinsic residual resistivity nor the intrinsic temperature-dependent resistivity is doping-dependent[238]. Fig. 11.3 shows the Hall

mobility $\mu_H = \frac{R_H}{\rho}$ for three K-doped samples which have room temperature resistivities in the ratio 1:2:3, a ratio consonant with substantial differences in doping between the samples. As shown in Fig. 11.3, μ_H is doping invariant, suggesting that the phase boundaries inside of the thin-plate samples are parallel to the major faces, a geometry in which the functional forms of $\rho(T)$ and $R_H(T)$ are intrinsic to the A_3C_{60} phase[239]. In addition, the ratio of extrapolated T=0 resistivities for the optimally doped Rb_3C_{60} and K_3C_{60} samples was $\frac{\rho(Rb_3C_{60})}{\rho(K_3C_{60})} \approx 1.6$, (with $\rho(K_3C_{60}) = 1.0 m\Omega$-cm), a value consistent with the best estimates of the ratio of intrinsic resistivities for these two compounds[195, 194, 177, 216] and indicative of similar effective geometries for our optimally doped samples.

Previous work demonstrates a strong influence of thermal expansion upon the form of $\rho(T)$ in Rb_3C_{60}[220]. This result suggests that lattice thermal expansion should be taken into account in a discussion of $R_H(T)$. The lattice thermal expansion of A_3C_{60} in the temperature range of interest can be adequately expressed as $a(T) = a_0 + bT$, where b is $3.52 \times 10^{-4} \text{\AA } K^{-1}$ for K_3C_{60}[240] and $4.40 \times 10^{-4} \text{\AA } K^{-1}$ for Rb_3C_{60}[241]. Using these results, we plot R_H as a function of lattice constant in Fig. 11.2. We obtain a striking relation- the difference in R_H between K_3C_{60} and Rb_3C_{60} samples at a given temperature can be ascribed purely to the difference in the lattice constant between the two materials! This result suggests that the variation in R_H with temperature for a given sample can also be attributed purely to changes in lattice constant. Apparently, R_H *at constant volume is temperature-independent for both materials*. A simple linear fit yields a lattice constant dependence of $R_H = [-2.8 + 13.9(a - 14.15)] \times \left(10^{-9}\frac{M^3}{C}\right)$ where a is measured in angstroms.

Prior calculations of the Hall coefficient using the Jones-Zener solution[242] of the Boltzmann equation in an orientationally ordered system at zero temperature with isotropic scattering time yield $R_H = 7 \times 10^{-9}\frac{M^3}{C}$ for both K_3C_{60} and Rb_3C_{60}[243]. The result, which is weakly pressure-dependent, arises from a complex weighted average over a Fermi surface composed of a hole-like pocket and a pair of open sheets with regions of
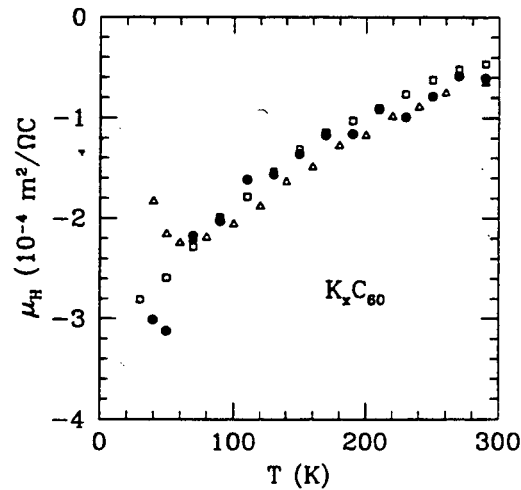
Figure 11.3: Temperature dependence of the apparent Hall mobility of three $K_x C_{60}$ samples with different doping levels. The resistivity ratios at 300 K are $\triangle : \square : \bullet = 3 : 2 : 1$.

positive and negative curvature. These results are at variance with the present experiments, wherein the Hall coefficient is much smaller in absolute magnitude and negative over a broad temperature range. In addition, the universal dependence of R_H on lattice constant suggests a pressure dependence much stronger than that calculated. Since the Hall coefficient is sensitive to Fermi surface topology, it is plausible that the discrepancy between theory and experiment is due to disorder-induced modification of the Fermi surface which is not taken into account in the orientationally ordered calculation. Although other etiologies could be envisioned (nonadiabatic effects, electron-electron correlation), the primary electronic feature determining the character of the electronic states appears to be the strong orientational disorder.

The common source of a temperature dependent Hall coefficient is a temperature dependent anisotropy in the scattering time at temperatures below the Debye temperature. Judging from experimental and theoretical indications of moderate total electron-phonon

coupling[173, 174, 175, 157, 176] and small electron-alkali-phonon coupling[180], the primary contribution to the electron-phonon scattering time can plausibly be attributed to high frequency on-ball optical phonons. The near-Einstein nature of C_{60} optical phonons and the strong electronic disorder suggest that any purely phonon anisotropy is weak and insensitive to temperature. Although the interball vibrational modes are expected to show significant dispersion, their frequencies are too low ($\sim$100 K) to explain the temperature dependence in R_H observed up to 300 K. In addition, the measured universal dependence on lattice constant argues strongly (if somewhat circularly) against a significant temperature-dependent phonon contribution to R_H, contributions which would not produce scaling behavior between materials. Instead, we must seek an explanation invoking a mechanism which itself shows universal scaling. In particular, the combined influence of orientational disorder and universal scaling of the density of states.

We begin our discussion of a model for the influence of disorder on R_H by introducing the appealing theoretical construct of the scattering length surface[244]. In this treatment, the Hall conductivity σ_{xyz} of a two dimensional system is identified with the number of flux quanta that thread a surface constructed by tracing the circuit of the vector scattering path length $\vec{\ell} = \vec{v_k}\tau_k$ as $\vec{k}$ circumscribes the Fermi surface (the three dimensional case is treated as an integral over these two dimensional constructs). The Hall coefficient R_H is obtained from the ratio $R_H = \frac{\sigma_{xyz}}{\sigma^2}$. For a single-sheet Fermi surface with isotropic scattering, the resulting scattering path locus is simply a circle (sphere in 3D) which yields the free electron result of $R_H = -\frac{1}{nec}$. More complex Fermi surfaces with anisotropic scattering times yield additional loops in the scattering length locus which contribute in accord with the sign of circulation of the scattering length vector about these regions.

Calculations using a tight-binding disordered supercell, a cluster-Bethe lattice model and a disorder-smeared virtual crystal[228] all yield a Fermi surface for the disordered system composed of pairs of parallel sheets in the cartesian directions with square electron-like regions centered at Γ, X and K (the region around K is severely smeared). The

electron-like nature of the disordered Fermi surface is consistent with the predominately negative Hall coefficient. For the purposes of gaining a qualitative understanding of the Hall effect, we conceptually model the disorder by considering large supercells with the disorder incorporated into the unit cell. Since this model system has perfect order, the resulting Fermi surface is well-defined and unsmeared, albeit quite complex due to the very large unit cell. Qualitatively, this Fermi surface will mimic the cluster-Bethe result of a smeared quasi-Fermi surface, but instead of true smearing the Fermi surface will have fine detail over a width consistent with the zero-temperature mean free path. This fine detail will consist of both numerous small electron-like and hole-like pockets and the complex local curvature of the larger sections of Fermi surface, sections which may either encompass the Γ and X points or bridge across the zones in a multiple zone scheme.

The numerous small hole-like and electron-like pockets will contribute oppositely to the integral determining R_H, presumably yielding a small net contribution to the Hall coefficient. Anisotropy in the scattering length along the large-scale sections of the Fermi surface will lead to the formation of secondary loops associated with high-curvature regions of these extended portions of the Fermi surface. Should the secondary loops be equally positive and negative, they will on average cancel each other out. However, the increase in Fermi velocity with distance from Γ and X should produce secondary loop contributions of generally opposite sign from the main contribution (similar to the generic situation of parabolic bands[244]). The greater the k-space extent of the disorder broadening, the larger the contributions from the secondary loops.

The variation in R_H with lattice constant can be qualitatively modelled by assuming that the relative k-space extent of the disorder broadening of the Fermi surface increases with increasing lattice constant. As the relative k-space extent of the disorder increases, the secondary loops sample regions of smaller Fermi velocity near the Γ and X points, leading to larger secondary loops and an increasing Hall coefficient. The question remains how an increase in lattice constant could yield an increase in the disorder broadening at

the Fermi level. If the disorder potential has a characteristic energy scale which is to
first order independent of the lattice constant, then the k-space extent of the disorder
broadening will be an increasing function of density of states and hence an increasing
function of lattice constant. The differences in residual resistivity between K_3C_{60} and
Rb_3C_{60}[195, 194, 177, 216] are consistent with greater density of states in Rb_3C_{60} and
hence greater k-space extent to the disorder broadening. The universal scaling of R_H is a
natural consequence of the universal scaling of the density of states at the Fermi level as
a function of the lattice constant[172]. This argument suggests that the Hall coefficient
R_H in A_3C_{60} will increase from negative values at low disorder broadening (K_3C_{60} sample
at low T and small density of states) to positive values at larger disorder broadening
(Rb_3C_{60} sample at high T and large density of states), in accord with the experimental
result. The behavior is similar to that suggested[245] for disordered nearly free electron
metals, wherein the Hall coefficient is inversely dependent on the density of states.

To obtain rough numerical results we assume that the secondary loops do not overlap
and thereby perfectly cancel the primary loop in $\vec{\ell}$-space over an extent consonant with
the k-space extent of the disorder broadening, so that the net contribution to the Hall
coefficient will arise from a residual Fermi surface at the inner edges of the smearing
zones, a region of decreased Fermi velocity and therefore smaller contributions to R_H. In
this crude approximation the dynamics can be modelled quite simply by taking a smearing
length perpendicular to the Fermi surface equal to the inverse zero temperature mean free
path corresponding to a particular lattice constant and only taking contributions to R_H
from electronic states around the Γ and X points that lie entirely inside of these regions of
disorder, treating the system as if it had (for the purposes of the Hall effect) an effective
Fermi surface which lies at the *inner* (nearest Γ and X) edge of the actual disorder-
broadened Fermi surface. Using the experimental results for the T=0 mean free paths of
K_3C_{60} and Rb_3C_{60} which arise from an analysis of upper critical field data[177, 216], we

obtain a ratio of R_H between K_3C_{60} and Rb_3C_{60} at T=0 of $\frac{R_H(K_3C_{60})}{R_H(Rb_3C_{60})} \sim 5$, in possibly fortuitously close agreement with the experimental result of ~ 4.5 for linear extrapolation to T=0.

Although finite phonon energies, thermal smearing and true (non-super cell) disorder will wash out the finest structure of the disordered supercell Fermi surface, the functional form of R_H is primarily determined by the Fermi surface sampling of the large-scale variation in v_f, a large-scale feature which should not be washed out by moderate smearing. Temperature-dependent thermal smearing will contribute a nonuniversal term to the volume dependence of the Hall coefficient. However, taking a mean free path of 12Å for Rb_3C_{60} at T=0[216] and $v_f = 1.5 \times 10^8 \frac{cm}{sec}$[216], a simple estimate for the energy scale of the disorder yields $\Delta E \approx \frac{\hbar v_f}{\ell} \approx 1400$ K, substantially larger than the temperature range of this experiment- temperature-dependent thermal smearing will make at most a minor nonuniversal contribution to R_H. Before concluding, we also note that the orientational disorder in alkali-doped C_{60} appears to be frozen in in the temperature regime of this experiment, thereby disallowing the possibility of nonuniversal contributions to R_H from temperature dependence in the nature of the orientational disorder.

Hall effect measurements on K_3C_{60} and Rb_3C_{60} single crystal samples yield R_H as a universal of lattice constant, apparently regardless of whether dilation is caused by thermal expansion or steric effects. A qualitative model incorporating lattice-constant dependent disorder broadening at the Fermi level is consistent with this universal form and accounts for the discrepancy between the experimental results and previous calculations on orientationally ordered systems. The theoretical treatment yields a simple prediction for the pressure dependence of the Hall coefficient, namely, the same universal functional dependence on volume should be evinced if the volume change is induced by pressure rather than temperature or species of alkali atom. A similar argument applies to alloys such as $Rb_xCs_{3-x}C_{60}$ or $K_xRb_{3-x}C_{60}$, materials which are expected to have temperature

dependent Hall coefficients in accord with this universal form.

Chapter 12

Isotope Effects

12.1 Carbon Isotope Effect

A crucial experiment in the development of the BCS theory of superconductivity was the observation of an isotope effect for T_c. For several metals, the isotope parameter $\alpha = -\frac{d\ln T_c}{d\ln M}$ was found to be approximately 0.5, indicating that electron-lattice effects are intimately connected with superconductivity. Values of α less than $\frac{1}{2}$ were found for transition metals and reconciled with the different frequency cutoffs for the phonon and Coulomb interactions, which yield

$$\alpha = \frac{1}{2}\left[1 - \left(\frac{\lambda^*}{\lambda^* - \mu^*}\right)^2\right], \tag{12.1}$$

wherein a finite Coulomb repulsion μ^* reduces the isotope effect exponent from the canonical value of $\frac{1}{2}$.

At this time, five measured values of α for carbon substitution in A_3C_{60} have been reported: $\alpha = 1.4 \pm 0.5$ for 33% ^{13}C replacement [246], $\alpha = 1.7 \pm 0.5$ for 60% ^{13}C replacement [247], $\alpha = 0.37 \pm 0.05$ for 75 ± 5 % ^{13}C replacement [224], $\alpha = 0.30 \pm 0.06$ for 99% ^{13}C replacement [225], and an unpublished measurement of $\alpha = 0.2 \pm 0.2$ [248]. One obvious conclusion, if these data are correct, is that lattice effects appear to be related to the superconductivity. However, the substantial scatter in results begs explanation. A comparison of samples with different microscopic isotopic profiles may provide a solution. Measurements at half ^{13}C substitution have been performed on samples in which the ^{12}C and ^{13}C were mixed on each fullerene molecule (intraball substitution) and also on samples composed of a mixture of pure ^{12}C and ^{13}C molecules (interball substitution). The interball substitution yields the larger isotope effect, $\Delta T_c = 0.9K$ versus $\Delta T_c = 0.45K$[249]. These

results suggest that the larger values of α cited above arise from heterogeneous mixtures of different flavors of fullerene molecules.

The values of α in the range of 0.3 to 0.4 are consistent with standard models of superconductivity in which α is depressed from $\frac{1}{2}$ by the Coulomb repulsion as described in Eqn. 12.1. In particular, an average phonon frequency of 1000 K yields $T_c = 29$ K and $\alpha = 0.37$ for $\lambda = 0.81$ and $\mu^* = 0.19$. Lower average frequencies require stronger coupling and larger μ^*. For example, $\omega \sim 200$ K implies $\lambda = 2.5$ and $\mu^* = 0.31$ for $\alpha \approx 0.37$.

In this context, the general question of whether μ^* can be reduced much from μ has been raised [250]. It is argued that the $\log\left(\frac{E_F}{E_D}\right)$ factor in μ^* is small and ineffective in reducing μ. In addition, $N(E_F)$ is large because of the narrow bands and this causes μ, which is proportional to $N(E_F)$, to be large. However, it is likely that since $\mu \sim \frac{(N(E_F)V)}{\varepsilon}$, where V is the Coulomb interaction and ε is the dielectric function, the $N(E_F)$ factor in ε will dominate this function and cancel the $N(E_F)$ factor in the numerator. This is characteristic of systems with large $N(E_F)$. The result would be a μ in the range of 0.15 to 0.3.

The experimental measurements of $\alpha \sim 1.5$ [246, 247] provide a greater challenge to conventional theories of superconductivity. We consider four possible explanations for an isotope effect greater than the BCS maximum of 0.5: a strong energy dependence of the electronic density of states near the Fermi level, anharmonic phonons, isotopically disordered intraball phonons and materials variability associated with the differing effective thermal histories of intraball and interball substituted samples. Electronic structure calculations place the Fermi level on the upper side of a peak in the density of states of width ~ 0.5 eV, as depicted in Fig. 8.1. Assuming an average phonon frequency less than 2000 K, a calculation within BCS theory using a Lorentzian form for the density of states [193] yields a maximum change of only ± 0.05 in the isotope effect exponent due to the energy-dependent density of states. An anharmonic phonon with positive quadratic and sixth-order contributions and a negative quartic part can increase the isotope exponent

above 0.5 [22, 102]. The effect is most pronounced at weak coupling. Unfortunately, weak coupling implies high-frequency phonons, which are unlikely to be softened by a negative quartic part. Stronger coupling to lower frequency phonons would imply stronger (and likely unphysical) anharmonicities.

These two mechanisms do not provide a natural explanation for the difference between intraball and interball isotopic substitution. In addition, neither of them is consistent with an isotope effect exponent $\alpha \sim 0.4$ upon 100% ^{13}C substitution. At intermediate isotopic substitution, the mass distribution on the C_{60} molecule is disordered[251]. The normal modes of this system will not have the exact symmetries of the isotopically pure material. Therefore, the electron-phonon coupling function $\alpha^2 F(\omega)$ will spread out as the isotopic disorder allows additional modes to couple to the electrons [252]. This effect can be crudely modelled as a broadening of the peaks in $\alpha^2 F(\omega)$ as the system becomes maximally isotopically disordered. At first sight, it may appear plausible that this broadening could influence the isotope exponent. However, within linear electron-phonon coupling the magnitude of λ is independent to isotopic disorder[252] such that isotopic disorder has no effect on α.

Finally, we consider the possibility that the anomalous isotope effect for interball substitution arises from a unique thermal history to a heterogeneously substituted molecular solid. The interball substituted material has two different flavors of fullerene molecules. As the temperature is lowered below that necessary for intercalation of alkali atoms the rotational motion of the fullerene molecules will freeze out. The heavy and light balls of the interball substituted material will freeze out at different temperatures, effectively creating an intrinsic anneal and plausibly leading to a different variety of orientational disorder compared to the more homogeneous intraball isotopically substituted material. The freezing out of rotational motion in the pristine material is accompanied by a $\sim 0.1\text{Å}$ change in lattice constant, suggesting that a difference in the character of the orientational disorder in the two varieties of doped material could produce a comparable, although likely

smaller difference in lattice constant. The interball isotope effect as measured by the group of Lieber et al.[249] is 0.45 K above that of the nonanomalous intraball material. This anomalous decrease in T_c could be accounted for by a 0.01 Å decrease in lattice constant for the intrinsically annealed interball substituted material. The size of this anomalous decrease would be sensitive to materials processing conditions, consistent with the large scatter in the experimental results for the carbon isotope effects greater than 0.5 in alkali-doped C_{60}.

12.2 Alkali Isotope Effect

Although the preponderance of evidence points towards electron-phonon mediated superconductivity in the alkali-doped fullerenes, the details of the mechanism remain controversial, with several different phonon-mediated[174, 175, 173, 160, 253, 226] models proposed. These models can be subdivided into those that rely exclusively upon on-ball molecular phonons[174, 175, 173] and those which incorporate additional modes such as librons,[226] translational modes[254] or alkali-C_{60} optic phonons[160, 253]. For any superconducting mechanism, we can write $T_c \propto M_i^{-\alpha_i}$ where M_i is mass of a given atomic constituent and α_i is the isotope shift exponent for this atomic species. Although these models generally predict a carbon isotope effect, a substantial intercalant isotope effect is expected only for models with a significant alkali-C_{60} optic phonon contribution to the pairing mechanism. An accurate measurement of the alkali atom isotope effect would therefore provide a useful constraint on the mechanism of superconductivity.

To date, isotope effect measurements on A_3C_{60} (A=K, Rb) consist of a single rubidium experiment[255] and several carbon isotope effect experiments[225, 224, 246, 247, 256]. There is uncertainty concerning the intrinsic carbon isotope effect in that a more homogeneous carbon isotopic distribution seems to yield a smaller carbon isotope effect[249]. The most complete substitution to date yields $\alpha_C = 0.3 \pm 0.05$ for K_3C_{60} and Rb_3C_{60}[249].

Susceptibility measurements on powder samples of T_c have yielded an upper limit on the rubidium isotope effect exponent of $\alpha_{Rb} < 0.2$ [255]. Comparing the T_c's of K_3C_{60} and Rb_3C_{60} *at equal lattice constant* does not constitute a valid alkali isotope experiment. Since $T_c^{Rb_3C_{60}} > T_c^{K_3C_{60}}$ at equal lattice constant[154] such an approximation would suggest an inverse isotope effect of rough magnitude $\alpha_{alkali} \approx -0.2 \pm 0.2$. However, this result is clouded by the large difference in ionic radii between K and Rb, which could yield a change in vibrational dynamics of the same magnitude as that caused by the change in alkali mass. Considering the present experimental situation, a greater certainty in α_{Rb} is desirable in order to narrow the constraints on plausible pairing mechanisms. Burk et al. have performed detailed measurements of the effect of rubidium isotope substitution on the resistive T_c in C_{60} single crystals doped with ^{85}Rb, ^{87}Rb and natural abundance rubidium, ^{na}Rb[180].

Single-crystal C_{60} samples (typically 1 mm × 1 mm × 0.1 mm) were intercalated with rubidium vapor following the technique developed by Xiang et al.[192]. Since isotopically pure elemental rubidium is not commercially available, all rubidium used in this experiment was produced by extraction of Rb metal from RbCl. Rubidium metal was extracted from isotopically enriched RbCl (RbCl @ 99.2% ^{87}Rb, 0.8% ^{85}Rb and RbCl @ 99.8% ^{85}Rb, 0.2% ^{87}Rb from US Services) and from natural abundance RbCl (RbCl @ 72.2% ^{85}Rb, 27.8% ^{87}Rb from Aldrich). The Rb metal is liberated by reaction with Ca, which yields Rb and $CaCl_2$ (see reference [180] for details). The procedure differs from that described by Ebbesen et al.[255] in that they reacted lithium with RbCl to liberate rubidium, a reaction complicated by the higher vapor pressure of Li.

Fig. 12.1 shows resistance versus temperature data of ^{85}Rb, ^{87}Rb and ^{na}Rb-intercalated samples near T_c, normalized to the resistance at T=32 K. The resistive transitions are sharp (for this material), indicating a high degree of homogeneity within a given sample. We define T_c by the maximum in the derivative of the resistance with respect to temperature. Fig. 12.2 shows $\frac{dR}{dT}$ for each sample. The data were fitted with a cubic
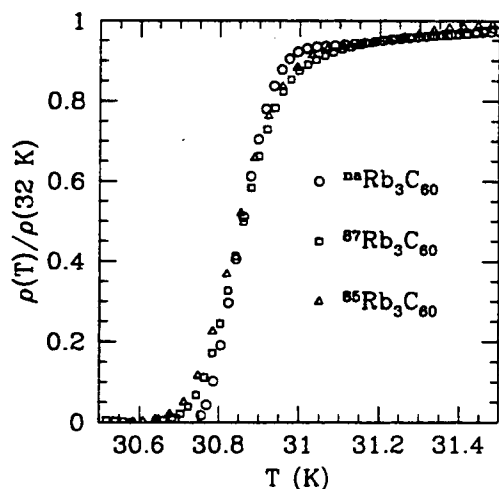
Figure 12.1: Normalized resistance versus temperature near T_c for $^{85}Rb_3C_{60}$, $^{87}Rb_3C_{60}$ and $^{na}Rb_3C_{60}$.

spline, and the maximum of the fit determines T_c (parabolic and gaussian fits yield essentially equivalent results). We measured the resistive transition several times, T_c being reproducible to within 5 mK for a given sample. We define the width of the transition as the separation between the maximum and minimum in the second derivative, yielding transition widths from 140 to 180 mK. Although the transition for $^{na}Rb_3C_{60}$ appears to be slightly narrower, the range of variation in transition width observed in natural abundance samples encompasses the results for the isotopically pure samples. We assign an uncertainty in T_c of 0.1 times the transition width. This uncertainty estimate is always greater than the reproducibility spread of T_c for a given sample; it reflects our estimate of the errors introduced by inhomogeneous broadening of the transition.

Before presenting the isotopically shifted results, we note that our measurements provide an accurate determination of T_c in Rb_3C_{60}. For $^{na}Rb_3C_{60}$ we find $T_c=30.82\pm0.09$ K, where the uncertainty reflects possible temperature sensor calibration errors. This result

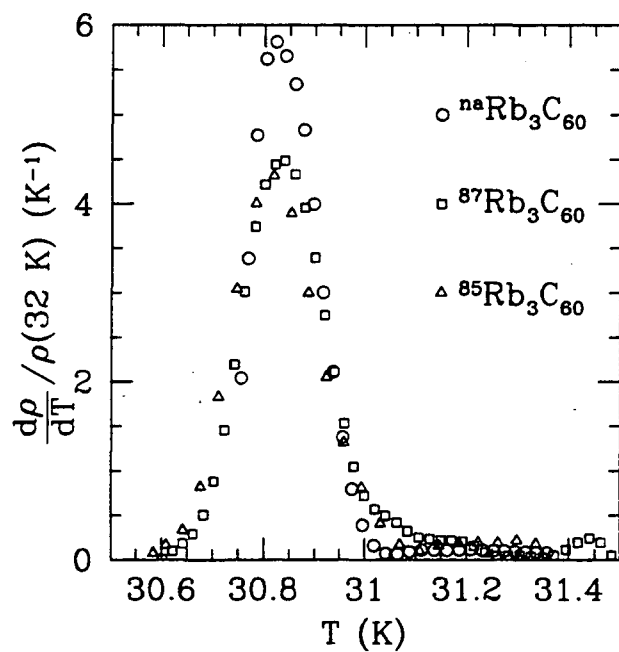Figure 12.2: Derivative with respect to temperature of normalized resistance near T_c for $^{85}Rb_3C_{60}$, $^{87}Rb_3C_{60}$ and $^{na}Rb_3C_{60}$.
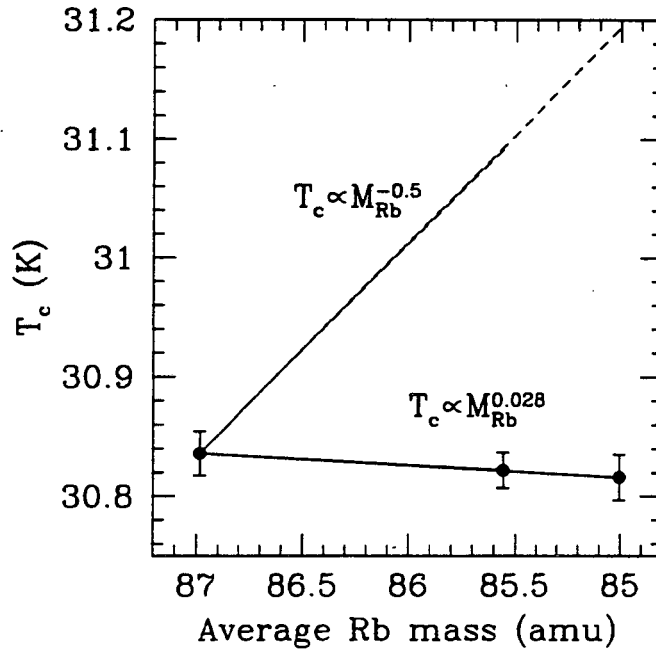
Figure 12.3: Plot of T_c versus average rubidium mass in Rb_3C_{60}. Solid line is fit of the data to $T_c \propto M_{Rb}^{0.028}$. Dashed line shows $T_c \propto M_{Rb}^{-\frac{1}{2}}$ with proportionality constant chosen so that the line passes through the $^{87}Rb_3C_{60}$ data point.

is 1-2 K higher than reported susceptibility measurements of T_c[225, 257] and about 0.6 K higher than previous resistive T_c's[194].

Fig. 12.3 displays our results for T_c measured in $^{85}Rb_3C_{60}$, $^{87}Rb_3C_{60}$ and $^{na}Rb_3C_{60}$. The data are plotted as T_c versus average rubidium mass. For comparison we plot the result for the BCS maximum value of $\alpha_{Rb} = 0.5$ normalized to the $^{87}Rb_3C_{60}$ data point. We obtain $\alpha_{Rb} = -0.028 \pm 0.036$, or equivalently $\Delta T_c = -20 \pm 26$ mK for $^{87}Rb_3C_{60} \rightarrow ^{85}Rb_3C_{60}$ (the error bars indicate the 65% confidence interval). To within our experimental uncertainty there is no rubidium isotope effect on T_c in Rb_3C_{60}.

Before discussing the implications of this result for the different pairing mechanisms, we

consider an indirect rubidium isotope effect due to a weak dependence of lattice constant on Rb mass. Both electronic[190] and phonon-mediated mechanisms are expected to exhibit an effect of lattice constant on transition temperature. To estimate this effect, we use the experimentally determined lattice constant dependence of T_c, 44 $K\text{Å}^{-1}$ [257, 154]. The isotopic shift in lattice constant can be estimated from the fractional change in crystal isotopic mass $\frac{\Delta M}{M}$, the bulk modulus B, the phonon mode energies E_i and Grüneisen constants γ_i,[258]

$$\frac{\Delta a}{a} = -\frac{2}{3}\frac{\Delta M}{M}\frac{1}{Ba^3}\sum \gamma_i E_i. \tag{12.2}$$

We treat the C_{60} molecule as a single entity, yielding four "atoms" per unit cell. The relevant phonon frequencies are the intermolecular translational and Rb-C_{60} optic modes, with frequencies in the range 50-300 K. An upper limit on the Grüneisen constants can be estimated from the pressure dependence of the bulk modulus,[154] which provides information about the hardening of the intermolecular modes with pressure. These estimates yield $\Delta a \approx 0.5 - 2.0 \times 10^{-4}$ Å for $^{87}Rb_3C_{60} \rightarrow ^{85}Rb_3C_{60}$, which translates into an increase in T_c of 2-9 mK. The entire range of this estimate falls within two standard deviations of the experimental result for α_{Rb}, indicating that the null experimental result is robust under consideration of isotopic shifts in lattice constant.

In addition to increasing the lattice constant, the substitution of ^{85}Rb for ^{87}Rb could harden the librational potential, reducing a possible librational contribution to the electron-phonon coupling. Such an effect can be estimated from the dependence of the librational mode frequency upon the size of the alkali atom[259]. The substitution of Rb for K increases the librational frequency by 8 K. The steric effects of this substitution also increase the lattice constant by 0.15Å. The $^{87}Rb \rightarrow ^{85}Rb$ substitution increases lattice constant by 0.5-2.0 $\times 10^{-4}$ Å, implying a tiny increase in librational mode frequency on the order of 10^{-2} K, a negligible effect.

A model of superconductivity in Rb_3C_{60} incorporating both on-ball carbon phonons

and Rb-C_{60} optic modes would predict a direct rubidium isotope effect due to isotopic shift in phonon frequency. The present experiment places limits on the relative contributions of rubidium modes within such a model. First we obtain a simple analytic constraint on the relative contribution of rubidium modes to the electron-phonon coupling. We assume that T_c depends on atomic mass only through the mass dependence of the average phonon frequency,

$$\alpha_i = \frac{1}{2}\frac{d\ln T_c}{d\ln \omega_{log}}\frac{d\ln \omega_{log}^{-2}}{d\ln M_i},\qquad(12.3)$$

where ω_{log} in the case of discrete phonon frequencies is defined by

$$\omega_{log} = e^{\sum_n \frac{\lambda_n}{\lambda}\ln \omega_n},\qquad(12.4)$$

with λ_n the electron-phonon coupling constant to the mode with frequency ω_n and λ is the total coupling constant. The logarithmic frequency average is the most accurate single-frequency approximation for the full spectrum of electron-phonon coupling. Using the McMillan formula for T_c[2] with a spectrum of pure carbon and Rb-C_{60} optic modes we obtain

$$\frac{\alpha_{Rb}}{\alpha_C + \alpha_{Rb}}\frac{3M_{Rb}}{M_{eff}} = \frac{\lambda_{Rb}}{\lambda},\qquad(12.5)$$

where $M_{eff} = \frac{3M_{C_{60}}M_{Rb}}{M_{C_{60}}+3M_{Rb}}$ is an estimate of the effective optic mode mass. The contribution to α_C from the weak Rb mass dependence of the carbon modes has been neglected. An upper bound on α_{Rb} yields an upper bound on the fractional contribution of λ_{Rb} to λ. Using the minimal reported value for α_C ($\alpha_C = 0.3$[225]) and two standard deviations above the measured α_{Rb} as an upper bound on α_{Rb} ($\alpha_{Rb} < 0.044$), this simple analytic model yields $\frac{\lambda_{Rb}}{\lambda} < 0.17$. Adjusting for a possible lattice-constant induced isotope shift of 2-9 mK would decrease this bound by roughly 10%.

In order to examine the effects of the detailed frequency distribution of the electron-phonon coupling we performed numerical solutions of the Eliashberg equations for various electron-phonon coupling spectra. The on-ball carbon phonons were modelled following the results of three theoretical calculations[174, 175, 173]. The frequency of the Rb-C_{60} optic
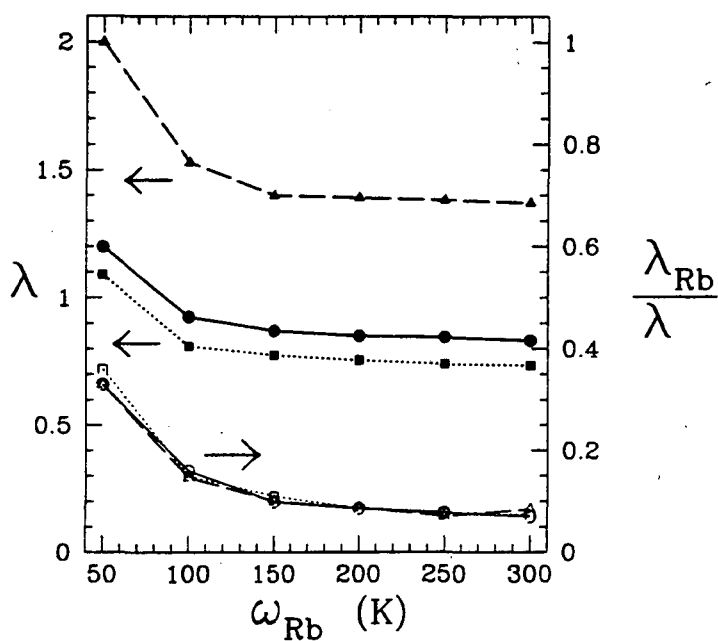
Figure 12.4: Total electron-phonon coupling strength λ (upper curves, solid symbols) and upper bound on the ratio of Rb-C_{60} optic mode coupling strength to total coupling $\frac{\lambda_{Rb}}{\lambda}$ (lower curves, open symbols) as a function of alkali mode frequency for three theoretical models of the on-ball electron-phonon coupling. The values of $\frac{\lambda_{Rb}}{\lambda}$ plotted yield $\alpha_{Rb} = 0.044$, the experimentally determined upper bound on the rubidium isotope effect. Dotted curves refer to the model of Varma et al.[174] which has the fitted value $\mu^* = 0.16$. Solid curves refer to the model of Schluter et al.[173] ($\mu^* = 0.17$). Dashed curves refer to the model of Jishi et al.[175] ($\mu^* = 0.23$).

modes was varied from 50 to 300 K. Neutron scattering results suggest mode frequencies on the order of 200 K,[260] while theoretical treatments[160, 261] place these modes in the range from 50 to 200 K. For each electron-phonon coupling spectrum the values of λ, μ^* and λ_{Rb} were varied to match experimental constraints of $\alpha_C = 0.3$, $T_c=30.8$ and $\alpha_{Rb} < 0.044$. The results are presented in Fig. 12.4. The three models yield different values of λ and μ^* while the limits on $\frac{\lambda_{Rb}}{\lambda}$ remain essentially unchanged. As the frequency of the alkali modes increases from 50 K to 300 K, the limit on $\frac{\lambda_{Rb}}{\lambda}$ decreases from 0.33 to 0.08 for all three spectra. Although the contribution of the alkali modes to T_c is at best small, the contribution of a low frequency alkali mode to λ can be substantial. In contrast to the analytic model, the ratio $\frac{\lambda_{Rb}}{\lambda}$ is only weakly dependent on α_C. Decreasing (increasing) the carbon isotope effect exponent to 0.2 (0.4) results in significantly increased (decreased) values of λ and μ^*, but the ratio $\frac{\lambda_{Rb}}{\lambda}$ decreases (increases) by only 10%. This reduced sensitivity to α_C is due to the great disparity between the alkali and carbon phonon frequencies. Modifying the electron-phonon coupling spectrum by the addition of substantial coupling to a low-frequency librational mode at 50 K[262] yields a limit on $\frac{\lambda_{Rb}}{\lambda}$ roughly 10% larger. In all cases, removal of the maximal allowed alkali-C_{60} optic mode contribution to the coupling function results in a reduction in T_c of 1-4 K, indicating that the alkali modes make at most a minor contribution to T_c.

Although the estimated uncertainty in T_c yields a value of isotope exponent consistent with $\alpha_{Rb} = 0$, the actual data points hint at a small inverse isotope effect. An inverse isotope effect is well known for hydrogen at the octahedral interstitial sites of the fcc Pd lattice;[17] it has been interpreted within the framework of anharmonic phonons[71]. Anharmonicity of the alkali vibration in the A_3C_{60} system could conceivably depress or even invert the isotopic signature of the alkali modes, weakening the limit on $\frac{\lambda_{Rb}}{\lambda}$.

In summary, precise measurements of T_c in isotopically substituted Rb_3C_{60} yield a null result for the rubidium isotope effect in Rb_3C_{60}. This result puts stringent limits on the possible contributions of alkali-C_{60} optic phonons to the superconductivity.

References

Bibliography

[1] J. Bardeen, L. N. Cooper and J. R. Schrieffer, Phys. Rev. **106**, 162 (1957); **108**, 1175 (1957).

[2] W. L. McMillan, Phys. Rev. **167**, 331 (1968).

[3] P. B. Allen and R. C. Dynes, Phys. Rev. B **12**, 905 (1975).

[4] G. M. Eliashberg, JETP **11**, 696 (1960).

[5] P. B. Allen and B. Mitrovic, *Solid State Physics*, **37** (Academic Press, 1982).

[6] A. E. Karakozov and E. G. Maksimov, Sov. Phys. JETP **47**, 358 (1978).

[7] S. G. Louie and M. L. Cohen, Solid State Comm. **22**, 1 (1977).

[8] J. C. K. Hui and P. B. Allen, J. Phys. F: Metal Phys. **4**, L42 (1974).

[9] V. Z. Kresin, Bull. Am. Phys. Soc. **32**, 796 (1987).

[10] L. C. Bourne, A. Zettl, T. W. Barbee III, and M. L. Cohen, Phys. Rev. B **36**, 3990 (1987).

[11] J. R. Hardy and J. W. Flocken, Phys. Rev. Lett. **60**, 2191 (1988).

[12] R. E. Cohen, W. E. Pickett, and H. Krakauer, Phys. Rev. Lett. **64**, 2575 (1990).

[13] S. L. Drechsler and N. M. Plakida, Phys. Stat. Sol. **144**, K113 (1987).

[14] J. J. Capponi, C. Chaillout, A. W. Hewat, P. Lejay, M. Marezio, N. Nguyen, B. Raveau, J. L. Soubeyroux, J. L. Tholence, and R. Tournier, Europhys. Lett. **3**, 1301 (1987)

[15] M. A. Beno, L. Soderholm, D. W. Capone II, D. G. Hinks, J. D. Jorgensen, J. D. Grace, I. K. Schuller, C. U. Segre, and K. Zhang, Appl. Phys. Lett. **51**, 57 (1987).

[16] A. Williams, G. H. Kwei, R. B. Von Dreele, A. C. Larson, I. D. Raistrick, and D. L. Bish, Phys. Rev. B **37**, 7960 (1988).

[17] B. Stritzker and W. Buckel, Z. für Phys. **257**, 1 (1972).

[18] V. B. Ginodman and L. N. Zherikhina, Sov. J. Low Temp. Phys. **6**, 278 (1980).

[19] R. Griessen and D. G. de Groot, Helvetica Physica Acta, **55**, 699 (1982).

[20] C. Elsässer, K. M. Ho, C. T. Chan, and M Fähnle, Phys. Rev. B **44**, 10377 (1991).

[21] V. H. Crespi, M. L. Cohen, D. R. Penn, Phys. Rev. B **43**, 12921 (1991).

[22] V. H. Crespi and M. L. Cohen, Phys. Rev. B **44**, 4712 (1991).

[23] J. M. Rowe, J. J. Rush, H. G. Smith, M. Mostoller and H. E. Flotow, Phys. Rev. Lett. **33**, 1297 (1974).

[24] J. E. Schirber, J. M. Mintz and W. Wall, Solid State Comm. **52**, 837 (1984).

[25] C. Elsässer, M. Fähnle, K. M. Ho and C. T. Chan, Physica B **172**, 217 (1991).

[26] R. C. Dynes, Solid State Comm. **10**, 615 (1972).

[27] H. Hemmes, A. Driessen, R. Griessenand M. Gupta, Phys. Rev. B **39**, 4110 (1989).

[28] J. G. Bednorz and K. A. Müller, Z. Phys. B **64**, 189 (1986).

[29] P. B. Littlewood and C. M. Varma, Phys. Rev. B **46**, 405 (1992).

[30] G. Baskaran, Z. Zou and P. W. Anderson, Solid State Comm. **88**, 853 (1993).

[31] M. Shirai, N. Suzuki and K. Motizuki, J. Phys.- Condensed Matter **2** 3553 (1990).

[32] K. Motizuki, M. Shirai, and N. Suzuki, *Proc. of Symp. on Manifestations of Electron-Phonon Interaction in Copper Oxides and Related Superconductors* (Mexico, Dec. 11-14, 1990).

[33] Q. Huang, J. F. Zasadzinski, N. Tralshawala, K. E. Gray, D. G. Hinks, J. L. Peng, and R. L.Greene, Nature **347**, 369 (1990).

[34] J. M. Valles, Jr., R. C. Dynes, A. M. Cucolo, M. Gurvitch, L. F. Schneemeyer, J. P. Garno, J. V. Waszczak, *Phys. Rev. B* **44**(1991), 11986.

[35] H. A. Mook, M. Mostoller, J. A. Harvey, N. W. Hill, B. C. Chakoumakos, and B.

C. Sales, *Phys. Rev. Lett.* **65**(1990), 2712.

[36] Y. Koyama and H. Hoshiya, *Phys. Rev. B* **39**(1989), 7336.

[37] P. B. Allen and Dierk Rainer, Nature, **349**, 396 (1991).

[38] B. Sundqvist and B. M. Andersson, Solid State Comm. **76**, 1019 (1990).

[39] M. Gurvitch and A. T. Fiory, Phys. Rev. Lett. **59**, 1337 (1987).

[40] V. H. Crespi and M. L. Cohen, Solid State Comm. **81**, 187 (1992).

[41] I. I. Mazin and O. V. Dolgov, Phys. Rev. B. **45**, 2509 (1992).

[42] S. Hoen, W. N. Creager, L. C. Bourne, M. F. Crommie, T. W. Barbee III, M. L. Cohen, A. Zettl, L. Bernardez, and J. Kinney, Phys. Rev. B **39**, 2269 (1989).

[43] M. K. Crawford, W. E. Farneth, E. M. McCarron III, R. L. Harlow and A. H. Moudden, Science **250**, 1390 (1990).

[44] J. P. Frank, J. Jung, M. A.-K. Mohamed, S. Gygax and G. I. Sproule, Physica B **169**, 697 (1991).

[45] H. J. Bornemann, D. E. Morris, H. B. Liu, A. P. B. Sinha, P. Narwankar and M. Chandrachood, Third International Conference on Materials and Mechanisms of Superconductivity, High Temperature Superconductors, Kanazawa, Japan, July 22-26, 1991.

[46] S. J. L. Billinge, B. H. Toby, H. D. Rosenfeld, T. Sendyka and T. Egami, *Proceedings of "Lattice Effects in High-T_c Superconductors"*, Santa Fe, NM January 13-15 (1992).

[47] S. J. L. Billinge, personal communication.

[48] J. Mustre de Leon, S. D. Conradson, I. Batistić and A. R. Bishop, Phys. Rev. Lett. 65, 1675 (1990).

[49] J. Jorgensen, personal communication.

[50] R. P. Sharma, L. E. Rehn, P. M. Baldo, and J. Z. Liu, Phys. Rev. Lett. 62, 2869 (1989).

[51] W. E. Pickett, R. E. Cohen, H. Krakauer, Phys. Rev. Lett. 67, 228 (1991).

[52] W. Wong-Ng, F. W. Gayle, D. L. Kaiser, S. F. Wakins, and F. R. Fronczek, Phys. Rev. B 41, 4220 (1990).

[53] Z. Hiroi, M. Azuma, M. Takano and Y. Takeda, Physics C 208, 286 (1993).

[54] M. G. Smith, A. Manthiram, J. Zhou, J. B. Goodenough, and J. T. Market, Nature 351, 549 (1991).

[55] C. Tarrio, E. L. Benitez and S. E. Schnatterly, Physica C 193 34 (1992).

[56] R. E. Cohen, W. E. Pickett, H. Krakauer and D. A. Papaconstantopoulos, Phase Transitions 22 167 (1990).

[57] V. H. Crespi and M. L. Cohen, (unpublished).

[58] M. K. Crawford, M. N. Kunchur, W. E. Farneth, E. M. McCarron III, and S. J. Poon, Phys. Rev. B 41, 282 (1990).

[59] C. C. Tsuei, D. M. Newns, C. C. Chi, P. C. Pattnaik, Phys. Rev. Lett. 65, 2724 (1991).

[60] Y. Maeno, N. Kakehi, M. Kato, Y. Tanaka, T. Fujita, Physica C 185, 909 (1991).

[61] S. J. L. Billinge, G. H. Kwei and H. Tagaki, Phys. Rev. Lett. 72, 2282 (1994).

[62] S. J. L. Billinge, G. H. Kwei, A. C. Lawson, J. D. Thompson et al., Phys. Rev. Lett. 71, 1903 (1993).

[63] M. K. Crawford, R. L. Harlow, E. M. McCarron, W. E. Farneth, J. D. Axe, H. Chou and Q. Huang, Phys. Rev. B 44, 7749 (1991).

[64] J. P. Franck, S. Harker and J. H. Brewer, Phys. Rev. Lett. 71, 283 (1993).

[65] S. Barišić, I. Batistić, and J. Friedel, Europhys. Lett. 3, 1231 (1987).

[66] Peter Härtwich, Sergej Flach and Jürgen Schreiber, J. Phys. Condens. Matter. 3, 2337 (1991).

[67] H. Krakauer, personal communication.

[68] T. R. Thurston, R. J. Birgeneau, D. R. Gabbe, H. P. Jenssen, M. A. Kastner, P. J. Picone, N. M. Preyer, J. D. Axe, P. Böni, G. Shirane, M. Sato, K. Fukuda, and S. Shamoto, Phys. Rev. B. 39, 4327 (1989).

[69] L. Pintschovious, J. M. Bassat, P. Odier, F. Gervais, G. Chevrier, W. Reichardt, F. Gompf, Phys. Rev. B. **40**, 2229 (1989).

[70] T. Springer, *Hydrogen in Metals I*, ed. G. Alefeld and J. Völkl, Springer-Verlag (1978).

[71] V. H. Crespi and M. L. Cohen, Solid State Comm. **83**, 427 (1992).

[72] B. Büchner, M. Cramm, M. Braden, W. Braunisch, O. Hoffels, W. Schnelle, J. Harnischmacher, R. Borowski, A. Gruetz, B. Heymer, C. Hohn, R. Müller, O. Maldonado, A. Freimuth, W. Schlabitz, G. Heger, D. I. Khomskii and D. Wohlleben,*Proceedings of the NATO ASI, Physics and Material Science of HTSC II*, Greece, August 1991, ed. R. Kossowsky, Kluwer Inc., in press.

[73] K. N. Yang, Y. Dalicaouch, J. M. Ferreria, B. W. Lee, J. J. Neumeir, M. S. Torikachivli, H. Zhou, M. B. Maple, and R. R. Hake, Solid State Commun. **63**, 515 (1987).

[74] Z. Fisk, J. D. Thompson, E. Zirngiebl, J. L. Smith, and S. W. Cheong, Solid State Commun. **62**, 743 (1987).

[75] P. H. Hor, R. L. Meng, Y. Q. Wang, L. Gao, Z. J. Huang, J. Bechtold, K. Forster, and C. W. Chu, Phys. Rev. Lett. **58**, 1891 (1987).

[76] D. W. Murphy, S. Sunshine, R. B. Van Dover, R. J. Cava, B. Batlogg, S. M. Zahurak, and L. F. Schneemeyer, Phys. Rev. Lett. **58**, 1888 (1987).

[77] L. Soderholm, K. Zhang, D. G. Hinks, M. A. Beno, J. D. Jorgenson, C. U. Segre, and I. K. Schuller, Nature **328**, 604 (1987).

[78] Y. Dalichaouch, M. S. Torikachvili, E. A. Early, B. W. Lee, C. L. Seaman, K. N. Yang, H. Zou, and M. B. Maple, Solid State Commun. **65** 1001 (1987).

[79] K. K. Liang, X. T. Xu, S. S. Xie, G. H. Rao, X. Y. Shao, and Z. G. Duan, Z. Phys. B **69**, 137 (1987).

[80] J. L. Peng, P. Klavins, R. N. Shelton, H. B. Radousky, P. A. Hahn, L. Bernardez, Phys. Rev. B **40**, 4517 (1989).

[81] G. Y. Guo and W. M. Temmerman, Phys. Rev. B **41**, 6372 (1990).

[82] J. J. Neumeier, T. Bjornholm, M. B. Maple, and Ivan K. Schuller, Phys. Rev. Lett. **63**, 2516 (1989).

[83] H. B. Radousky, Journal of Materials Research **7**, 1917 (1992).

[84] Kyun Nahm, Bo Young Cha and Chul Koo Kim, Solid State Comm. **72** 559 (1989).

[85] J. Fink, N. Nücker, H. Romberg, M. Alexander, M. B. Maple, J. J. Neumeier, and J. W. Allen, Phys. Rev. B **42**, 4823 (1990).

[86] A. A. Abrikosov and L. P. Gor'kov, JETP **12**, 1243 (1961).

[87] J. P. Carbotte, M. Gree-son, and A. Perez-Gonzalez, Phys. Rev. Lett. **66**, 1789 (1991).

[88] J. P. Franck in *Physical Properties of High Temperature Superconductors IV*, ed. D. M. Ginsberg (World Scientific, 1994) 189.

[89] M. L. Cohen, D. R. Penn, and T. W. Barbee III, Solid State Comm. **75**, 971 (1990) and T. W. Barbee III, M. L. Cohen, and D. R. Penn, Phys. Rev. B **44**, 4473 (1991).

[90] J. E. Hirsch and D. J. Scalapino, Phys. Rev. Lett. **56**, 2732 (1986).

[91] E. Schachinger, M. G. Gree-son, and J. P. Carbotte, Phys. Rev. B **42**, 406 (1990).

[92] J. P. Carbotte and R. Akis, Solid State Comm. **82**, 613 (1992).

[93] D. R. Penn and M. L. Co-hen, Phys. Rev. B, **46** 5466 (1992).

[94] W. Reichardt, N. Pyka, L. Pintschovius, B. Hennion and G. Collin, Physica C **162-164** 464 (1989).

[95] J. H. Nickel, D. E. Morris and J. W. Algers, Phys. Rev. Lett. **70**, 81 (1993) and J. H. Nickel, D. E. Morris and J. W. Ager, Phys. Rev. Lett. **72**, 1389 (1994) (reply).

[96] J. P. Franck and D. D. Lawrie, Bull. Amer. Phys. Soc. **39**, 914 (1994).

[97] V. H. Crespi and M. L. Co-hen, *Proceedings of "Lattice Effects in High-T_c Supercon-ductors"*, Santa Fe, NM January 13-15 (1992) 184.

[98] V. H. Crespi and M. L. Co-hen, Solid State Comm. **86**, 161 (1993).

[99] R. D. Fowler, J. D. G. Lind-say, R. W. White, H. H. Hill, and B. T. Matthias, Phys. Rev. Lett. **19**, 892 (1967).

[100] B. Renker, F. Gompf, E. Gering and D. Ewert, Phys-ica C **162-164**, 462 (1989)

[101] S. Tian, J. Liu, M. Li, Z.-X. Zhao, Solid State Comm. **78**, 295 (1991).

[102] V. H. Crespi and M. L. Co-hen, Phys. Rev. B **48**, 398 (1993).

[103] C. O. Rodriquez, A. I. Liechtenstein, I. I. Mazin, O. Jepsen, O. K. Anderson and M. Methfessel, Phys. Rev. B **42**, 2692 (1990).

[104] A. P. Litvinchuk, C. Thom-sen and M. Cardona, Solid State Comm. **80**, 257 (1992).

[105] J. H. Nickel, personal com-munication.

[106] J. P. Franck, A. Hnatiw, M. K. Yu, S. Gygax, G. So-erensen, E. Altendorf and J. C. Irwin, *Proceedings of "Workshop on Lattice Ef-fects in high T_c Superconduc-tors"*, Santa Fe, NM, Jan-uary 13-15, 1992, ed. Bar-Yam et al. (World Scientific, Singapore, 1992).

[107] Z. Schlesinger, R. T. Collins, F. Holtzberg, C. Feild, N. E. Bickers, and D. J. Scalapino, Nature **343**, 242 (1990).

[108] B. Chakraborty, W. E. Pickett, and P. B. Allen, *Phys. Rev. B.* **14**, 3227 (1976).

[109] W. E. Pickett, Rev. Mod. Phys. **61**, 499 (1989).

[110] R. E. Cohen, W. E. Pickett, L. L. Boyer, and H. Krakauer, *Mater. Res. Soc. Symp. Proc.* **99**, 825 (1988).

[111] H. Krakauer and W. E. Pickett, *Phys. Rev. Lett.* **60**, 1665 (1988).

[112] S. Massida, J. Yu, and A. J. Freeman, *Physica C* **152**, 251 (1988).

[113] R. Lui et al., Phys. Rev. B **45**, 5614 (1992).

[114] J. Tobin et al., Phys. Rev. B **45** 5563 (1992).

[115] D. M. King et al. (unpublished).

[116] R. Combescot, *Phys. Rev. Lett.* **67**, 148 (1991).

[117] A. B. Migdal, *Soviet Physics JETP* **34**, 996 (1958).

[118] B. Batlogg, R. J. Cava, A. Jayaraman, R. B. van Dover, G. A. Kourouklis, S. Sunshine, D. W. Murphy, L. W. Rupp, H. S. Chen, A. White, K. T. Short, A. M. Mujsce and E. A. Rietman, Phys. Rev. Lett **58**, 2333, (1987).

[119] L. C. Bourne, M. F. Crommie, A. Zettl, H. zur Loye, S. W. Keller, K. L. Leary, A. M. Stacy, K. J. Chang, M. L. Cohen and D. E. Morris, Phys. Rev. Lett. **58**, 2337 (1987).

[120] B. Friedl, C. Thomsen and M. Cardona, Phys. Rev. Lett. **65**, 915 (1990).

[121] C. W. Chu, P. H. Hor, Y. Y. Xue, G. Lin, R. L. Meng, K. Matsuishi, Z. J. Huang, C. Diaz, and Y. C. Jean, Physica C **185**, 701 (1991).

[122] R. C. Buschert, A. E. Merlini, S. Pace, S. Rodriguez, and M. H. Grimsditch, Phys. Rev. B **38**, 5219 (1988).

[123] R. E. Peierls, Quantum Theory of Solids, Oxford University Press, (1955).

[124] E. G. Haanappel, W. Joss, P. Wyder, S. Askenazy, K. Trübenbach, Hj. Mattausch, A. Simon and M. Osofsky, J. Phys. Chem. Solids **54**, 1261 (1993).

[125] V. H. Crespi and M. L. Cohen, (unpublished).

[126] S. J. L. Billinge, Physica (Amsterdam) **179C**, 279 (1991).

[127] M. Arai, K. Yamada, Y. Hidaka, S. Itoh, Z. A. Bowden, A. D. Taylor, and Y. Endoh, Phys. Rev. Lett. **69**, 359 (1992).

[128] B. H. Toby, T. Egami, J. D. Jorgensen and M. A. Subramanian, Phys. Rev. Lett. **64**, 2414 (1990).

[129] J. Remmel, O. Meyer, J. Geerk, J. Reiner, G. Linker, A. Erb and G. Müller-Vogt, Phys. Rev. B **48**, 16168 (1993).

[130] M. L. Cohen and V. H. Crespi, *Buckminsterfullerenes* ed. W. E. Billups and M. A. Ciufolini (VCH Publishers, Cambridge, UK 1993) 197.

[131] S. Saito, A. Oshiyama, and Y. Miyamoto, *Proceedings of "Computational Physics for Condensed Matter Phenomena- Methodology and Applications,"* Osaka, Japan, October 21-23 1991. ed. M. Imada, S. Miyashita, et al. Springer-Verlag.

[132] S. Saito, *Fall 1990 Materials Research Society Proceedings "Clusters and Cluster Assembled Materials"* , Boston MA, ed. R. S. Averback, D. L. Nelson and J. Bernholc.

[133] N. Troullier and J. L. Martins, (unpublished).

[134] S. Saito and A. Oshiyama, Phys. Rev. Lett. **66** 2637 (1991).

[135] S. Saito and A. Oshiyama, Phys. Rev. B **44**, 11536 (1991).

[136] J. L. Martins and N. Troullier, Phys. Rev. B **46**, 1766 (1992).

[137] S. C. Erwin and M. R. Pederson, Phys. Rev. Lett. **67**, 1610 (1991).

[138] V. de Coulon, J. L. Martins, and F. Reuse, Phys. Rev. B **45**, 13671 (1992).

[139] P. A. Heiney, J. E. Fischer, A. R. McGhie, W. J. Romanov, A. M. Denenstein, J. P. McCauley, Jr. and A. B. Smith, III, Phys. Rev. Lett. **66**, 2911 (1991).

[140] J. H. Weaver, J. L. Martins, T. Komeda, Y. Chen, T. R. Ohno, G. H. Kroll, N. Troullier, R. E. Haufler and R. E.

Smalley, Phys. Rev. Lett **66**, 1741 (1991).

[141] M. B. Jost, N. Troullier, D. M. Poirier, J. L. Martins, J. H. Weaver, L. P. F. Chibante and R. E. Smalley, Phys. Rev. B **44**, 1966 (1991).

[142] E. Burstein, S. C. Erwin, M. Y. Jiang and R. P. Messmer, Physica Scripta, **T42**, 207 (1992).

[143] S. Saito and A. Oshiyama, Physica C **185**, 421 (1991).

[144] J. L. Martins and N. Troullier, preprint.

[145] M.-Z. Huang, Y.-N. Xu and W. Y. Ching, Phys. Rev. B **47**, 8249 (1993).

[146] M.-Z. Huang, Y.-N. Xu and W. Y. Ching, Journal of Chemical Physics, **96** 1648 (1992).

[147] S. C. Erwin and W. E. Pickett, Science **254** 842 (1991).

[148] N. Hamada, S. Saito, Y. Miyamoto and A. Oshiyama, Japanese Journal of Applied Physics II- Letters **30** L2036 (1991).

[149] P. W. Stephens, L. Mihaly, P. L. Lee, R. L. Whetten, S.-M. Huang, R. Kaner, F. Deiderich and K. Holczer, Nature **351** 632 (1991).

[150] M. P. Gelfand and J. P. Lu, Phys. Rev. Lett. **68** 1050 (1992).

[151] M. P. Gelfand and J. P. Lu, Phys. Rev. B **46**, 4367 (1992).

[152] O. Zhou, J. E. Fischer, N. Coustel, S. Kycia, Q. Zhu, A. R. McGhie, W. J. Romanow,

J. P. McCauley Jr., A. B. Smith III and D E Cox, Nature **351** 462 (1991).

[153] D. A. Neumann, J. R. D. Copley, W. A. Kamitakahara, J. J. Rush, R. L. Cappelletti, N. Coustel, J. P. McCauley Jr., J. E. Fischer, A. B. Smith III, K. M. Creegan and D. M. Cox, Journal of Chem. Phys. **96**, 8631 (1992) and Journal of Phys. and Chem. of Solids **54**, 1699 (1993)..

[154] O. Zhou, G. B M. Vaughan, Q. Zhu, J. E. Fischer, P. A. Heiney, N. Coustel, J. P. McCauley Jr., and A. B. Smith III, Science **255**, 833 (1992).

[155] K. Prassides, J. Tomkinson, C. Christides, M. J. Rosseinsky, D. W. Murphy, and R. C. Haddon, Nature **354**, 462 (1991).

[156] K. Sinha, J. Menéndez, B. L. Ramakrishna and Z. Iqbal, (unpublished).

[157] V. H. Crespi, J. G Hou, X.-D. Xiang, M. L. Cohen and A. Zettl, Phys. Rev B **46**, 12064 (1992).

[158] W. E. Pickett, Bull. Am. Phys. Soc. **37**, 455 (1992).

[159] J. E. Rowe, R. A. Malic and E. E. Chaban, Bull. Am. Phys. Soc. **37**, 192 (1992).

[160] F. C. Zhang, M. Ogata, and T. M. Rice, Phys. Rev. Lett. **67** 3452 (1991).

[161] J. L. Martins, N. Troullier, and M. Schabel, (unpublished).

[162] P. J. Benning, J. L. Martins, J. H. Weaver, L. P. F. Chibante and R. E. Smalley, Science **252**, 1417 (1991).

[163] M. S. Dresselhaus, G. Dresselhaus, K. Sugihara, I. L. Spain, H. A. Goldberg, *Graphite Fibers and Filaments* , Springer Ser. Mat. Sci., Vol. 5 (Springer, Berlin, Heidelberg 1988).

[164] D. S. Bethune, G. Meijer, W. C. Tang, J. H. Rosen, W. G. Golden, H. Seki, C. A. Brown and M. S. deVries, Chem. Phys. Lett. **179**, 181 (1991).

[165] D. E. Weeks and W. G. Harter, Journal of Chemical Physics, **90** 4744 (1989).

[166] P. B. Allen, Phys. Rev. B **6**, 2577 (1972).

[167] M. G. Mitch, S. J. Chase and J. S. Lannin, Phys. Rev. Lett. **68**, 883 (1992).

[168] M. G. Mitch and J. S. Lannin, J. Phys. Chem. Solids **54**, 1801 (1993).

[169] A. F. Hebard, M. J. Rosseinsky, R. C. Haddon, D. W. Murphy, S. H. Glarum, T. T. M. Palstra, A. P. Ramirez and A. R. Kortan, Nature **350**, 600 (1991).

[170] G. Sparn, J. D. Thompson, R. L. Whetten, S.-M. Huang, R. B. Kaner, F. Diederich, G. Grüner and K. Holczer, Phys. Rev. Lett. **68** 1228 (1992).

[171] R. M. Fleming, A. P. Ramirez, M. J. Rosseinsky, D. W. Murphy, R. C. Haddon, S. M. Zahurak and A. V. Makhija, Nature **352** 787 (1991).

[172] A. Oshiyama and S. Saito, Solid State Comm. **82** 41 (1992).

[173] M. Schluter, M. Lannoo, M. Needels and G. A. Baraff, Phys. Rev. Lett. **68** 526 (1992).

[174] C. M. Varma, J. Zaanen and K. Raghavachari, Science **254**, 989 (1991).

[175] R. A. Jishi and M. S. Dresselhaus, Phys. Rev. B **45** 2597 (1992).

[176] L. Degiorgi, P. Wachter, G. Gruner, S. M. Huang, J. Wiley, and R. B. Kaner, Phys. Rev. Lett. **69**, 2987 (1992); Phys. Rev. B **46**, 11250 (1992).

[177] J. G. Hou et al., Solid State Comm. **86**, 643 (1993).

[178] Y. J. Uemura et al., Nature **352** 605 (1991).

[179] N. R. Werthamer, *Superconductivity* (ed. R. D. Parks), Marcel Dekker, Inc. New York, 1969, p. 338.

[180] B. Burk, V. H. Crespi, A. Zettl and M. L. Cohen, Phys. Rev. Lett. **72**, 3706 (1994).

[181] P. W. Stephens, L. Mihaly, J. B. Wiley, S.-M. Huang, R. B. Kaner and F. Diederich, Phys. Rev. B. **45**, 543 (1992).

[182] R. M. Fleming, M. J. Rosseinsky, A. P. Ramirez, D. W. Murphy, J. C. Tully, R. C. Haddon, T. Siegrist, R. Tycko, S. H. Glarum, P. Marsh, G. Dabbagh, S. M. Zahurak, A. V. Makhija and C. Hampton, Nature **352** 701 (1991).

[183] Z. Zhang, C.-C. Chen and C. Lieber, Science **254** 1619 (1991).

[184] J. Hubbard, Proc. Royal Society of London, Ser. **A276**, 238 (1963).

[185] S. R. White, S. Chakravarty, M. P. Gelfand and S. A. Kivelson, Phys. Rev. B **45** 5062 (1992).

[186] S. Chakravarty, M. P. Gelfand and S. A. Kivelson, Science **254** 970 (1991).

[187] S. Chakravarty and S. A. Kivelson, Europhys. Lett. **16** 751 (1991).

[188] P. E. Lammert and D. S. Rokhsar, Phys. Rev. B **48**, 4103 (1993).

[189] A. J. Heeger, S. Kivelson, J. R. Schrieffer and W.-P. Su, Rev. Mod. Phys. **60**, 781 (1988).

[190] S. Chakravarty, S. A. Kivelson, M. K. Salkola and S. Tewari, Science **256** 1306, (1992) and Bull. Am. Phys. Soc **37**, 524 (1992).

[191] W. E. Goff and P. Phillips, Bull. Am. Phys. Soc. **37**, 355 (1992).

[192] X.-D. Xiang et al., Science **256**, 1190 (1992).

[193] J. P. Carbotte, Rev. Mod. Phys. **62**, 1027 (1990).

[194] X.-D. Xiang, J. G. Hou, V. H. Crespi, A. Zettl and M. L. Cohen, Nature **361**, 54 (1993).

[195] A. F. Hebard, T. T. M. Palstra, R. C. Haddon and R. M. Fleming, Phys. Rev. B **48**, 9945 (1993).

[196] K. Holczer *et al.* Phys. Rev. Lett. **67** 271 (1991).

[197] Y. Yeshurum and A. P. Malozemoff, Phys. Rev. Lett. **60**, 2202 (1988).

[198] T. T. Palstra et al., Phys. Rev. Lett. **61**, 1662 (1988).

[199] A. P. Malozemoff, B. Batlogg, L. F. Schneemeyer and J. V. Waszczak, Springer Series in Solid-State Sciences **89**, 349 (Springer-Verlag Berlin, Heidelberg, 1989).

[200] S. C. Erwin, personal communication of Fermi velocity and plasma frequency of K_3C_{60} at the Rb_3C_{60} lattice constant.

[201] S. Foner, E. J. Mcnitt Jr., D. Heiman, S.-M. Huang and K. R. Kaner, Phys. Rev. B **46**, 14936 (1992).

[202] S. C. Erwin, personal communication.

[203] Y. Isawa, K. Tanaka, T. Yasuda, T. Koda and S. Koda, Phys. Rev. Lett. **69**, 2284 (1992).

[204] A. F. Hebard, Physics Today **45**, 26 (1992).

[205] E. Sohmen, J. Fink and W. Krätschmer, Europhys. Lett. **17**, 51 (1992).

[206] M. S. Deshpande, S. C. Erwin, S. Hong, and E. J. Mele, Phys. Rev. Lett. **71**, 2619 (1993).

[207] L. D. Rotter, Z. Schlesinger, J. P. McCauley Jr., N. Coustel, J. E. Fischer and A. B. Smith III, Nature **355**, 532 (1992).

[208] C. J. Lobb, Phys. Rev. B **36**, 3930 (1987).

[209] L. G. Aslamasov and A. I. Larkin, Phys. Lett. A **26**, 238 (1968).

[210] K. Maki, Prog. Theor. Phys. **39**, 887 (1968); **40**, 193 (1968).

[211] R. S. Thompson, Phys. Rev. B **1**, 327 (1970); Physica **55**, 296 (1971).

[212] K. Maki and R. S. Thompson, Phys. Rev. B **39**, 2767 (1989).

[213] J. Appel, Phys. Rev. Lett. **21**, 1164 (1968).

[214] H. Z. Schmidt, Z. Phys. **216**, 336 (1968).

[215] J. G. Hou and X.-D. Xiang, personal communication.

[216] J. G. Hou, X.-D. Xiang, V. H. Crespi, M. L. Cohen and A. Zettl, to appear in Physica C.

[217] T. Ishiguro and K. Yamaji, *Organic Superconductors*, Springer-Verlag, (1990) p 36.

[218] W. I. F. David, R. M. Ibberson, T. J. S. Dennis, J. P. Hare, and K. Prassides, Europhys. Lett. **18** 219 (1992).

[219] O. Gunnarsson and G. Zwicknagl, Phys. Rev. Lett. **69** 957 (1992).

[220] W. A. Vareka, and A. Zettl, Phys. Rev. Lett. **72**, 4121 (1994).

[221] W. E. Lawrence and J. W. Wilkins, Phys. Rev. B **7**, 2317 (1973).

[222]   G. Grimvall, *The electron-phonon interaction in metals*, North-Holland Publishing Company, (1991) p.p 210-223.

[223]   P. B. Allen, T. P. Beaulac, F. S. Khan, W. H. Butler, F. J. Pinski, and J. C. Swihart, Phys. Rev. B **34**, 4331 (1986).

[224]   A. P. Ramirez, A. R. Kortan, M. J. Rosseinsky, S. J. Duclos, A. M. Mujsee, R. C. Haddon, D. W. Murphy, A. V. Makhija, S. M. Zahurak and K. B. Lyons, Phys. Rev. Lett. **68** 1058 (1992).

[225]   C.-C. Chen and C. M. Lieber, Journal of the American Physical Society, **144** 3141 (1992).

[226]   I. I. Mazin, S. N. Rashkeev, V. P. Antropov, O. Jepsen, A. I. Liechtenstein and O. K. Anderson, Phys. Rev. B **45** 5114 (1992).

[227]   P. B. Allen in *Superconductivity in d- and f- Band Metals*, ed. H. Suhl and M. B. Maple (Academic Press, New York 1980) p. 291.

[228]   E. J. Mele and S. C. Erwin, (unpublished).

[229]   J. G. Hou, L. Lu, V. H. Crespi, X.-D. Xiang, A. Zettl and M. L. Cohen, submitted to Phys. Rev. Lett.

[230]   M. Gurvitch, Phys. Rev. B **24**, 7407 (1981).

[231]   R. Tycko et al., Phys. Rev. Lett **68**, 1912 (1992).

[232]   K. Prassides, personal communication.

[233]   P. W. Stephens et al., Phys. Rev. B **45**, 543 (1992).

[234]   E. L. Shirley and S. G. Louie, Phys. Rev. Lett. **71**, 133 (1993).

[235]   T. T. M. Palstra, R. C. Haddon, A. F. Hebard and J. Zaanen, Phys. Rev. Lett. **68**, 1054(1992).

[236]   Barrier regions and/or hopping conduction between grains will modify the Hall coefficient. N. F. Mott and E. A. Davis, *Electronic Processes in Non-Crystalline Materials*, (Clarendon Press, Oxford, 1971) p 53-55, N. F. Mott and E. A. Davis, *Electronic Processes in Non-Crystalline Materials*, (Clarendon Press, Oxford, 1979) p 56, p 92.

[237]   R. H. Friend and N. Bett, J. Phys. E **13**, 294 (1980).

[238]   A. Zettl, L. Lu, X.-D. Xiang, J. G. Hou, W. A. Vareka and M. S. Fuhrer, J. of Superconductivity 7, 639 (1994).

[239]   Assuming a filling fraction of β for the A_3C_{60} phase relative to an insulating background material, a parallel-plate geometry yields $R_H \propto \beta$ and $\rho \propto \beta$ such that $\mu_H = \frac{R_H}{\rho}$ is independent of β as observed, whereas a percolative island model yields $R_H \propto \beta$ and $\rho \propto \beta^n$ ($n \geq 2$) such that $\mu_H \propto \beta^{n-1}$, at variance with the experimental results.

[240]   Q. Zhu and J.E. Fisher, (private communication).

[241]   O. Zhou, Q. Zhu, G. B. M. Vaughan, J. E. Fischer, P. A.

Heiney, N. Coustel, J. Mc-Cauley Jr., A. B. Smith III and D. E. Cox, *Novel forms of carbon*, C. L. Renschler, J. J. Pouch and D. M. Cox eds. (Mat. Res. Soc., San Francisco, CA 1992), **270** 191.

[242] H. Jones and C. Zener, Proc. R. Soc. **A145** (1934).

[243] S. C. Erwin and W. E. Pickett, Phys. Rev. B **46**, 14257(1992).

[244] N. P. Ong, Phys. Rev. B **43**, 193 (1991).

[245] J. M. Ziman, Adv. in Phys. **13**, 578 (1967).

[246] T. W. Ebbesen, J. S. Tsai, K. Tanigaki, J. Tabuchi, Y. Shimakawa, Y. Kubo, I. Hirosawa and J. Mizuki, Nature **355**, 620 (1992).

[247] A. A. Zakhidov, K. Imaeda, D. M. Petty, K. Takushi, H. Inokuchi, K. Kikuchi, I. Ikemoto, S. Suzuki and Y. Achiba, Physics Letters A **164**, 355 (1992).

[248] D. S. Bethune, W. Y. Lee, M. S. deVries, J. R. Salem, W. C. Tang, H. J. Rosen, C. A. Brown, (unpublished).

[249] C.-C. Chen and C. M. Lieber, Science **259**, 655 (1993).

[250] P. W. Anderson, (unpublished).

[251] J. M. Hawkins, A. Meyer, S. Loren and R. Nunlist, Journal of the American Chemical Society, **113** 9394 (1991).

[252] D. M. Deaven and D. S. Rokhsar, Phys. Rev. B **48**, 4114 (1993).

[253] G. H. Chen, Y. J. Guo, N. Karasawa and W. A. Goddard III, Phys. Rev. B **48** 13959 (1993).

[254] A crude estimate of the electron-phonon coupling strength for intermolecular translational modes can be found in V. H. Crespi, J. G Hou, X.-D. Xiang, M. L. Cohen and A. Zettl, Phys. Rev B **46**, 12064 (1992).

[255] T. W. Ebbesen, J. S. Tsai, K. Tanigaki, H. Hiura, Y. Shimakawa, Y. Kubo, I. Hirosawa and J. Mizuki, Physica C **203**, 163 (1992).

[256] Auban-Senzier, G. Quirion, D. Jerome, P. Bernier, S. Della-Negra, C. Fabre and A. Rassat, Synthetic Metals **56**, 3027 (1993).

[257] G. Sparn and J. D. Thompson, Phys. Rev. Lett. **68**, 1228 (1992).

[258] H. Holloway, K. C. Hass, M. A. Tamor, T. R. Anthony and W. F. Banholzer, Phys. Rev. B **44**, 7123 (1991).

[259] D. A. Neumann, J. R. D. Copley, D. Reznik, W. A. Kamitakahara, J. J. Rush, R. L. Paul and R. M. Lindstrom, unpublished.

[260] J. W. White, G. Lindsell, L. Pang, A. Palmisano, D. S. Silva and J. Tomkinson, Chem. Phys. Lett.**191**, 92 (1992).

[261] W. Zhang, H. Zheng and K. H. Bennemann, Solid State Comm. **82**, 679 (1992).

[262] I. I. Mazin, O. V. Dolgov, A Golubov and S. V. Shulga, Phys. Rev. B **47**, 538 (1993).

LAWRENCE BERKELEY LABORATORY
UNIVERSITY OF CALIFORNIA
TECHNICAL INFORMATION DEPARTMENT
BERKELEY, CALIFORNIA 94720